This publication is an edited version of:

Diss. ETH No. 17094

Sensor Modeling, Calibration and Point Positioning with Terrestrial Panoramic Cameras

A dissertation submitted to the
SWISS FEDERAL INSTITUTE OF TECHNOLOGY (ETH) ZURICH

for the degree of
Doctor of Sciences

presented by

JAFAR AMIRI PARIAN
M.Sc., Tehran University

born 16.03.1977
citizen of Iran

accepted on the recommendation of

Prof. Dr. Armin Gruen, examiner
ETH Zurich, Switzerland

Associate Prof. Dr. Ali Azizi, co-examiner
Tehran University, Iran

Prof. Dr. habil. Hans-Gerd Maas, co-examiner
Technical University of Dresden, Germany

Zurich 2007

IGP Mitteilungen Nr. 94

Sensor Modeling, Calibration and Point Positioning with Terrestrial Panoramic Cameras
Jafar Amiri Parian
March 2007

Published by
Institut für Geodäsie und Photogrammetrie
Eidgenössische Technische Hochschule Zürich
ETH Hönggerberg
CH-8093 Zürich

ISSN 0252-9335
ISBN 3-906467-66-10

ABSTRACT

Several techniques have been used for terrestrial panoramic imaging. Known methods for panoramic imaging include: mosaicking/stitching of a rotated frame array CCD camera, mirror technology including single mirror and multi mirrors, near 180 degrees with large frame cameras or one shot with fish-eye lens and recently a linear array-based panoramic camera by horizontal rotation. Up to now, the technique of panorama production has mainly been used for pure imaging purposes, such as indoor imaging, landscape and cultural heritage recording, tourism advertising and image-based rendering and for efficient internet representations. Among the above panorama techniques, the linear array-based panoramic camera delivers a seamless high-resolution panoramic image with a Giga-pixel resolution in one shot. The camera consists of a linear array, which is mounted on a high precision turntable parallel to the rotation axis. The linear array sensor captures the scene by rotation of the turntable as a continuous set of vertical scan lines. The elegant image acquisition mode and the high information content of these panoramic images make them suitable candidates for quantitative image analysis.

For accurate measurements a sophisticated camera calibration is an important prerequisite. However, due to intrinsic differences between the frame array pinhole camera model and a terrestrial linear array-based panoramic camera model, previously developed sensor models for frame array cameras cannot be used for the calibration of the terrestrial linear array-based panoramic cameras. Therefore a new sensor model is needed.

We developed a sensor model for terrestrial linear array-based panoramic cameras by means of additional parameters, which models substantial deviations of a physical camera from the ideal one. The additional parameters model stationary and non-stationary systematic errors. The stationary systematic errors are related to: the lens, the configuration of the linear array with respect to the lens and the turntable, and the correction to the angular pixel size of the turntable. The source of non-stationary systematic errors is the dynamic mode of image acquisition. Systematic errors that are related to the dynamic behavior of the camera system are: non-equal angular pixel size and tumbling. The investigation of the modeling of these systematic errors is based on image space residual analysis and tumbling measurements by means of an inclinometer for the *SpheroCam*. Two terrestrial linear array-based panoramic cameras, the *EYESCAN* and the *SpheroCam*, are calibrated thorough self-calibration by the sensor model that was developed using additional parameters. Even though the system is highly dynamic a sub-pixel level of accuracy is obtained. The system's accuracy for 3D point positioning is validated by use of specific testfields. We also investigate the minimum number

of control points for the self-calibration. We extend the sensor model in order to calibrate terrestrial laser scanners providing laser intensity images, which operate similarly to panoramic cameras. Through the joint sensor model of terrestrial linear array-based panoramic cameras and terrestrial laser scanners, a laser scanner, *Imager 5003*, is calibrated. We achieve a sub-pixel level accuracy through self-calibration.

A lot of control points are needed to determine the tumbling parameters through bundle adjustment. This makes the use of the sensor inconvenient in practice. Object space information, such as 3D straight-lines, provides extra conditions and reduces the number of control points for calibration and orientation. So far, straight-line information has been mainly used to determine interior orientation and additional parameters with single frame cameras. Due to the eccentricity of the projection center from the rotation axis, the acquired panoramic images do not have a single projection center. Therefore the mathematical model which has been used for single projection center cameras cannot be applied. We develop a new mathematical model for the processing of 3D straight-lines in panoramic images. We show that 3D straight-line information can be used in addition to tie points for calibration and orientation. This allows a full calibration and orientation without control points, which makes the use of the sensor more efficient.

In addition to a sensor model, network design is considered to get the best possible accuracy. Network design considerations of panoramic cameras are assessed with respect to precision and reliability enhancement and the ability of the network for self-calibration. In terrestrial panoramic cameras the camera system is designed to have a leveled turntable, which reduces the mechanical errors of the camera system during rotation. However, this leads to restrictions in network design. Since the optical axis is always horizontal, the convergent concept cannot be realized in vertical direction. This loss in network flexibility must be compensated by other measures. We analyze several close-range networks of linear array-based panoramic camera stations through computer heuristic simulation in order to assess the precision and reliability. Joint networks of frame array CCD and linear array-based panoramic cameras are also compared with networks of linear array-based panoramic cameras only. We also investigate into the influence of different network configurations on the determination of additional parameters for self-calibration and point positioning. The accuracy and precision values of object points and the correlations of additional parameters with respect to the object point coordinates and the exterior orientation parameters are analyzed for this purpose. Networks of leveled and tilted linear array-based panoramic camera stations are analyzed by computer simulation. We show that with increasing tilt of camera stations the correlations of parameters decrease, especially the correlations of additional parameters with object space coordinates. We suggest tilted camera stations for self-calibration of linear array-based panoramic cameras and point positioning.

We show the influence of datum definition on the solution vector (all unknown parameters) and the quality analysis matrices, which are computed from least squares bundle adjustment with an analytical proof. We also give numerical examples in addition to the analytical proof.

The work that we present in this dissertation adds new and novel topics to the photogrammetric community. It provides preliminarily steps for further exploration such as measurement applications.

ZUSAMMENFASSUNG

In der Vergangenheit wurden verschiedene Techniken für terrestrische Panoramaaufnahmen verwendet. Folgende Methoden sind bekannt: Mosaikieren, Zusammenfügen von Bilder aufgenommen mit einer rotierenden Stillvideo-Kamera, die Spiegeltechnik mit einem oder mehreren Spiegeln, hochauflösende Kameras mit einem Blickwinkel von nahezu 180 Grad oder Aufnahmen mit einem Fish-Eye-Objektiv sowie in den letzten Jahren Rotationszeilenkameras. Vor wenigen Jahren wurde die Panoramatechnik fast ausschliesslich für photographische Aufnahmen innerhalb eines Gebäudes, Landschafts- und Kulturgutaufnahmen, Werbung für den Tourismus, Bildbasierende Renderverfahren und Panoramen für die Erhöhung der Attraktivität von Webseiten verwendet. Mit Rotationszeilenkameras können bei einer Aufnahme nahtlose Bilder von über 1 Giga-Pixel erzeugt werden. Diese Art von Kamera besteht aus einem Linearzeilensensor, der auf einer hoch präzisen Drehscheibe parallel zur Rotationsachse montiert ist. Die CCD-Zeile nimmt aufgrund seiner Rotationsbewegung kontinuierlich eine Reihe von vertikalen Zeilen auf. Durch diese elegante Bildaufnahmemethode und dem hohen Informationsgehalt der generierten Panoramen, können die erzeugten Bilder für eine quantitative Bildanalyse verwendet werden.

Vorraussetzung für genaue Messungen ist eine ausgeklügelte Kamerakalibrierung. Aufgrund der wesentlichen Unterschiede von Lochkameras gegenüber Rotations-zeilenkameras, können die bisher entwickelten Kameramodelle nicht für die Kalibrierung von Rotationszeilenkameras verwendet werden. Daher bestand die Notwendigkeit für die Entwicklung eines neuen Sensormodells.

Im Rahmen der vorliegenden Dissertationsarbeit wurde ein Kameramodell mit zusätzlichen Parametern für Rotationszeilenkameras entwickelt. Dieses Kameramodell berücksichtigt die Abweichungen zwischen physikalischen und optimalen Modell, indem konstante und nicht konstante systematische Fehler modelliert werden. Konstante systematische Fehler sind abhängig vom Objektiv, von der Anordnung des Zeilensensors gegenüber dem Objektiv und Drehtisch, sowie der Korrektion der Pixelgrösse aus der Rotationswinkelbestimmung. Variationen in der Pixelgrösse und Taumelbewegungen des Drehtisches sind nicht konstante systematische Fehler, welche durch die Bewegung des Drehtisches während der Bildaufnahme hervorgerufen werden. Die systematischen Fehler wurden anhand der resultierenden Standardabweichungen der Gewichtseinheit aus der Ausgleichung analysiert. Zusätzlich konnte die Taumelbewegung mittels Inklinometer für die SpheroCam bestimmt werden. In der vorliegenden Arbeit wurden anhand des entwickelten Sensormodells mit zusätzlichen Parametern zwei Rotationszeilenkameras mittels Selbstkalibrierung kalibriert. Obwohl diese

Kamera-systeme sehr dynamisch sind, konnte eine Genauigkeit im Subpixelbereich mit dem verwendeten Kameramodell erzielt werden. Die Systemgenauigkeit für die 3D-Positionierung der Punkte wurde mit Hilfe von speziellen Testfeldern analysiert. Außerdem konnte die minimal zur Kalibrierung notwendige Anzahl von Passpunkten bestimmt werden. Weiterhin wurde das Sensormodell erweitert, sodass auch Laserscanner, die Intensitätsbilder generieren, kalibriert werden können. Durch das kombinierte Sensormodell für Rotationszeilenkameras und Laserscanner konnte der Laserscanner „Imager 5003“ mittels Selbstkalibrierung im Subpixelbereich kalibriert werden.

Die Verwendung von Rotationszeilenkamera ist jedoch in der Praxis schwierig, da eine grosse Anzahl von Passpunkten benötigt wird, um die Parameter der Taumelbewegung mit der Bündelblockausgleichung zu bestimmen. Unter Verwendung von zusätzlichen geometrischen Informationen, wie zum Beispiel Geraden, ergeben sich Bedingungen, welche die Anzahl der benötigten Passpunkte für die Kalibrierung und Orientierung reduzieren.
Bisher wurden Informationen aus Geraden für die Bestimmung der inneren Orientierung und zusätzlicher Parameter von Flächensensoren verwendet. Das mathematische Modell für Kameras mit fixem Projektionszentrum, kann für Rotationszeilenkamera nicht direkt verwendet werden, da die aufgenommen Panoramabilder kein festes Projektionszentrum (Exzentrizität zwischen Projektionszentrum und Rotationsachse) haben. Aus diesem Grund wurde ein neues mathematisches Modell entwickelt, welches die gewonnen Information aus den Geraden mit berücksichtigt. Mit den Informationen aus Verknüpfungspunkten und aus Geraden konnte eine Kalibrierung und Orientierung ohne Verwendung von Passpunkten durchgeführt werden. Dieses Verfahren gestattet uns eine effiziente Verwendung solcher Sensoren.

Um eine möglichst hohe Genauigkeit zu erreichen, wurde in dieser Arbeit zusätzlich zur Sensormodellierung das Netzwerk-Design untersucht. Das Netzwerk-Design für Panoramakameras wurde, unter Berücksichtigung der Genauigkeitsverbesserung und der Erhöhung der Zuverlässigkeit sowie der Eignung des Netzwerkes für die Selbst-kalibrierung, entwickelt. Bei terrestrischen Rotationszeilenkameras wurde das Kamerasystem so konstruiert, dass mit einem horizontierten Drehtische, die Einflüsse der mechanischen Fehler während der Rotation minimiert werden. Diese Art von Konstruktion führt zu einer Einschränkung im Netzwerk-Design. Aufgrund der horizontal verlaufenden optischen Achse, existieren keine konvergente Schnitte in vertikaler Richtung. Diese Einschränkung in der Flexibilität des Netzwerkes muss daher durch andere Beobachtungen kompensiert werden. Um dennoch die Genauigkeit und Zuverlässigkeit zu steigern, wurden verschiedene Konfigurationen im Nahbereich für Rotationszeilenkamera durch computergestützte heuristische Simulationen analysiert. Außerdem wurden gemeinsame Netzwerkkonfiguration von Flächensensoren und Rotationszeilenkamera mit reinen Netzwerken von Rotationszeilenkameras verglichen. Eine weitere Untersuchung war der Einfluss von verschiedenen Netzwerkkonfigurationen auf die Bestimmbarkeit von 3D-Punkten und von zusätzlichen Parametern. Dafür wurden die berechneten und theoretischen Genauigkeitswerte der Objektpunkte und die Korrelationen der zusätzlichen Parameter analysiert. Ferner wurden verschiedene Netzwerke für horizontierte und geneigte Rotationszeilenkamerakonfigurationen mittels Rechnersimulationen analysiert. Die Untersuchungen ergaben, dass geneigte Kamerapositionen die Korrelation zwischen den Parameter, besonders die zwischen zusätzlichen Parameter und Objektkoordinaten, verringern. Aus den gewonnen Ergebnissen

empfehlen wir eine geneigte Kamerapositionen von Rotationszeilenkameras für die Selbstkalibrierung und 3D-Punktbestimmung.

In der vorliegenden Arbeit wurde der Einfluss der Datumsdefinition auf den Lösungsvektor (alle Parameter unbekannt) und auf die Qualitätsbeschreibende-Matrizen gezeigt. Dieser Einfluss wurde aus der Bündelblockausgleichung berechnet und analytisch geprüft. Zusätzlich zu den analytischen Tests wurden auch numerische Beispiele aufgezeigt.

Diese Dissertationsarbeit verbessert existierende und behandelt neue Methoden der Photogrammetrie und gibt uns das Rüstzeug für weitere Untersuchungen, wie zum Beispiel verschiedene Messanwendungen mit Rotationszeilenkameras.

Table of Contents

1

Introduction

"Photogrammetry is the art, science and technology of obtaining reliable information about physical objects and environment through processes of recording, measuring and interpreting photographic images and patterns of electromagnetic radiant and other phenomena" (Slama, 1980).

Close-range photogrammetry is a specialized branch of photogrammetry which is predominantly non-topographic and terrestrial based and involves the measurement of objects with a camera to object distance of less than three hundred meters. The majority of close-range photogrammetric activities satisfy the above definitions. However, the definition is not absolute and some photogrammetric applications, which fall under the banner of "close-range", do not meet all of the above requirements.

Applications of close-range photogrammetry have traditionally been in the areas of archeology, architecture, medicine, crime and accident investigation, industry and engineering. Techniques used for aerial photogrammetry, which are well developed and understood, have been adapted to these close-range photogrammetric applications. The adaptation of these techniques to close-range photogrammetry has resulted in high precision, which are required in the areas of engineering and industrial metrology and monitoring. Frame array cameras (metric and non-metric) have been used in many applications and they have become a standard sensor in close-range photogrammetry.

Terrestrial linear array-based panoramic cameras are suitable candidates to be used for applications dealing with static scenes. Up to now, these techniques have mainly been used for pure imaging purposes, such as indoor imaging, landscape and cultural heritage recording, tourism advertising and image-based rendering, and recently for efficient internet representations.

A terrestrial linear array-based panoramic camera consists of a linear array, which is mounted on a high precision turntable parallel to a rotation axis. The linear array sensor captures the scene by rotation of turntable as a continuous set of vertical scan lines. They have been designed in order to capture a 360° horizontal field of view. The vertical field of view of the camera system depends on the lens and also the focal length of the lens. A panoramic image usually has cylindrical geometry.

The main advantages of linear array-based panoramic cameras with respect to frame array CCD cameras are two-fold. The first is high information content of panoramic images because of the larger field of view and larger format size. The second is the cylindrical or spherical geometry of the images, which inherently strengthens the geometry of the network of panoramic cameras.

Due to intrinsic differences between the frame array CCD camera model and linear array-based panoramic camera model, the sensor model that were developed previously for frame array CCD cameras cannot be used for the calibration of linear array-based panoramic cameras. The general calibration scenario and some of the procedures, like automatic detection of targets, may be similar for both sensors. However, differences like single versus multiple projection centers and planar versus cylindrical image geometry lead to different systematic errors. Because of different geometry and systematic errors, the design of a new sensor model and investigation of new additional parameters are needed.

A close-range photogrammetric network of terrestrial linear array-based panoramic camera stations, for high precision applications and for the purpose of self-calibration requires new verification. It is essential to be able to determine the most appropriate design, in terms of specified quality criteria in close-range photogrammetric applications, especially where achievable precision is pushed to a limit and calibration is demanded. As the use of terrestrial linear array-based panoramic cameras in close-range photogrammetry becomes more accepted as a precise metrology tool, it will be necessary for a photogrammetric evaluation of these new sensors in terms of accuracy potential and capability for different applications.

This dissertation allows a photogrammetrist the flexibility of using terrestrial linear array-based panoramic cameras in measurement applications. The aims are:

- to develop a joint sensor model for terrestrial linear array-based panoramic cameras and terrestrial laser scanners with laser intensity image,
- to perform sensor self-calibration and accuracy tests,
- to develop and adopt the techniques of close-range photogrammetric network design using terrestrial linear array-based panoramic cameras and joint sensors such as panoramic and frame array CCD cameras for precision and reliability enhancement and self-calibration.

For the purpose of meeting the aims of this dissertation, most of the concepts associated with sensor modeling, sensor calibration and close-range photogrammetric network design have been studied, developed and implemented. The reasons of such overall coverage of topics in this dissertation are two-fold. The first reason is that the terrestrial linear array-based panoramic camera is a new sensor and these topics should be investigated for it. The second reason is the particular requirements of close-range photogrammetric evaluations and the significance of such evaluations in terms of optimization, concepts and least squares theory. For example: least squares with mixed adjustment model in which the observations and unknowns are implicitly related, the concepts of datum, free network adjustment, datum independent parameters and network design problems.

The original contributions of this thesis are:

- a joint sensor model with additional parameters for terrestrial linear-array based panoramic cameras and terrestrial laser scanner,
- physical measurement, spectral analysis and the modeling of tumbling,
- a new mathematical model for bundle block self-calibration of terrestrial linear-array based panoramic cameras using 3D straight-lines,
- investigation on the minimal number of control points for the self-calibration of terrestrial linear-array based panoramic cameras,
- precision and reliability enhancement of the networks of panoramic cameras and the joint networks of panoramic and frame array CCD cameras by network design and analysis,
- proposing tilted panoramic camera stations as a general rule for self-calibration and point positioning by network analysis,
- the proof of datum-independency of the additional parameters of frame array and panoramic cameras.

In this dissertation terrestrial linear array-based panoramic cameras are referred to as "panoramic cameras". Two other sensors are used in connection with panoramic cameras: a single frame array camera referred to as "frame array camera" and a terrestrial laser scanner. The author assumes that the reader of this dissertation is familiar with the concepts of least squares optimization and geodetic and photogrammetric network design. Therefore each chapter only discusses the target topics and avoids detailed introduction.

Chapter 2 gives an overview to the state-of-the-art of panoramic techniques. Chapter 3 develops a joint sensor model for terrestrial panoramic cameras and laser scanners. Chapter 4 gives the results of self-calibration and accuracy tests of terrestrial panoramic cameras and a laser scanner.

Chapter 5 analyzes networks of terrestrial panoramic cameras by heuristic simulation for precision and reliability enhancement. In addition, it develops close-range photogrammetric networks for the purpose of self-calibration of panoramic cameras. Chapter 6 provides the proof for datum independent parameters, additional parameters, and quality analysis matrices of the least squares bundle adjustment.

2

State-of-the-Art of Panoramic Techniques

2.1 Introduction

Physical agents living in complex environments, such as humans and animals, need two types of visual sensing abilities. One is to focus on particular objects with a precise but small retina and the other is to look around the environment with a wide but coarse retina. Both visual sensing mechanisms are required to enable robust and flexible visual behaviors. In particular, the wide visual information obtained by looking around is necessary to monitor wide areas and to avoid dangerous situations. If the complete surrounding in space can be involved into the perception process, orientation and navigation in space becomes easier and more reliable.

According to Merriam-Webster's dictionary, the word "panorama" is a combination of the Greek terms, namely the suffix *pan* ($\pi\alpha\nu$), meaning "all", and *horama* ($o\rho\alpha\mu\alpha$), meaning "sight". The dictionary also listed the year of its conception or start of popular usage as 1796. In more technical usage, a panorama is defined as a picture or a series of pictures of a landscape, a historical event, etc. representing a continuous scene, enclosing the spectator and providing an unlimited view in all directions, which synonymously means "omnidirectional". In both cases the meaning of wide field of view visibility is conveyed.

From the technological point of view, the demand of panorama creation was realized since the beginning of photography since the camera's field of view is always smaller than the human field of view and large objects could not be captured in a single picture.

The first panoramic camera was invented by P. Puchberger of Austria in 1843. It was a hand crank driven swing lens panoramic camera capable of capturing images with 150° horizontal field of view. The rotating camera invention of M. Grarella from England in 1857 extended the field of view of capture to a full 360°. Puchberger's camera belongs to a class of swing lens cameras while Grarellas's camera belongs to the rotating cameras. Another class of cameras, namely extra wide-angle cameras, does not rely on moving parts for panoramic capture. One of the earliest cameras with very wide-angle capture is T.

Sutton's panoramic camera that was invented in 1858. It uses a spherical lens filled with water to achieve the field of view of 120°. Many of the more recent non-moving camera configurations are combination of mirrors and lenses (Benosman and Kang, 2001).

2.2 Panoramic Techniques

The techniques of panorama production can be divided in two different groups (Figure 2.1): "catadioptric" and "dioptric" systems. Dioptrics is the science of refracting elements (lenses) whereas "catoptrics" is the science of the reflecting surfaces (mirrors). The combination of refracting and reflecting elements is called catadioptrics.

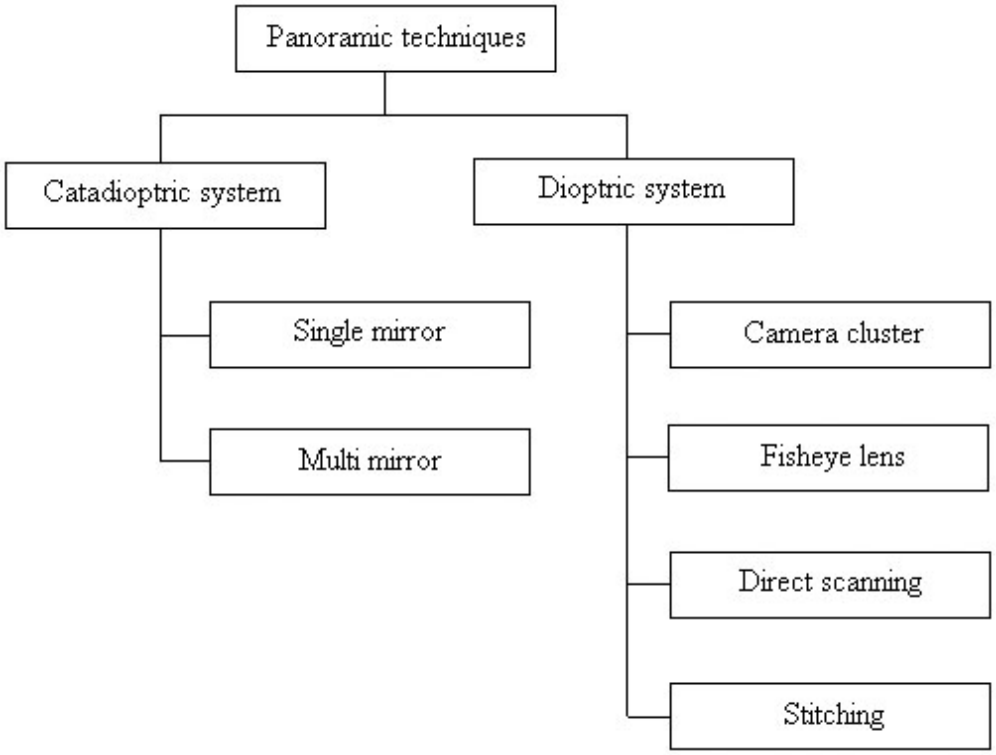

Figure 2.1. Panoramic techniques. It is divided into catadioptric and dioptric systems.

Catadioptric systems use one or more mirrors with one or more cameras to capture a wide view angle of the scene. The images then need mosaicking and in special cases, seamless panoramas can be created. Planar and curved mirrors are used in this system.

Dioptric systems are divided into four groups: camera cluster, fisheye lens, direct scanning and stitching. The first group uses different cameras, mounted on a surface and looking outwards to the scene which enables capturing the wide view of the scene. The second group consists of a camera with a fisheye lens which usually has more than 180° field of view. The third group is related to the camera systems with a rotating camera or rotating lens which produces a seamless image without any need of stitching. The fourth group produces a panoramic image by mosaicking or stitching the images.

2.2.1 Catadioptric Systems

"Omnidirectional vision" system using mirrors, called catadioptric systems, are getting cheaper and more effective with the development of the technology. Therefore, they are widely applied and researched in robot vision tasks (Yagi and Yachida, 1990; Hong, 1991). A panoramic camera system with a frame array CCD camera and a proper mirror is simple, relatively cheap and it is easily calibrated (mainly for navigation purposes) and assembled. These camera systems can contain one or more mirrors depending on the applications.

2.2.1.1 Single Mirror

The first property of catadioptric system, which is highly desirable, is that the system (or, in fact, any imaging system) has a single projection center (Figure 2.2). The reason why a single projection center is so desirable is that it allows the generation of geometrically correct perspective images from the images captured by the catadioptric camera systems. Naturally, when the catadioptric imaging system is omnidirectional in its field of view, a "virtual single projection center" permits the construction of panoramic images as well as perspective ones. Planar, conical, spherical and ellipsoidal mirrors are in the class of mirrors satisfying the single (virtual) projection property (Baker and Nayar, 1998; Svoboda et al., 1997).

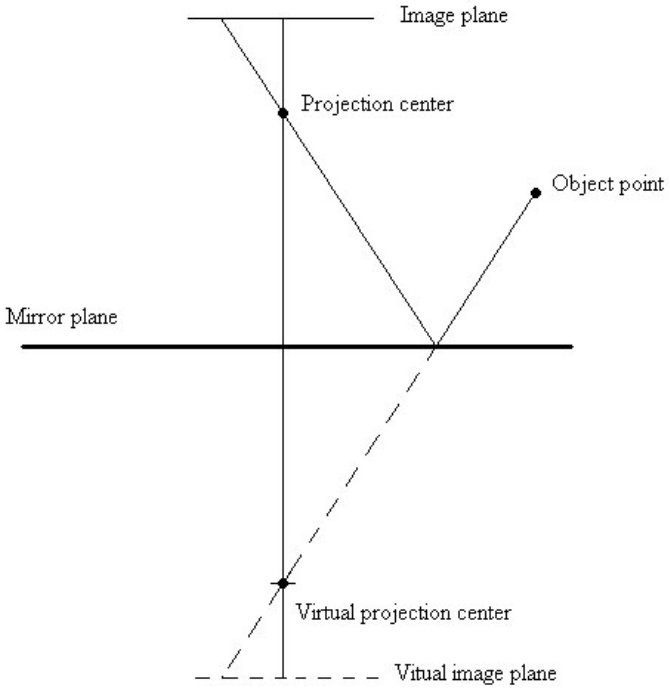

Figure 2.2. A single projection center for a planer mirror.

The second property of the camera system that images a large field of view is its resolution. Generally the resolution of a catadioptric camera is not the same as that of any of the camera used to construct it (Nayar and Backer, 1997).

The third property, which is affected by the use of a catadioptric system, is focusing because a curved (convex or concave) mirror increases image blur. Two factors combine to

cause additional blur in catadioptric systems with respect to the conventional dioptric systems: 1) the finite size of the lens aperture and 2) the curvature of the mirror.

2.2.1.2 Multi Mirrors

For 3D reconstruction or range estimation, it is necessary to have at least two images taken of the object from two different positions. If the exterior orientations of the camera at each position are known, 3D reconstruction or range estimation is possible. In most approaches this is done by using one or more cameras and taking images from different locations.

Catadioptric systems with multi mirrors can also be used for 3D reconstruction or range estimation because of distinct virtual projection centers. Figure 2.3 shows the systems with different combinations of mirrors and cameras (Ollis et al., 1999).

Figure 2.4 shows one of the cases of Figure 2.3 in which a 3D object point is projected into the image plane using two different curved mirrors. Because there are two different virtual projection centers, the re-projection of the object point from the mirrors results in two different points in the image plane.

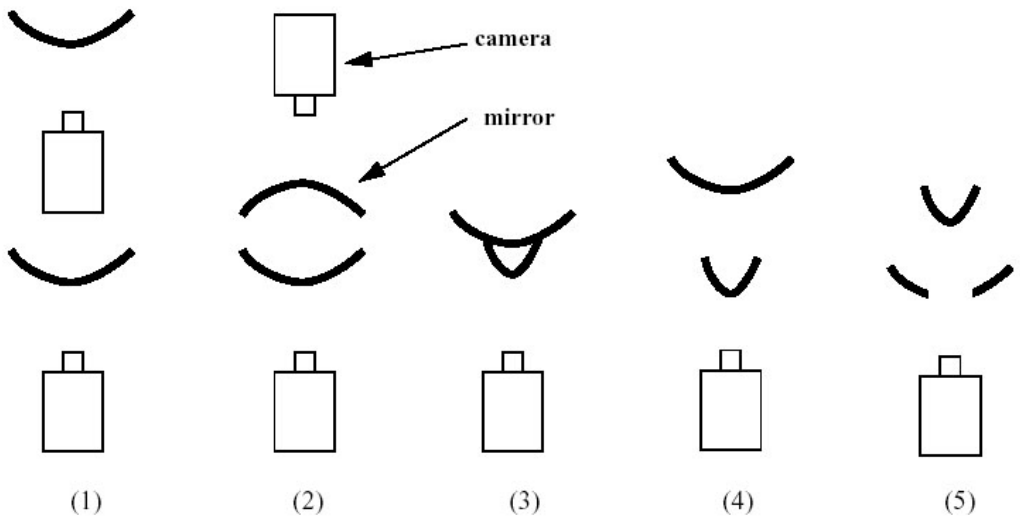

Figure 2.3. Five different configurations of multi mirrors and camera(s). The case 1 and 2 use two cameras and the cases 3, 4 and 5 use a single camera.

In addition to the previous application, a multi mirror configuration can also be used to cover an approximately full spherical panorama on the fly. For example, a panoramic video of a scene can be captured by a system of multi planar mirrors and cameras (Figure 2.5).

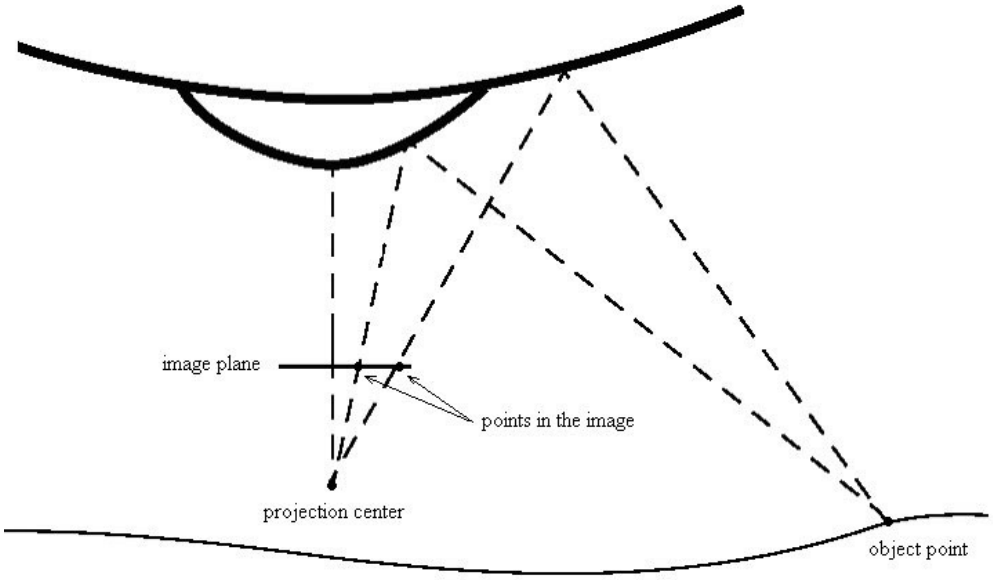

Figure 2.4. A single camera is used with a dual lobed mirror. The mirror with lower curvature is above and the mirror with higher curvature is below. The final image contains two distinct points from the 3D object point.

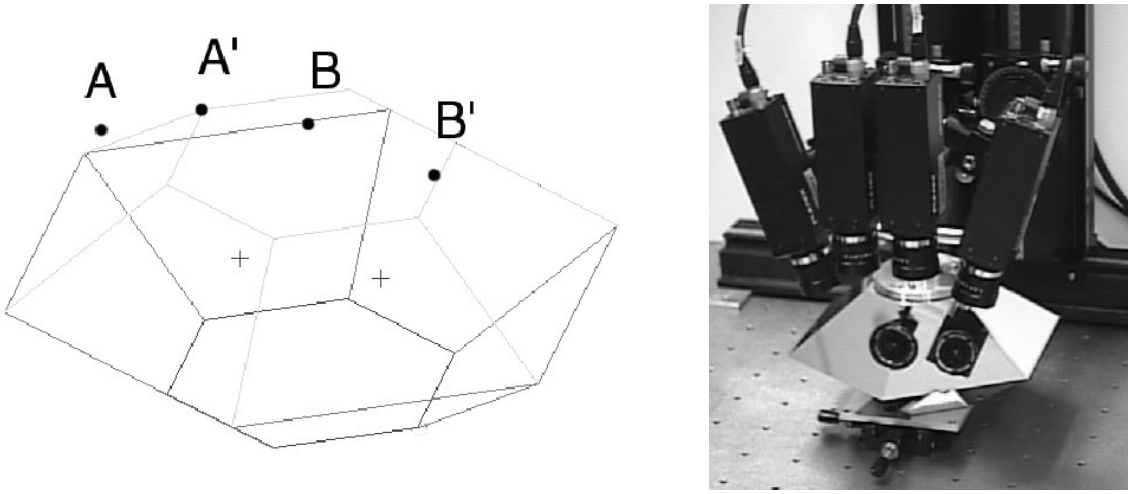

(a) (b)

Figure 2.5. A multi mirror camera system for a video acquisition. a) A design showing a 6-face pyramid and only two pairs of projection centers (AA', BB'). Each pair is associated with one face and the two virtual projection center shown as crosses (+), and b) real camera system.

A major problem with catadioptric systems is that they tend to be physically large. This is because the capture of a wide unobstructed field of view requires the lens and the mirror to be adequately separated from each other. To work around this problem, the well-known method of optical folding is used. A simple example of this is the use of a planar mirror to fold the optical path between a curved mirror and an imaging lens (Boult, 98). The folding can be in any direction. A 90° fold may help conceal some of the optical elements in an outdoor application and a 180° fold reduces the size of the entire system. Figure 2.6 shows a 180° folded catadioptric camera system based on two mirrors.

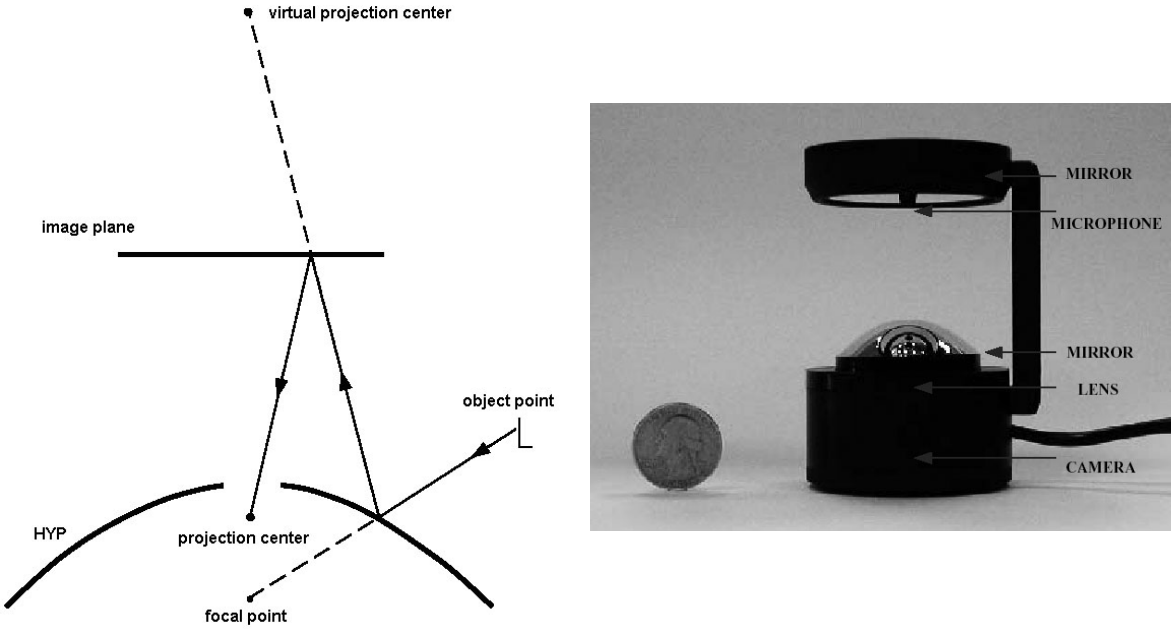

Figure 2.6. (a) Layout of the two-folded catadioptric camera design. (b) A folded catadioptric camera with a hemispherical field of view. It includes folded optics and a video camera.

2.2.2 Dioptric Systems

A dioptric system relates to the refractive elements (lenses). Mirrors may be included in these systems, but the aim is to fold optical system assembly and not increase the field of view.

2.2.2.1 Camera Cluster

The objective of a camera cluster (multi-head camera or poly-camera) is to be able to image a large field of view without loss of resolution using a minimum number of cameras. The cluster of cameras is arranged to minimize the overlap between individual adjacent views or images in order to minimize the number of cameras required to capture a full or desired field of view. In addition, the use of wide angle lenses is suggested. However, such wide angle lenses tend to have severe distortions, so calibration of each camera is necessary.

In addition, due to the finite size of the cameras, it is difficult to configure them in order to have a single projection center for the whole system. With some simplification it can be supposed that the individual projection centers of each camera are close enough to each other so that the images they produce can be stitched together seamlessly for objects beyond a minimum distance ("minimum working distance" or "parallax clearance") from the camera cluster.

An example of a camera cluster is *Dodeca* (Figure 2.7) which has been developed by *Immersive Media*[1]. The *Dodeca* uses 11 cameras arranged on a sphere, tessellated as a

[1] *http://www.immersivemedia.com*

dodecahedron. Each sensor has a small field of view and a long focal length. However, the small field of view of the cameras necessitates the use of a large number of such sensors. It results in a strong deviation from the single projection constraint, and increases the minimum working distances of the cluster. In addition, a larger number of sensors necessitates the capability of acquiring and processing more video signals simultaneously.

(a) (b) (c)

Figure 2.7. *Doceda* from *Immersive Media*. (a) Design axiom. (b) The camera with 11 frame array CCD cameras looking out of a dodecahedron to create a large field of view. (c) Dodecahedron image.

2.2.2.2 Fisheye Lens

A hemispherical or fisheye lens may represent the best acquisition tool for creating a wide field of view image. With a fisheye lens an image of more than 180° angular field of view can be acquired. Due to the large field of view, it has been used in many applications with different domains such as forestry, the study of plant canopies (Rich, 1990), geodesy to produce a site obstruction diagram for future GPS missions (Colcord, 1989). However, the photogrammetric literature shows only a few publications (Schwalbe, 2005; Van den Heuvel et al., 2006) of this type of lens. The main limitations of fisheye lens images are the impossibility of using conventional softcopy photogrammetry packages and the fact that fisheye images do not permit stereovision (Boulianne et al., 1997).

The fundamental difference between a fisheye lens and an ordinary rectilinear lens is that the projection from a 3D point to a 2D image in the fisheye lens is intrinsically non-perspective. Depending on the amount of deviation of the ray, equation (2.1) shows four different types of projections which characterize fisheye lenses (Herbert, 1987). The fisheye lens in the equation (2.1) is represented by an ideal hemispherical lens.

$$
\begin{aligned}
&\text{1) polar (equi-distance): } r = \frac{2 \cdot R \cdot \theta}{\pi} \\
&\text{2) orthographic: } r = R \cdot \sin(\theta) \\
&\text{3) Lambert's equal area: } r = \frac{2 \cdot R}{\sqrt{2}} \cdot \sin(\frac{\theta}{2}) \\
&\text{4) stereographic equal angle: } r = R \cdot \tan(\frac{\theta}{2})
\end{aligned}
\tag{2.1}
$$

with

θ…. the zenith angle,
R… the radius of hemisphere,
r…. radius of the image point from the principal point.

Most lenses available on the market are designed to produce a polar projection. Nikon 8-mm f/2.8, Canon 7.5-mm f/5.6, Sigma 15-mm f/2.8 (180° FOV) and Nikon 6-mm (220° FOV) are examples of polar projection fisheye lenses.

Figure 2.8 shows the construction of a typical fisheye lens and forming of an image by incoming rays. Figure 2.9 shows a typical image of fisheye lens from a plane plate.

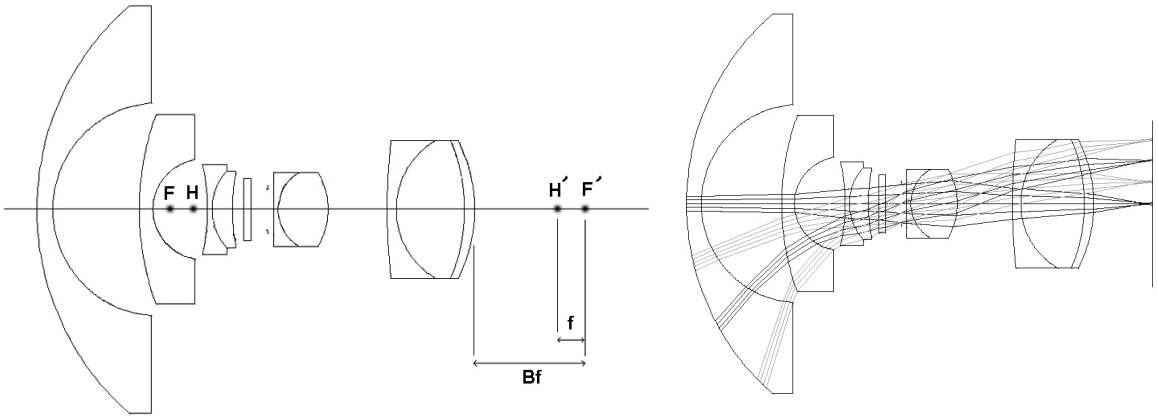

(a) (b)

Figure 2.8. a) Typical fisheye lens construction (f: focal length, Bf, backfocus, H and H': principal points, F and F': focal points). b) Incoming rays and the image formation.

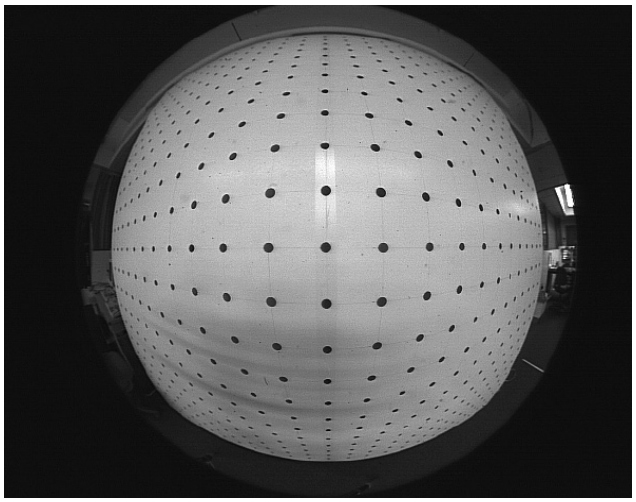

Figure 2.9. A typical image with a fisheye lens camera of a plane plate with 180° field of view.

New panoramic and immersive digital imaging developments have increased the interest in high performance fisheye camera lenses. Special concerns for such applications are the uniformity of illumination and radial image mapping. The performance of the lens at regions near to the borders of the fisheye image is just as important as the center of the image. Lateral color, high order distortion (edge compression), loss of resolution and severe drop-off of illumination at the full field are some major problems.

2.2.2.3 Direct Scanning

The direct scanning technique refers to the methods which construct seamless images by scanning the scene. A camera which operates by this method exposes a small portion of a film continuously at each specific time. A digital dynamic camera uses a linear array instead of film. This topic will be explained more in section 2.3.

2.2.2.4 Stitching

In general, stitching involves registration of a set of images to form a larger composition representing a portion of the 3D scene. In the case that the frame array CCD camera is rotated around the projection center, corresponding image points are related by a planar homography (a plane projective transformation). In the case of translating and rotating the camera (moving the projection center), the correct way is converting the perspective geometry of the image into an orthographic geometry which requires 3D information of the scene.

Image stitching has been investigated in computer graphics, computer vision and photogrammetry, for many years. Although 3D scanning technologies have been considerably improved to obtain fine detailed realistic models in computer graphics, one of the core problems remains the scene object composition. A key feature of this geometric approach is that the processing cost depends only on the intrinsic complexity of the geometric entities describing the scene. Therefore, efficient algorithms for visibility, culling strategies and progressive model refinements are of primary importance. A successful approach to navigate into virtual environments is to manipulate real data captured from our surrounding world. This stream of research is often coined "image-based rendering" or "warping". Image mosaics play an important role in the field of image-based rendering, which aims to rapidly render photorealistic views from collections of real (or pre-rendered) images (Chen, 1995). In computer vision, image mosaics are the part of the study of "visual scene representation". The complete description of visual scenes and scene models often entails the recovery of depth or parallax information (Shum and Szeliski, 1997).

Image stitching or "mosaicking" has been used in photogrammetry for cultural heritage documentation (Petsa et al, 2001) and 3D object reconstruction (Luhmann and Tecklenburg, 2004). Special panoramic heads and methods were used for precise stitching (Poentinen, 1999; Luhmann and Tecklenburg, 2002; Kukko, 2004). The influence of large eccentricities of the projection center from rotation axis for measurement applications was also investigated (Heikkinen, 2005).

Three general steps must be performed to create a panorama from images captured with rotating camera: image alignment, image cut and paste and image blending. These are described below.

2.2.2.4.1 Image Alignment

This step determines the geometric transformation that aligns the images to be combined together. The transformation ideally is a perspective transformation but simpler transformations like affine or polynomial transformations can be applied. This method is a local alignment that aligns neighboring images. The accumulation of errors of alignment in a series of the images causes some errors in the stitching process, especially for a 360°

panorama. In this case global alignment can be applied by using bundle block adjustment (Shum and Szeliski, 1997), reducing the errors of the alignment. To compute the geometric transformation parameters, the corresponding points in the neighboring images are necessary. The process of measuring the corresponding points can be done manually and automatically. In the automatic process a cross correlation or least squares matching is applied to find the correspondences. Another method uses the phase information of the Fourier transform of the images and is applied to find the overlapping areas of the neighboring images (Reddy and Chatterji, 1996).

2.2.2.4.2 Image Cut and Paste

After the transformation and alignment of the adjacent images with respect to the reference image, some regions in the reference image are covered by more than one adjacent image (overlapping parts). The cut and paste process involves either a selection of a single image for each overlapping region, or some kind of a combination of all overlapping images. It can also be a weighted sum of the overlapping pixels. The weights can be computed according to the high frequency image information (Shum and Szeliski, 1997).

2.2.2.4.3 Image Blending

This process tries to overcome the intensity and color differences between images. The intensity and color differences are present even when images are perfectly aligned, and they can cause a seam line in the stitched area. Such differences are created by a dynamically changing camera gain or severe changes of exposure. To reduce discontinuities in intensity and color between the images being stitched, a simple feathering algorithm can be applied by weighting the pixels in each image proportionally to their distance to the edge (Szeliski, 1996). An alternative to weighted blending is to select pixels from only one image (Milgram, 1977; Peleg and Herman, 1997).

2.3 Terrestrial Panoramic Cameras

With respect to the mechanical operation, terrestrial dynamic panoramic cameras are divided into two different groups. The first group consists of swing lens cameras and the second group consists of rotating cameras.

2.3.1 Swing Lens Camera

In this group of cameras, the lens rotates around a fix axis. There is a narrow vertical slit between the lens and film, which rotates with the lens, allowing the image to be progressively exposed as the lens rotates (Figure 2.10). The film is curved so that the long strip of the film being exposed is always at the same distance from the lens. This distance is the focal length of the lens. Usually, these cameras cover a field of view between 120° and 150° horizontally and 30° to 50° vertically.

2.3.2 Rotating Camera

In this type of panoramic cameras the lens is fixed in relation to the camera body and the entire camera rotates. The film moves like a conveyor belt at a speed synchronized with the

speed of the moving image to assure congruency between the image and the film (Figure 2.11). There is a very narrow vertical slit behind the objective which allows the changing image to be laid onto the moving film a little bit at a time. These cameras are able to take shots of 360° or more and they can keep rotating until they run out of film. Usually these cameras use film type 135 (35 mm).

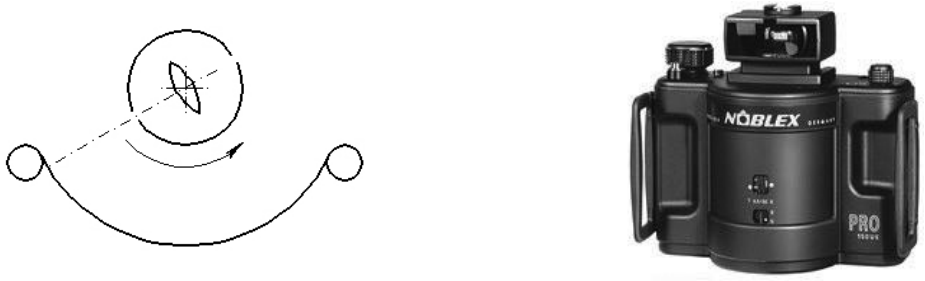

(a) (b)

Figure 2.10. Swing lens panoramic camera. a) Showing the operation of the camera and b) a typical swing lens analogue panoramic camera, *Noblex*.

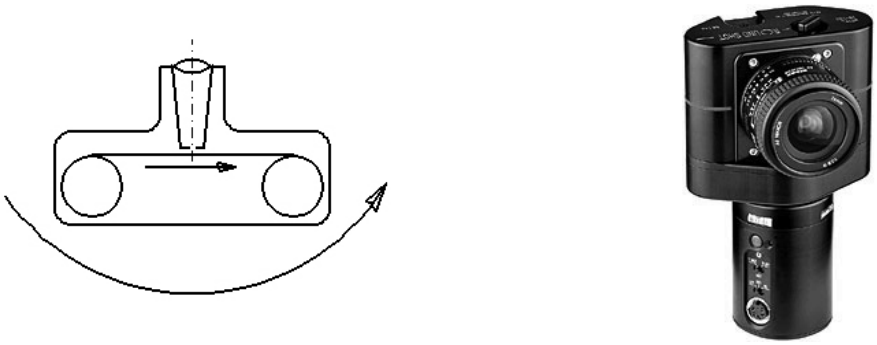

(a) (b)

Figure 2.11. Analogue rotating terrestrial panoramic camera. a) Showing the operation of the camera and b) a typical rotating analogue panoramic camera, *Roundshot*.

Through the development of digital technology, digital dynamic rotating panoramic cameras were generated. The principle of the operation is the same as the analogue rotating panoramic cameras. The camera system consists of a linear array which is mounted on a high precision turntable and is parallel to the rotation axis. By rotation of the turntable, the linear array sensor captures the scene as a continuous set of vertical scan lines.

SpheroCam from *SpheronVR AG*[1] and *EYESCAN* from the collaboration of Kamera & System Technik[2] (*KST GmbH*, Dresden) and German Aerospace Center[3] (*DLR*, Berlin) (Figure 2.12) are two typical linear array-based rotating panoramic cameras. Both systems are designed to capture a 360° horizontal field of view. The vertical field of view of the camera system depends on the lens and focal length. A precise rotating motor rotates the linear array and the lens (camera head). The horizontal angle size of each step of the rotation is computed by the camera system with respect to the focal length.

[1] http://www.spheron.com/spheron/public/
[2] http://www.kst-dresden.de/
[3] http://www.dlr.de/

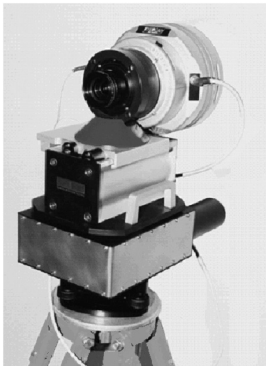

(a)

(b)

Figure 2.12. Digital rotating terrestrial panoramic cameras. a) *EYESCAN M3* and b) *SpheroCam*.

The *EYESCAN* camera system (Scheele et al., 2001) contains three parts: camera head, optical part, and high precision turntable with a DC-gearsystem motor. The camera head is connected to a PC with a bi-directional fiber link for data transmission and camera control. The optical part of the system uses high performance Rhodenstock lenses. With adjustment rings, one can use other lenses. The camera head is mounted on a high precision turntable with a sinus-commutated DC-gearsystem motor (Scheibe et al., 2001), internal motion control and direct controlling by the PC. Rotation speed and scan angle are pre-selectable and correspond to the shutter speed, image size and focal length of the lens. Table 2.1 shows specifications of *EYESCAN*.

The structure of the *SpheroCam* similar to *EYESCAN* includes 3 parts, the camera head, the optical part which is compatible with NIKON-lenses, and a DC motor to rotate the linear array. The *SpheroCam* is specially designed for use with a fisheye lens, with a near 180° vertical field of view. As it rotates about its vertical axis, the *SpheroCam* captures a complete spherical image. It is designed to capture high quality radiometric images. Table 2.1 shows specification of *SpheroCam*.

Since the acquisition time depends on the mechanical part of the rotating camera head and exposure time, it usually takes a long time, e.g. half an hour for capturing a full panoramic image of a room with Neon lights. It restricts the camera system to the use with a static scene.

Dynamic scanning provides a large image format, for example 100,000 x 10,000 pixels with 48 bits color depth per pixel (16 bits per R, G and B channels), which corresponds to a Giga-pixel image format. High information content and large format size makes panoramic cameras suitable candidates for applications like 3D object reconstruction and texture mapping.

Table 2.1. Specifications of *EYESCAN* and *SpheroCam* panoramic cameras.

Technical Specifications	*EYESCAN* [1]	*SpheroCam*
Hardware		
Color depth (RGB)	3 x 14 / 3 x 8 bit per color	3 x 16 bit per color
Turntable driving unit	Sinus-commutated DC-gearsystem motor with internal motion control	DC motor
Linear Array Sensor		
Number of pixels of the linear array	3,600 or 10,200	5,300
Pixel size (micron)	7 or 8	8
Image Acquisition		
Vertical field of view	Depends on the lens	180° with fisheye lens
Shutter speed for the linear array image acquisition (second)	1/1,000 up to ½	1/10,000 up to 1/4
Operation		
Full scan time: 360° horizontal filed of view [2]	3 minutes	30 seconds

[1] Parameters belong to *EYESCAN M2* and *EYESCAN M3*
[2] Depends on the mechanical factors, exposure time and data transmission to a PC

3

A Joint Sensor Model for Panoramic Cameras and Laser Scanners

3.1 Introduction

Due to intrinsic differences between the frame array pinhole camera model and a terrestrial panoramic camera model, previously developed sensor model and additional parameters for frame array cameras cannot be used for the self-calibration of panoramic cameras. The general calibration scenario, for example testfield, measuring the targets in the image and some of the procedures that was used for example, automatic detection of targets may be similar for both frame array and panoramic cameras. However, differences in camera architecture, e.g. multiple projection centers, and cylindrical image geometry, different systematic errors and therefore different additional parameters require the design of new sensor models and additional parameters.

Previous work on the sensor modeling of terrestrial panoramic cameras refers to Lisowski and Wiedemann (1998). Schneider and Maas (2003) investigated a geometrical model with additional parameters for a prototype of the *EYESCAN* panoramic camera and performed self-calibration by using a specific testfield. Schneider and Maas (2004) performed accuracy tests by bundle block adjustment. Amiri Parian and Gruen (2003) developed a sensor model with additional parameters for panoramic cameras and performed self-calibration and accuracy tests by using specific testfields for *EYESCAN* and *SpheroCam* panoramic cameras. Tumbling, a mechanical error of the turntable, was modeled by Amiri Parian and Gruen (2004a). Amiri Parian and Gruen (2004b) investigated the minimum number of control points needed for successful orientation and self-calibration. The use of 3D straight-line constraints with bundle block adjustment for self-calibration of panoramic cameras was reported in Amiri Parian and Gruen (2005a). The results of the extended sensor model of panoramic cameras for the modeling of terrestrial laser scanners with intensity image was shown in Amiri Parian and Gruen (2005b). A sensor model for a metric panoramic camera, *EYESCAN*, was demonstrated in Schneider and Maas (2006).

This chapter develops a joint sensor model for terrestrial panoramic cameras and laser scanners with intensity images. Section 3.2 develops an ideal sensor model for panoramic cameras. Section 3.3 introduces systematic errors and develops additional parameters for the modeling of systematic errors. Stationary and non-stationary systematic errors are modeled in this section. Section 3.4 develops a sensor model with additional parameters for real panoramic cameras with two least squares models for bundle adjustment. Section 3.5 extends the sensor model of panoramic cameras for terrestrial laser scanners with intensity images. Section 3.6 introduces and models three object space constraints that are integrated into bundle block adjustment.

3.2 Sensor Model for the Ideal Panoramic Camera

The sensor model as a mapping function is based on a perspective projection in the form of bundle equations, which maps the 3D object space points into the linear array coordinate system.

For the sake of simplicity of the modeling, four coordinate systems are defined as follow:

- pixel coordinate system,
- linear array coordinate system,
- turntable coordinate system,
- 3D object coordinate system.

Figure 3.1 shows the pixel coordinate (i, j) system. The original image observations are stored in this coordinate system.

Figure 3.2 shows the other coordinate systems: linear array (0, y, z), turntable (X', Y', Z') and object space (X, Y, Z) coordinate systems.

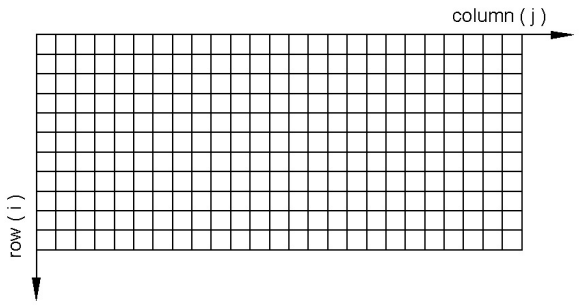

Figure 3.1. Pixel coordinate system (i, j).

To define the turntable coordinate system, the ideal panoramic camera is considered. The origin of the turntable coordinate system (O) coincides with the projection center. The rotation axis passes through the projection center and coincides with Z'. X' passes through the start position of the linear array before rotation and Y' is defined to get a right-handed coordinate system.

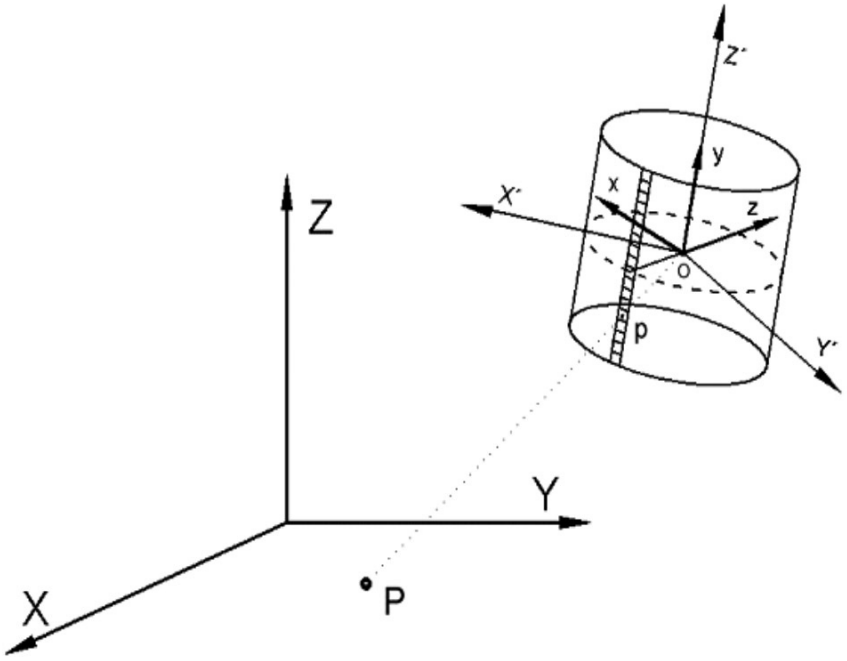

Figure 3.2. Object coordinate (X, Y, Z), turntable coordinate (X', Y', Z') and linear array (0, y, z) coordinate systems.

Equation (3.1), which is a 3D conformal transformation with 6 parameters, shows the relation between the object space coordinate system and the turntable coordinate system.

$$\begin{pmatrix} X' \\ Y' \\ Z' \end{pmatrix} = M_{\omega,\varphi,k} \cdot \begin{pmatrix} X - X_0 \\ Y - Y_0 \\ Z - Z_0 \end{pmatrix} \tag{3.1}$$

where,

(X_0, Y_0, Z_0)... location of the origin of the turntable coordinate system in the object space coordinate system,

(X, Y, Z)….. object point coordinates,

(X', Y', Z')…. object point coordinates in the turntable coordinate system,

$M_{\omega,\varphi,k}$ …….. rotation matrix with elements defined in equation (3.2).

$$M^{t}_{\omega,\varphi,\kappa} = R = \begin{bmatrix} \cos\varphi\cos k & -\cos\varphi\sin k & \sin\varphi \\ \cos\omega\sin k + \sin\omega\sin\varphi\cos k & \cos\omega\cos k - \sin\omega\sin\varphi\sin k & -\sin\omega\cos\varphi \\ \sin\omega\sin k - \cos\omega\sin\varphi\cos k & \sin\omega\cos k + \cos\omega\sin\varphi\sin k & \cos\omega\cos\varphi \end{bmatrix} \tag{3.2}$$

where, ω, φ and κ are rotation angles of the turntable coordinates axes (X', Y', Z') about object space coordinates axes (X, Y, Z).

The 6 parameters $(\omega, \varphi, \kappa, X_0, Y_0, Z_0)$ of equation (3.1) define the "exterior orientation parameters" of a panoramic camera.

Equation (3.3) shows the relation of an image point in the linear array coordinate system with respect to an object point in the turntable coordinate system.

$$\begin{pmatrix} X' \\ Y' \\ Z' \end{pmatrix} = R^{t}_{Z'}(\theta) \cdot \lambda \cdot T \cdot \begin{pmatrix} 0 \\ y \\ -c \end{pmatrix} \tag{3.3}$$

with

$$y = (i - \frac{N}{2}) \cdot p_y, \quad \theta = j \cdot p_x \tag{3.4}$$

and

$$T = \begin{pmatrix} 0 & 0 & -1 \\ -1 & 0 & 0 \\ 0 & 1 & 0 \end{pmatrix}$$

where,

p_x…….. angular pixel size of the turntable (rotation angle between two successive linear array image acquisition),
p_y…….. pixel size of the linear array,
c……... camera constant,
N…….. number of pixels in the linear array,
R_Z…… 3D rotation matrix around Z' axis,
T…….. transfer matrix from the linear array to the turntable coordinate system,
($0,y,-c$). image point coordinates in the linear array coordinate system,
(i, j)….. image point coordinates in the pixel coordinate system,
λ ……. scale factor.

Finally, the model which relates image point coordinates (i, j) to the object point coordinates (X, Y, Z), for an ideal sensor becomes as shown in equation (3.5).

$$M_{w,\varphi,k} \cdot \begin{pmatrix} X - X_0 \\ Y - Y_0 \\ Z - Z_0 \end{pmatrix} = R^{t}_{Z'}(\theta) \cdot \lambda \cdot \begin{pmatrix} c \\ 0 \\ y \end{pmatrix} \tag{3.5}$$

3.3 Systematic Errors and Additional Parameters of Panoramic Cameras

In practice a real panoramic camera deviates from the ideal one. These deviations, systematic errors, are modeled by additional parameters. The additional parameters are added to the ideal sensor model in order to compensate for the deviation caused by the systematic errors.

The sources of systematic errors for a panoramic camera are:

- the lens,
- the configuration of the linear array with respect to the optical axis,
- the configuration of the linear array with respect to the turntable rotation axis,
- the turntable itself.

The sources of some of the systematic errors of panoramic cameras are similar to the frame array CCD cameras. Therefore, the same additional parameters are used for the modeling.

The new systematic errors, which only can be observed for panoramic cameras, are explored through the geometrical analysis of the sensor mechanical design and physical measurements of the errors. In addition, image point residuals are analyzed for a better understanding of the behavior of the systematic errors.

With respect to the stability of a panoramic camera, systematic errors can be divided in two different classes:

- stationary systematic errors,
- non-stationary systematic errors.

However, some of the parameters of one class might belong to the other class depending on the stability of the camera system. The aim of this classification is to enable understanding of the sensor behavior and sensor modeling.

3.3.1 Stationary Systematic Errors

The systematic errors that are not varied in time are called stationary systematic errors. These errors remain constant in at least one epoch of data acquisition and over relatively long time. The stationary systematic errors for panoramic cameras are divided into 2 groups as follow:

1. Errors common between frame array CCD and panoramic cameras which are:
   - lens distortions,
   - the shift of principal point,
   - the shift of camera constant.

2. Errors only for panoramic cameras which are
   - affinity of image axes by the correction to the angular pixel size,

- tilt and inclination of the linear array with respect to the rotation axis of the turntable,
- eccentricities of the projection center of the lens with respect to the rotation axis of the turntable and the origin of the turntable coordinate system.

The first group of systematic errors is modeled by a sub-set of Brown's additional parameters (Brown, 1976). A new set of additional parameters is developed for the second group of systematic errors.

Some of the systematic errors of the second group are modeled with respect to the turntable coordinate system. Because of the eccentricities of the projection center from the rotation axis, different turntable coordinate systems can be defined with respect to that for the ideal panoramic camera (Figure 3.2). Therefore, the first step of the error modeling is to define a suitable turntable coordinate system.

3.3.1.1 Turntable Coordinate System

For all possible definitions for the turntable coordinate system, the Z'-axis is always identical to the rotation axis. The origin of the coordinate system is the intersection of the turntable plane and Z'-axis.

The differences between turntable coordinate systems result from the different definitions of X'-axis (Y'-axis is defined based on the definition of X' and Z' axes to construct right-handed coordinate system).

Three meaningful definitions of X'-axis are as follows:

1. X'-axis passes through projection center (Figure 3.3a)
2. X'-axis passes through the linear array (Figure 3.3b)
3. X'-axis is parallel to the optical axis (Figure 3.3c)

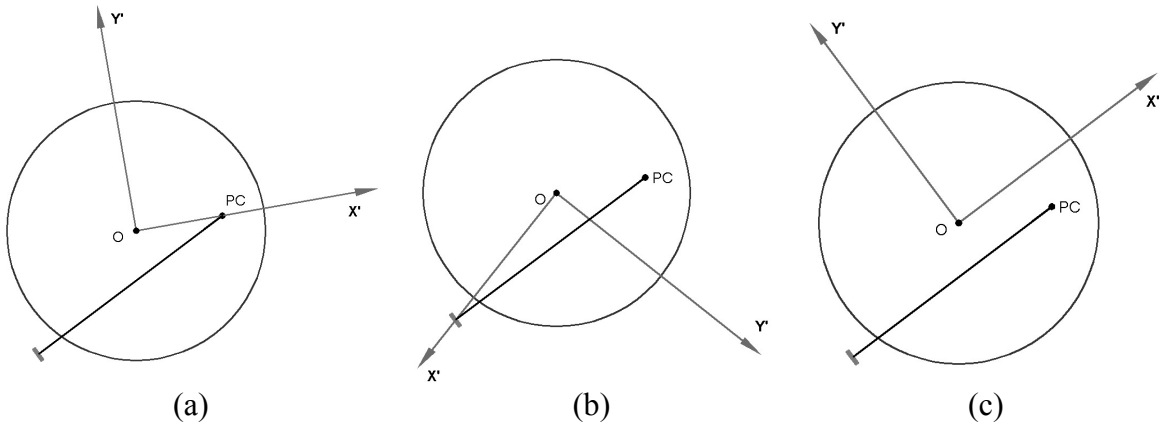

Figure 3.3. Three meaningful definitions of the turntable coordinate system.

The definition of the additional parameters belonging to the eccentricities of the projection center varies with respect to the turntable coordinate system definition. These systematic errors are modeled by:

- 1 eccentricity parameter and 1 parameter indicating the rotation angle of the optical axis with respect to X'-axis (Figure 3.3a),
- 2 eccentricity parameters and 1 constant parameter indicating the rotation angle of the optical axis with respect to X'-axis (Figure 3.3b).
- 2 eccentricity parameters (Figure 3.3c).

The disadvantage of the first coordinate system is the high correlation of the parameter that indicates rotation angle of the optical axis with respect to X'-axis with kappa (an exterior orientation parameter).

The disadvantage of the second coordinate system is that the parameter indicating the rotation angle of the optical axis with respect to the X'-axis should be known in advance, which is not applicable in most cases. Also, this coordinate system inherently has the problem of the first coordinate system.

The third coordinate system does not have the indicated problems of the first and second coordinate systems. Therefore modeling of systematic errors will be based on this coordinate system definition.

3.3.1.2 A New Set of Additional Parameters

The new set of additional parameters consists of the parameters which show the orientation of the linear array with respect to the turntable coordinate system and affinity by the correction to the angular pixel size. Equation (3.6) integrates the new additional parameters into equation (3.5).

$$M_{w,\varphi,k} \cdot \begin{pmatrix} X - X_0 \\ Y - Y_0 \\ Z - Z_0 \end{pmatrix} = R^t_{Z'}(\theta - d\theta) \cdot \left(\lambda \cdot R_{Y'}(ly) \cdot R_{X'}(lx) \cdot \begin{pmatrix} c \\ 0 \\ y \end{pmatrix} + \begin{pmatrix} ex \\ ey \\ ez \end{pmatrix} \right) \tag{3.6}$$

with

$$d\theta = j \cdot dp_x \tag{3.7}$$

where,

$R_{Y'}$, $R_{X'}$.... 3D rotation matrices around Y' and X' axes of the turntable coordinate system,
ex, ey, ez.. the eccentricities of the projection center from the origin of the turntable coordinate axis,
lx, ly……. the inclination and tilt of the linear array with respect to the turntable coordinate axis,
dp_x…….... the correction to the angular pixel size.

Figure 3.4 shows the eccentricities of the projection center, tilt and inclination of the linear array with respect to rotation axes.

In practice, the height of projection center (PC), *ez,* from the plane of the turntable is considered to be known and used as a constant parameter. This is because it has high correlation with Z_0 (an exterior orientation parameter).

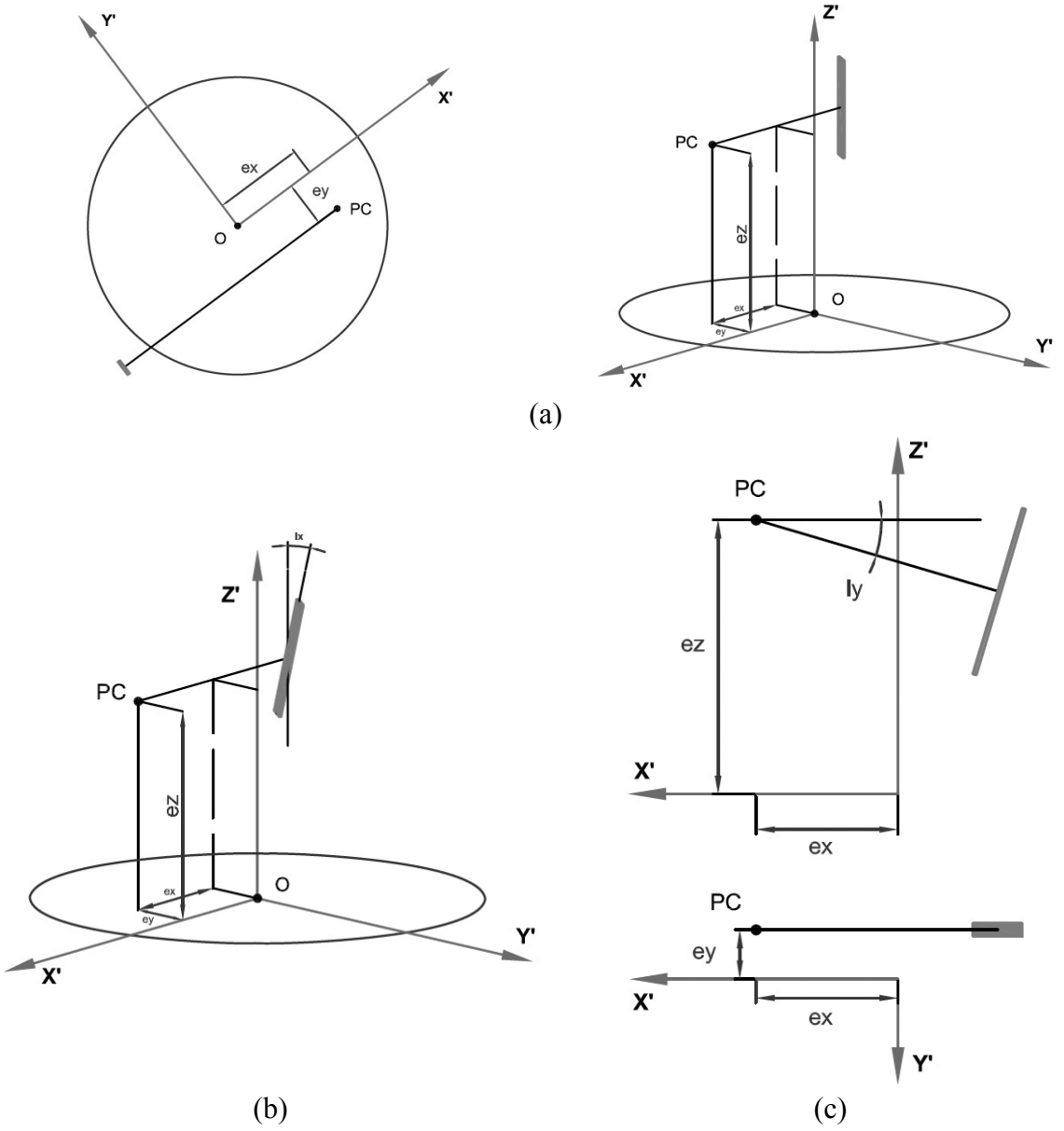

Figure 3.4. Additional parameters for the configuration of the linear array with respect to the turntable coordinate system. (a) Eccentricities, (b) inclination of the linear array, (c) tilt of the linear array with respect to the rotation axis.

3.3.1.3 Brown's Additional Parameters

Brown's set of additional parameters (Brown, 1976) as shown in equation (3.8) are used to model the systematic errors of the camera system along the linear array which are related to the lens itself and the shift of principal point:

$$dy = y_0 + dy_0 + \frac{\bar{y}}{c} \cdot dc + \bar{y} \cdot (r^2 \cdot k_1 + r^4 \cdot k_2) + 2 \cdot \bar{x} \cdot \bar{y} \cdot p_1 + (r^2 + 2 \cdot \bar{y}^2) \cdot p_2 \qquad (3.8)$$

with $\bar{y} = y - y_0$, $\bar{x} = x - x_0$ and $r^2 = \bar{x}^2 + \bar{y}^2$. Where,

x_0, y_0 ..... shift of principal point in the linear array coordinate system,
k_1, k_2 ..... parameters of radial symmetrical lens distortion,
p_1, p_2 .... parameters of decentering lens distortion,
dc ..... correction to the camera constant,
dy_0 ..... correction to the shift of principal point along linear array.

For panoramic cameras, equation (3.8) is reformulated as shown in equation (3.9):

$$dy = y_0 + dy_0 + u_0 \cdot \bar{y} + u_1 \cdot \bar{y}^2 + u_2 \cdot \bar{y}^3 + u_3 \cdot \bar{y}^5 \tag{3.9}$$

where,

$$\begin{aligned} u_0 &= \frac{dc}{c} + 2 \cdot x_0 \cdot p_1 + x_0^2 \cdot (k_1 + x_0^2 \cdot k_2) \\ u_1 &= 3 \cdot p_2 \\ u_2 &= k_1 + 2 \cdot x_0^2 \cdot k_2 \\ u_3 &= k_2 \end{aligned} \tag{3.10}$$

Due to the high correlation of x_0 with kappa (one of the exterior orientation parameters) and dp_x (correction to the angular pixel size), this parameter cannot be determined through self-calibration with bundle adjustment. Therefore this parameter is fixed to a priori value. Assuming that x_0 is a small value and since p_1, x_0^2, k_1 and k_2 are also small values, equations (3.10) are reformulated as shown in equation (3.11):

$$u_0 = \frac{dc}{c} \text{ and } u_2 = k_1 \tag{3.11}$$

Experiences from the self-calibrations of two panoramic cameras (*EYESCAN* and *SpheroCam*) show that the influence of term u_1 is trivial and the maximal u_1 is 0.06 pixel. In these cases the equation (3.12) shows the reduced formulation:

$$dy = y_0 + dy_0 + \frac{\bar{y}}{c} \cdot dc + \bar{y}^3 \cdot (k_1 + k_2 \cdot \bar{y}^2) \tag{3.12}$$

Equation (3.13) shows the integration of the equations (3.12) into equation (3.6).

$$M_{w,\varphi,k} \cdot \begin{pmatrix} X - X_0 \\ Y - Y_0 \\ Z - Z_0 \end{pmatrix} = R^t_{Z'}(\theta - d\theta) \cdot \left(\lambda \cdot R_{Y'}(ly) \cdot R_{X'}(lx) \cdot \begin{pmatrix} c \\ 0 \\ y - dy \end{pmatrix} + \begin{pmatrix} ex \\ ey \\ ez \end{pmatrix} \right) \tag{3.13}$$

3.3.2 Non-Stationary Systematic Errors

The source of non-stationary systematic errors of panoramic cameras is the dynamic mode of image acquisition. These errors are divided into two different groups: non-equal angular pixel size and tumbling.

3.3.2.1 Non-Equal Angular Pixel Size

This error originates from the rotating device of the turntable. The sources of this type of systematic error are:

- non-linear angular velocity of the rotating device,
- inaccurate mechanical rotation axis, which causes the deviations of the trajectory of the projection center from a perfect circle,
- tumbling, which causes a non-uniform friction and leads to change of angular velocity.

In order to understand how to model this systematic error, self-calibrations are applied using the previous additional parameters mentioned at equation (3.13). The Fourier transform of the component of the image space residuals which are perpendicular to the linear array is computed. A high peak of the power spectrum shows that residuals have a periodic behavior and the number of high peaks shows different periods of the oscillation. Based on the Fourier analysis and real self-calibration tests, this error is modeled by the modulation of two sine wave functions with different amplitudes, periods and phases. Equation (3.14) shows the model.

$$\xi = r_0 \cdot \sin(r_1 \cdot \theta + r_2) + r_3 \cdot \sin(r_4 \cdot \theta + r_5) \tag{3.14}$$

where,

r_0 and r_3…. amplitudes,
r_1 and r_4…. periods,
r_2 and r_5…. phases.

Equation (3.15) shows the integration of the equation (3.14) into equation (3.7).

$$d\theta = j \cdot dp_x + \xi \tag{3.15}$$

A non-linear velocity of the rotating device and tumbling are modeled by equation (3.14). In case of the non-linear velocity of the rotating device in one 360° rotation, amplitude shows the maximal variation of the velocity. Period shows the number of maximal positive variation of the velocity. Phase shows the (angular) shift of the sine wave function.

In the case of inaccurate mechanical rotation axis (the imperfect circular rotation of the projection center), proper terms are integrated in order to correct the influence of the change of the eccentricity of the projection center. Since a differential variation of the eccentricity of the projection center has the same influence as the variation of the camera constant and a differential variation of the camera constant can be modeled by scaling the linear array, this error is modeled as shown in equation (3.16):

$$\delta = \bar{y} \cdot (s_0 \cdot \sin(s_1 \cdot \theta + s_2) + s_3 \cdot \sin(s_4 \cdot \theta + s_5)) \tag{3.16}$$

Equation (3.17) shows the integration of the equation (3.16) into equation (3.12).

$$dy = y_0 + dy_0 + \frac{\bar{y}}{c} \cdot dc + \bar{y}^3 \cdot (k_1 + k_2 \cdot \bar{y}^2) + \delta \tag{3.17}$$

For small deviations of the trajectory of the projection center from a circle, this term is negligible and its influence is compensated by tumbling parameters.

3.3.2.2 Tumbling

"Tumbling" or "trunnion axis error" originates from the mechanical properties of the turntable. It is mainly caused by an incorrect and incomplete shape of ball bearings and the contacting surfaces (Matthias, 1961). Tumbling results from imperfect rotation around the vertical axis and shows its effect as a change of the exterior orientation of the camera head during rotation. One of the main effects of the tumbling is the oscillation of the projection center during rotation (Figure 3.5).

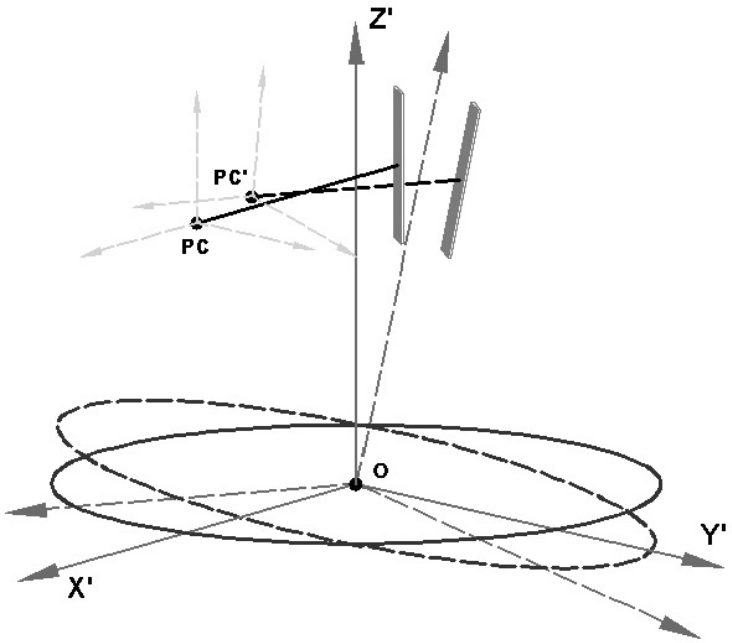

Figure 3.5. Effect of tumbling: the oscillation of the projection center (PC) of the camera.

Tumbling is modeled using:

- an implicit model based on some pure mathematical functions,
- an explicit model based on a physical behavior of the turntable.

The main advantage of explicit model with respect to implicit model is the physical interpretation of the parameters which helps to understand the physical behavior of the sensor. However, if the physical interpretation of the systematic errors is complex, the implicit model is utilized.

3.3.2.2.1 Implicit Model and Patchwise Method

The idea is to use pure mathematical functions which are able to model the non-stationary systematic errors. However, since it is difficult to find a general mathematical function for the modeling of the systematic errors over the whole image space, the image space is divided into patches in order to model the systematic errors of each patch by simple mathematical functions.

The image space is divided into some patches through the analysis of the image point residuals. Each patch contains the residuals of the same pattern and the residuals are modeled by a simple mathematical function. The mathematical function is a polynomial and is written so as to model image point residuals along the row-axis and column-axis of the image. Equation (3.18) shows separate polynomial functions of order 5 for the modeling of row and column image point residuals in each patch.

$$\begin{aligned} F_x &= a_1 + a_2 \cdot x + a_3 \cdot x^2 + a_4 \cdot x^3 + a_5 \cdot x^4 + a_6 \cdot x^5 \\ F_y &= b_1 + b_2 \cdot y + b_3 \cdot y^2 + b_4 \cdot y^3 + b_5 \cdot y^4 + b_6 \cdot y^5 \end{aligned} \tag{3.18}$$

The selection of each patch (the size and location) is done by Fourier or wavelet analysis of the row-axis or column-axis residuals. The patch size selection is influenced by the number of image points and the pattern of the residuals.

In spite of its efficiency in the modeling of systematic errors, generally implicit modeling has the following problems:

- it needs many control points well-distributed in the image space,
- the selection of the mathematical function is required for each patch,
- the selection of the suitable patch size and location in the image space.

In addition, this method has no good performance in case of modeling non-stationary systematic errors. This is because once it is performed for one image, the same parameters and patches cannot be applied for other images of the same camera (without the need for control points). Since tumbling is not a stationary systematic error, this method reduces its efficiency. Therefore another method is investigated.

3.3.2.2.2 Physical Measurement of Tumbling

For a better understanding of the tumbling of panoramic cameras, the inclination of the turntable was measured by an inclinometer. This investigation was done for the *SpheroCam* using the inclinometer, *Zerotronic* from *Wyler Switzerland*, which provides the inclination along one measurement axis.

The inclinometer was placed firmly on the top of the turntable near the gravity center of the camera. Using the operating software for the camera, the inclinations of at least 3 continuous rotations (1080°) of the turntable at every 15° were recorded. The measurements were carried out at 4 different epochs to investigate whether the camera is stationary with respect to time. Figure 3.6 shows the observations for epoch 1. The Fourier analysis of the signal was carried out, which shows a high peak at the period π (Figure 3.6). The analyses of the other epochs show that the camera is not stable over time.

Figure 3.7 shows the observations and the power spectrum of another epoch which has different amplitude, period and phase.

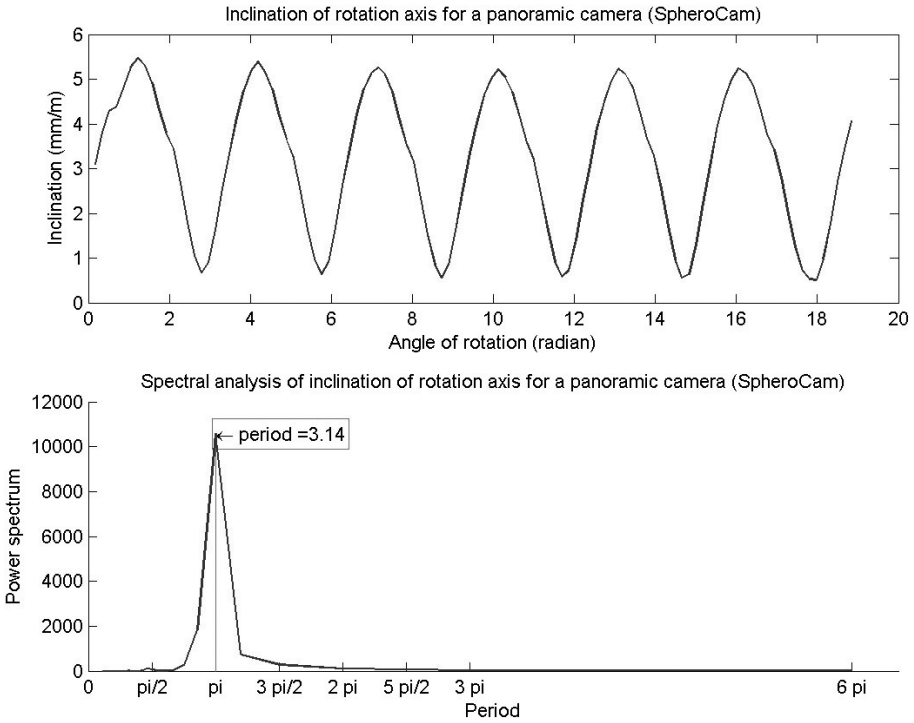

Figure 3.6. Observations of the turntable inclination (top) and the corresponding power spectrum (bottom) for epoch 1.

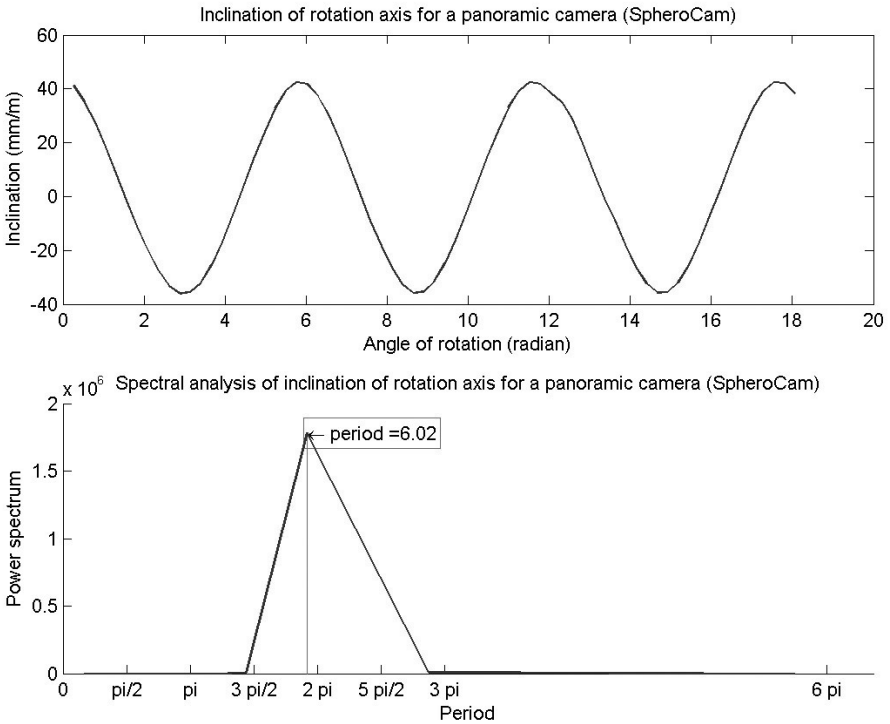

Figure 3.7. Observations for the turntable inclination (top) and the corresponding power spectrum (bottom) for epoch 2.

These measurements indicate that this panoramic camera has tumbling with periodic oscillations. The results of these measurements are used to model tumbling with an explicit model.

3.3.2.2.3 Explicit Model

In practice the physical rotation axis is represented by a cylinder. If we suppose that this axis can be approximated locally by a mathematical straight-line, then the turntable is constrained to have its oscillation around one point on the rotation axis and in the plane of the turntable. With this assumption we suppose that the turntable is constrained to oscillate around the center of the turntable, O (Figure 3.5). Therefore, tumbling can be represented as a rotation of the turntable around a 3D vector at the time of data acquisition. The mathematical formulation of this behavior is presented by the concept of finite rotational axis, "quaternions" or "Euler's parameters".

A quaternion (Hamilton, 1844) is defined as a complex number with one real part and 3 imaginary parts:

$$q = q_0 + q_1 \cdot i + q_2 \cdot j + q_3 \cdot k \tag{3.19}$$

where, $i^2 = j^2 = k^2 = i \cdot j \cdot k = -1$.

It can be used to represent a rotation about the unit 3D vector $\hat{n}$ by an angle θ (Arvo 1994; Hearn and Baker, 1996):

$$q = (s, v) = (\cos(\frac{1}{2} \cdot \theta), \hat{n} \cdot \sin(\frac{1}{2} \cdot \theta)) \tag{3.20}$$

The four components of this quaternion (equation (3.21)) are called Euler's parameters, describing a finite rotation about an arbitrary axis:

$$\begin{aligned} q_0 &= \cos(\frac{\theta}{2}) \\ q_1 &= \hat{n}_x \cdot \sin(\frac{\theta}{2}) \quad q_2 = \hat{n}_y \cdot \sin(\frac{\theta}{2}) \quad q_3 = \hat{n}_z \cdot \sin(\frac{\theta}{2}) \end{aligned} \tag{3.21}$$

where, $\hat{n}_x, \hat{n}_y, \hat{n}_z$ are components of the unit vector $\hat{n}$.

A rotation matrix representing the tumbling of the turntable can be formulated by converting the Euler's parameters to the rotation matrix:

$$R_q = \begin{pmatrix} q_0^2 + q_1^2 - q_2^2 - q_3^2 & 2 \cdot (q_1 \cdot q_2 + q_0 \cdot q_3) & 2 \cdot (q_1 \cdot q_3 - q_0 \cdot q_2) \\ 2 \cdot (q_1 \cdot q_2 - q_0 \cdot q_3) & q_0^2 - q_1^2 + q_2^2 - q_3^2 & 2 \cdot (q_2 \cdot q_3 + q_0 \cdot q_1) \\ 2 \cdot (q_1 \cdot q_3 + q_0 \cdot q_2) & 2 \cdot (q_2 \cdot q_3 - q_0 \cdot q_1) & q_0^2 - q_1^2 - q_2^2 + q_3^2 \end{pmatrix} \tag{3.22}$$

In the case of panoramic cameras, equation (3.23) defines $\hat{n}$ and θ.

$$\begin{matrix} \hat{n}=\hat{n}(t) \\ \theta=\theta(t) \end{matrix} \quad \text{or} \quad \begin{matrix} \hat{n}=\hat{n}(j) \\ \theta=\theta(j) \end{matrix} \tag{3.23}$$

where,

t……. the time,
j..... the number of the column in the pixel coordinate system.

Based on the results of tumbling measurements described in section 3.3.2.2.2, R_q can be simplified as a rotation matrix about the Y'-axis with angle η:

$$R_q = R_{Y'}(\eta) = \begin{pmatrix} \cos(\eta) & 0 & \sin(\eta) \\ 0 & 1 & 0 \\ -\sin(\eta) & 0 & \cos(\eta) \end{pmatrix} \tag{3.24}$$

where,

$$\eta = t_0 \cdot \sin(t_1 \cdot \theta + t_2)$$

If the component of R_q in equation (3.22) around the Z'-axis exists, the parameters of equation (3.14), which are related to the non-equal angular pixel size modeling, can also model this error.

The component of R_q around the X'-axis is not modeled because of its non-efficiency based on real results of self-calibration.

By integration of equation (3.24) into the equation (3.13), equation (3.25) is obtained.

$$M_{w,\varphi,k} \cdot \begin{pmatrix} X - X_0 \\ Y - Y_0 \\ Z - Z_0 \end{pmatrix} = R^t_{z'}(\theta - d\theta) \cdot R_{Y'}(\eta) \cdot \left(\lambda \cdot R_{Y'}(ly) \cdot R_{X'}(lx) \cdot \begin{pmatrix} c \\ 0 \\ y - dy \end{pmatrix} + \begin{pmatrix} ex \\ ey \\ ez \end{pmatrix} \right) \tag{3.25}$$

Equation (3.25) is the general form of bundle equations for panoramic cameras.

3.4 A Sensor Model with Additional Parameters for Panoramic Cameras

In order to eliminate λ from equation (3.25) two different ways are proposed. This is based on two models of the four least squares models (Tienstra, 1956; Gotthardt, 1968) for optimization. The first way is based on the condition model with unknowns (mixed model) in which the observations and unknowns parameters are interrelated. The second way is based on observation model in which observations are as explicit functions of unknown parameters.

3.4.1 Condition Model with Unknowns (Mixed Model)

Equation (3.25) is reformulated by equation (3.26) in order to eliminate λ.

$$\lambda \begin{pmatrix} c \\ 0 \\ y - dy \end{pmatrix} = \begin{pmatrix} P_1 \\ P_2 \\ P_3 \end{pmatrix} \tag{3.26}$$

with

$$\begin{pmatrix} P_1 \\ P_2 \\ P_3 \end{pmatrix} = R^t_{x'}(lx) \cdot R^t_{y'}(ly) \cdot \left(R^t_{y'}(\eta) \cdot R_{Z'}(\theta - d\theta) \cdot M_{w,\varphi,k} \cdot \begin{pmatrix} X - X_0 \\ Y - Y_0 \\ Z - Z_0 \end{pmatrix} - \begin{pmatrix} ex \\ ey \\ ez \end{pmatrix} \right)$$

After elimination of λ, equation (3.27) is constructed. Observations of this equation are the row and column of the image point (i, j) in the pixel coordinate system and are mixed with unknown parameters.

$$\begin{aligned} Fx(U,L) &= 0 - c \cdot \frac{P_2}{P_1} \\ Fy(U,L) &= y - dy - c \cdot \frac{P_3}{P_1} \end{aligned} \tag{3.27}$$

This equation is also considered as an explicit model in (0, y) image point observations in the linear array coordinate system.

The left side of equation (3.27) can be written as shown in equation (3.28).

$$\begin{aligned} Fx(U,L) &= Fx(U|_0, L) + \frac{\partial Fx}{\partial U} \cdot dU + \frac{\partial Fx}{\partial L} \cdot V \\ Fy(U,L) &= Fy(U|_0, L) + \frac{\partial Fy}{\partial U} \cdot dU + \frac{\partial Fy}{\partial L} \cdot V \end{aligned} \tag{3.28}$$

where,

$U|_0$ …. the initial value of unknown vector, *U,*
dU…… Correction to the unknown vector,
L…….. the observation vector,
V…….. the residual vector of the observation vector,
P…….. the weight matrix of observations.

The least squares solution of equation (3.28) is based on equation (3.29) (Vanicek and Krakiwsky, 1986):

$$dU = Q_U \cdot (A^t \cdot M \cdot W) \tag{3.29}$$

with

$$Q_U = (A^t \cdot M \cdot A)^{-1}$$

$$M = B \cdot P^{-1} \cdot B^t$$

$$W = \begin{pmatrix} Fx(U|_0, L) \\ \\ Fy(U|_0, L) \end{pmatrix} \quad A = \begin{pmatrix} \frac{\partial Fx}{\partial U} \\ \\ \frac{\partial Fy}{\partial U} \end{pmatrix} \quad B = \begin{pmatrix} \frac{\partial Fx}{\partial L} \\ \\ \frac{\partial Fy}{\partial L} \end{pmatrix} \tag{3.30}$$

where,

Q_U…… cofactor matrix of unknowns,
A and B… first and second design matrices,
W……. misclosure vector,
P…….. weight matrix of observations.

The main advantages of the mixed model are:

- a simple method of elimination of λ from equation (3.25) through (3.26),
- its complete statistical modeling of the observation equations.

However, it has the following disadvantages with respect to the observation model:

- slower convergence to the optimal solution because of a less steep gradient vector of the "variation function" near to the "solution vector",
- longer computation time with respect to the observation model due to increased matrix operations,
- Complication of the extension of the mixed model for some close-range photogrammetric applications like texture mapping and network design simulations.

Therefore, the observation model is also developed.

3.4.2 The Observation Model

In the first step, for the sake of simplicity, equation (3.3) is considered. From this equation, with the aim of constructing the observation model, equation (3.31) is constructed (see appendix A for more details).

$$\begin{aligned} \theta &= -\tan^{-1}\left(\frac{Y'}{Z'}\right) \\ y &= \frac{c \cdot Z'}{\sqrt{X'^2 + Y'^2}} \end{aligned} \tag{3.31}$$

with (θ, y) at equation (3.4).

The observation model of equation (3.25) that contains additional parameters is obtained similarly to equation (3.31). Equation (3.32) shows this model after simplifications.

$$\begin{aligned} \theta &= -\tan^{-1}\left(\frac{\widetilde{Y}}{\widetilde{Z}}\right) + d\theta \\ y &= \frac{c \cdot \widetilde{Z}}{\sqrt{\widetilde{X}^2 + \widetilde{Y}^2}} + dy \end{aligned} \tag{3.32}$$

with (θ, y) at equation (3.4),

$$\begin{pmatrix} \widetilde{X} \\ \widetilde{Y} \\ \widetilde{Z} \end{pmatrix} = M_{w,\varphi,k} \cdot \begin{pmatrix} X - X_0 \\ Y - Y_0 \\ Z - Z_0 \end{pmatrix} - R^t_{Z'}(\theta) \cdot \begin{pmatrix} ex + ey \cdot \eta + ez \cdot \xi \\ ex \cdot \xi + ey \\ ez - ex \cdot \eta \end{pmatrix} \tag{3.33}$$

and

$$\begin{aligned} d\theta &= d\theta_{dc} + d\theta_{dy_0} + d\theta_{dp_x} + d\theta_{lx} + d\theta_{ly} + d\theta_{lens} + d\theta_{\xi} + d\theta_{\eta} + d\theta_{ex} + d\theta_{ey} \\ dy &= dy_{dc} + dy_{dy_0} + dy_{dp_x} + dy_{lx} + dy_{ly} + dy_{lens} + dy_{\xi} + dy_{\eta} + dy_{ex} + dy_{ey} \end{aligned} \tag{3.34}$$

with the assumption that ζ and η are small angles. This assumption is in agreement with the measurement of tumbling and the estimation of the non-equal angular pixel size from real panoramic camera calibration through self-calibration. Note that *ez* is a constant value and is equal to the height of the projection center from the turntable.

The terms of equation (3.34) are expanded in equations (3.35) and (3.36).

$$\begin{aligned} & d\theta_{dc} = d\theta_{dy_0} = d\theta_{ly} = d\theta_{lens} = d\theta_{\eta} = d\theta_{ex} = d\theta_{ey} = 0 \\ & d\theta_{dp_x} = -j \cdot dp_x \\ & d\theta_{lx} = -\tan^{-1}\left(\frac{\bar{y}}{c} \cdot \sin(lx)\right) \\ & d\theta_{\xi} = -\xi \end{aligned} \tag{3.35}$$

and

$$\begin{aligned} & dy_{dp_x} = dy_{\xi} = dy_{ex} = dy_{ey} = 0 \\ & dy_{dc} = \frac{\bar{y}}{c} \cdot dc \\ & dy_{dy_0} = y_0 + dy_0 \\ & dy_{lx} = \bar{y} \cdot \left(1 - \frac{c \cdot \cos(lx)}{\sqrt{c^2 + \bar{y}^2 \cdot \sin(lx)}}\right) \end{aligned} \tag{3.36}$$

$$dy_{ly} = \frac{\sin(ly)\cdot(\bar{y}^2 + c^2)}{c\cdot\cos(ly) + \bar{y}\cdot\sin(ly)}$$
$$dy_{lens} = \bar{y}^3\cdot(k_1 + k_2\cdot\bar{y}^2)$$

Among these additional parameters, the following cannot be applied to an image point observation without the existence of a corresponding object point:

- *ex* and *ey*: eccentricities of the project center
- ξ and η: non-equal angular pixel size and tumbling parameters

These additional parameters model the shift of the projection center with respect to the origin of the turntable coordinate system and compensate for the oscillation of the projection center because of tumbling. They can be applied to the image point observations by using object space information.

If the object point corresponding to the image point is available, equation (3.37) can be used to correct the image point observations from the systematic errors caused by *ex* and *ey*.

$$\begin{aligned} d\theta_{ex} &= 0 \\ dy_{ex} &= -\frac{y\cdot ex}{\sqrt{X^2+Y^2}} \\ d\theta_{ey} &= \sin^{-1}\left(\frac{ey}{\sqrt{X^2+Y^2}}\right) \\ dy_{ey} &= c\cdot Z\cdot\left(\frac{1}{\sqrt{X^2+Y^2}} - \frac{1}{\sqrt{X^2+Y^2-ey^2}}\right) \end{aligned} \qquad (3.37)$$

3.5 A Sensor Model for Terrestrial Laser Scanners

The developed mathematical model for panoramic cameras offers a flexibility that makes it applicable to other sensors that demonstrate similar geometry to panoramic cameras. By incorporating a preprocessing stage, the sensor model developed for panoramic cameras can also handle the terrestrial laser scanners if the laser scanner has the following two conditions:

- the laser scanner scans the horizontal field of view by horizontal rotation using the turntable,
- the laser scanner provides the intensity images of the backscattered laser light or/and provides measurable geometrical features in the range image like corners, spheres.

Under these conditions the operation of a laser scanner is similar to a panoramic camera. Therefore, it has most of the systematic errors of panoramic cameras. However, a

terrestrial laser scanner with the above conditions has some differences with respect to a panoramic camera due to the mechanical design and operation:

- the laser scanner does not have a linear array. A rotating mirror or prism captures the vertical field of view by rotating around a horizontal axis,
- the laser scanner does not have the same optics as a panoramic camera.

To utilize the previously developed sensor model of panoramic cameras for laser scanners, a virtual linear array is assumed instead of a rotating mirror. The virtual linear array is:

- parallel to the turntable rotation axis,
- orthogonal to the normal vector of the plane containing x and y axes,
- located at a constant non-zero distance from the turntable rotation axis.

Figure 3.8a shows the rotation axis of the turntable and scanning mirror. It also shows the location of the virtual linear array with respect to the rotation axes. Figure 3.8b shows a component of a laser scanner for vertical scanning after 180° rotation of the scanning mirror with respect to its location at Figure 3.8a. Figure 3.9 shows the incoming rays to the virtual linear array.

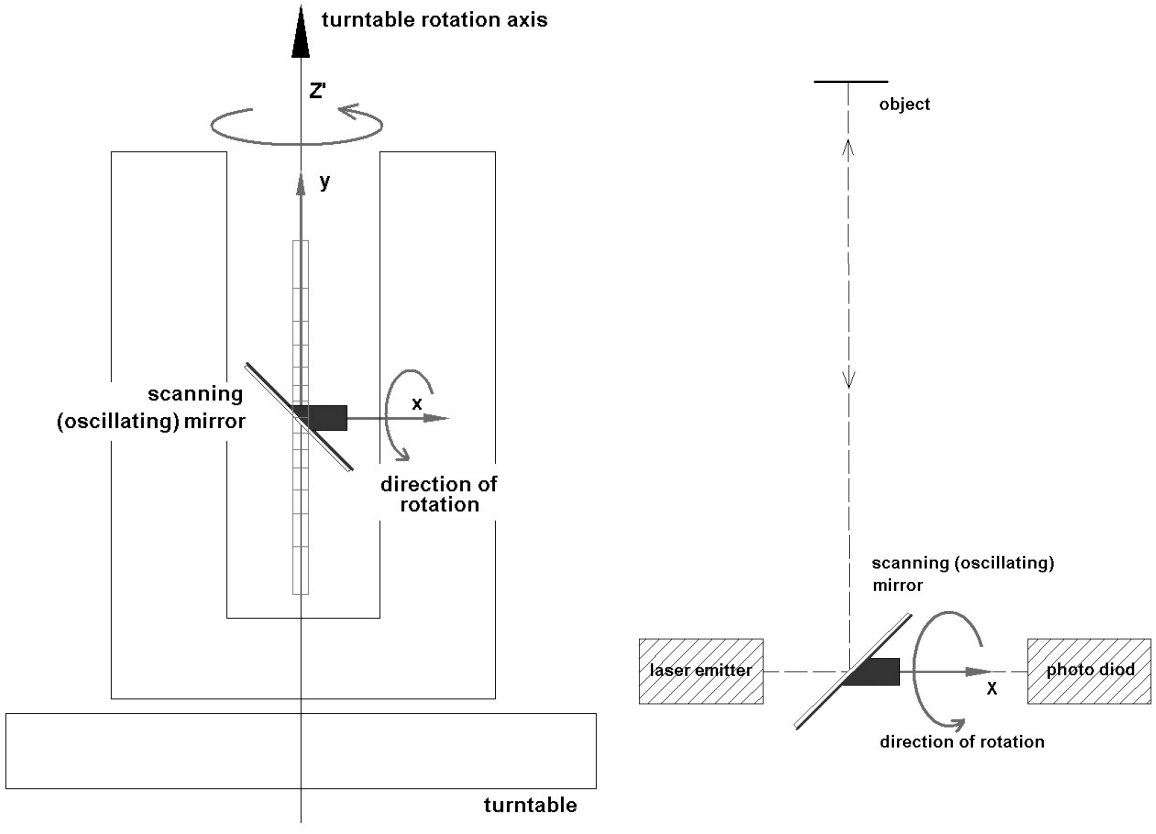

(a) (b)

Figure 3.8. Laser scanner rotation axes. a) Location of the virtual linear array with respect to the turntable and scanning mirror rotation axes. (x, y) is the linear array coordinate system and x is the rotation axis of the scanning mirror. b) A component of the laser scanner for vertical scanning.

The projection along the virtual linear array is not a perspective projection. Due to the spherical geometry of the laser scanner's intensity image, the pixels of the virtual linear array do not have equal sizes. The pixel size on the virtual linear array depends on the distance of the pixel from the center of the virtual linear array (assuming the linear array has finite length). It increases with the distance of the pixel from the center of the virtual linear array. However, given the single ray projection of a terrestrial laser scanner, the angular pixel size of each pixel on the linear array is nominally constant.

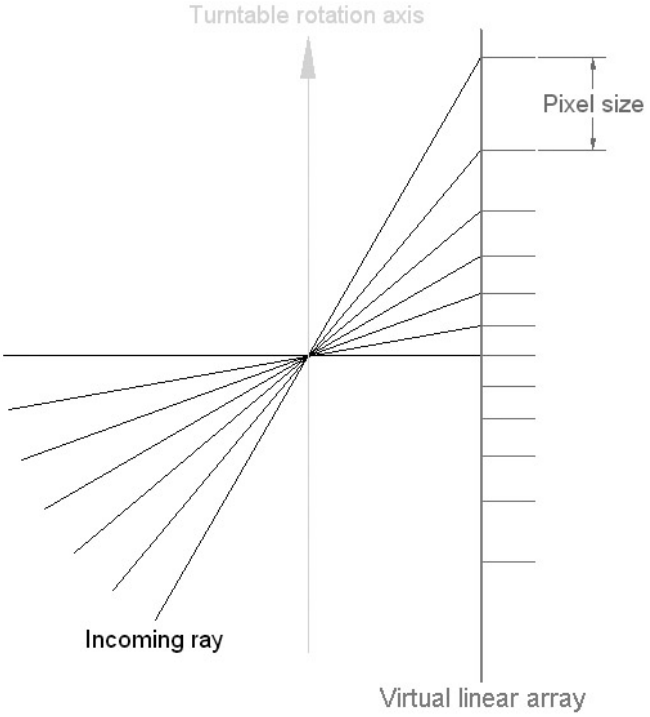

Figure 3.9. The virtual linear array of a terrestrial laser scanner. The pixel size increases by increasing the distance from the center of the virtual linear array.

The sensor model of the ideal laser scanner is similar to equation (3.5) which was already developed for the ideal panoramic camera. However, due to different image geometry with respect to panoramic cameras, minor changes needed to be applied to the sensor model of the ideal panoramic camera. For laser scanners, instead of the perspective projection along the linear array, a single ray projection along the virtual linear array is considered. In addition, the lens is neglected from the sensor model of the ideal panoramic camera. Figure 3.10 shows the projection of the incoming ray into the virtual linear array with φ, the angle of the ray with respect to the orthogonal line to the virtual linear array. Equation (3.38) shows the sensor model of the ideal terrestrial laser scanner.

$$M_{w,\varphi,k} \cdot \begin{pmatrix} X - X_0 \\ Y - Y_0 \\ Z - Z_0 \end{pmatrix} = R^t_{Z'}(\theta) \cdot \lambda \cdot \begin{pmatrix} 1 \\ 0 \\ y \end{pmatrix} \tag{3.38}$$

with

$$y = -\tan(\varphi),\ \varphi = (i - \frac{N}{2}) \cdot p_y$$
$$\theta = j \cdot p_x \tag{3.39}$$

where,

p_x ..... angular pixel size of the turntable,
p_y ..... angular pixel size of the rotating mirror.

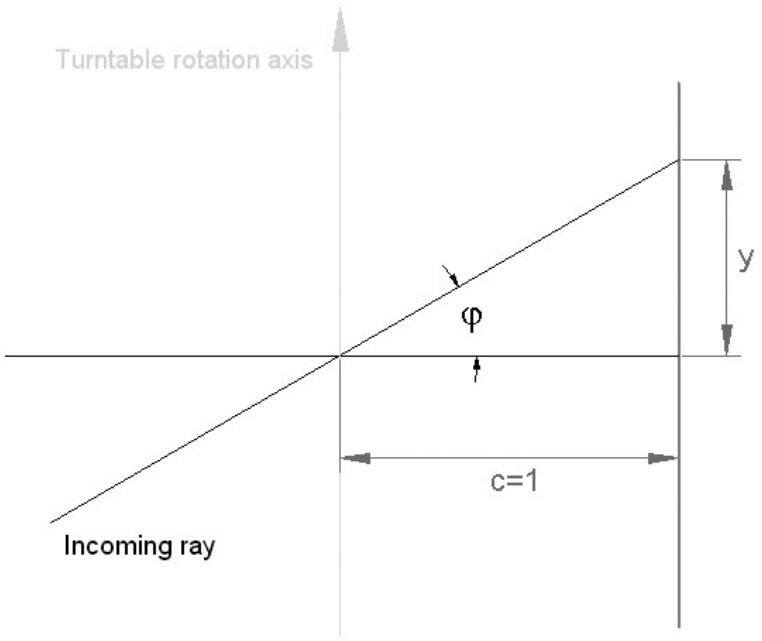

Figure 3.10. The geometry of single ray projection. The figure shows the incoming ray, virtual linear array and rotation axis of the turntable.

For a real laser scanner, the following systematic errors are assumed:

- tilt (Figure 3.11a) and inclination (Figure 3.11b) of the virtual linear array with respect to the rotation axis,
- eccentricities of the projection center from the origin of the turntable coordinate system,
- correction to the horizontal and vertical angular pixel size,
- non-equal angular pixel size,
- tumbling.

It should also be noted that during a time span needed for a single vertical sweep by the mirror, the turntable also rotates. This effectively produces a scan time skew. This skewness produces progressively inclined pattern of the virtual linear array of the laser scanner. Assuming that one vertical scan line takes small time, non-linearity of the skewness can be regarded as being negligible, and hence overall skewness can be taken to be similar to the inclination of the virtual linear array.

Similar to equation (3.32), equation (3.40) shows the observation model for terrestrial laser scanners.

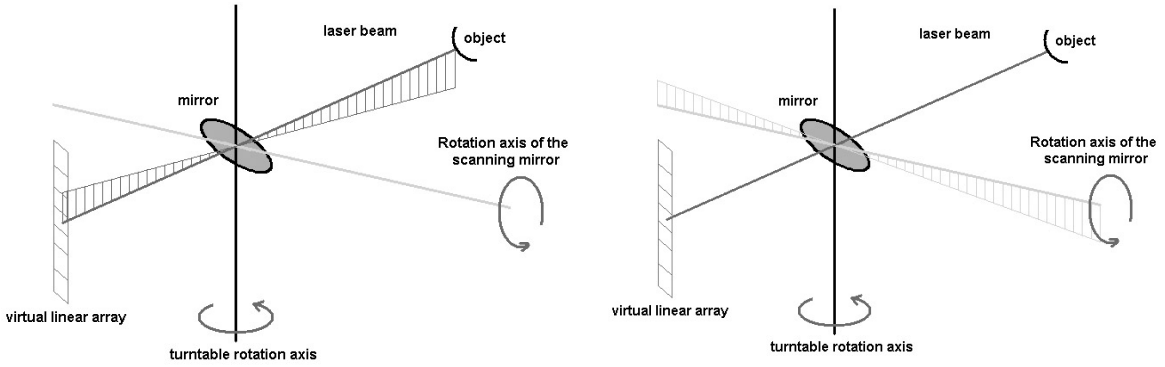

(a) (b)

Figure 3.11. Tilt and the inclination of the virtual liner array. a) The influence of the tilt of the virtual linear array with respect to the turntable rotation axis on the laser beam and b) the influence of the inclination of the virtual linear array with respect to the turntable rotation axis on the rotation axis of the scanning mirror.

$$\begin{aligned} \theta &= -\tan^{-1}\left(\frac{\tilde{Y}}{\tilde{Z}}\right) + d\theta \\ \varphi &= \tan^{-1}\left(\frac{\tilde{Z}}{\sqrt{\tilde{X}^2 + \tilde{Y}^2}} + dy\right) \end{aligned} \tag{3.40}$$

with (θ, φ) in equation (3.39), $(\tilde{X}, \tilde{Y}, \tilde{Z})$ in equation (3.33) and

$$\begin{aligned} d\theta &= d\theta_{dp_x} + d\theta_{dp_y} + d\theta_{lx} + d\theta_{ly} + d\theta_{\xi} + d\theta_{\eta} + d\theta_{ex} + d\theta_{ey} \\ dy &= dy_{dp_x} + dy_{dp_y} + dy_{lx} + dy_{ly} + dy_{\xi} + dy_{\eta} + dy_{ex} + dy_{ey} \end{aligned} \tag{3.41}$$

The terms of equation (3.41) are expanded in equations (3.42) and (3.43).

$$\begin{aligned} d\theta_{ly} &= d\theta_{dp_y} = d\theta_{\eta} = d\theta_{ex} = d\theta_{ey} = 0 \\ d\theta_{dp_x} &= -j \cdot dp_x \\ d\theta_{lx} &= -\tan^{-1}(\tan(\varphi) \cdot \sin(lx)) \\ d\theta_{\xi} &= -\xi \end{aligned} \tag{3.42}$$

and

$$
\begin{aligned}
dy_{dp_x} &= dy_{\xi} = dy_{ex} = dy_{ey} = 0 \\
dy_{lx} &= y \cdot (1 - \frac{\cos(lx)}{\sqrt{1 + y^2 \cdot \sin(lx)^2}}) \\
dy_{ly} &= \frac{\sin(ly) \cdot (y^2 + 1)}{\cos(ly) + y \cdot \sin(ly)} \\
dy_{dp_y} &= \tan(\varphi) - \tan(\varphi - d\varphi) \\
dy_{\eta} &= \frac{\sin(\eta) \cdot (y^2 + 1)}{\cos(\eta) + y \cdot \sin(\eta)}
\end{aligned}
\tag{3.43}
$$

where

$$
d\varphi = (i - \frac{N}{2}) \cdot dp_y \tag{3.44}
$$

3.6 Object Space Constraints

If object space information is available, they can be used with image point observations in the bundle adjustment as constraints and treated as stochastic condition equations (observation equations with associated weights). Three constraints are modeled in this section: 3D straight-lines, the intersection angle of two lines and points that are in the same plane.

3.6.1 3D Straight-Line Constraints

Straight-line features for frame array camera calibration procedures have been used by Brown (1971) who introduced the plumb-line method. Straight-lines were used to derive symmetrical radial and decentering lens distortions. The principle behind this method is that the straightness of the lines in object space should be preserved in image space by perspective projection if an ideal camera is considered. Deviations of a projected straight-line in image space are modeled by additional parameters which are mainly the symmetrical radial and decentering lens distortion parameters. By this method lens distortion parameters of the camera can be estimated. For the estimation of the other additional parameters other methods should be applied.

Kager and Kraus (1976) incorporated geometric constraints such as line constraints, coordinate differences, horizontal and space distances, and angles to improve the traditional bundle adjustment method. Hell (1979) proposed geometric constraints like lines and used these in the form of the coplanarity condition in the bundle adjustment procedure. Van den Heuvel (1999) used parallel and perpendicular straight-lines. In addition to radial lens distortion parameters, van den heuvel estimated the other parameters: shift of principal point and focal length (interior orientation parameters). Mikhail and Weerawong (1994) and Habib et al. (2004) investigated the possibility of using straight-lines for calibration and orientation. They used the model of 3D straight-lines in object space.

The straight-line model for panoramic cameras with no eccentricities of projection center is the same as single-projective center cameras. We used the same concept and extracted a mathematical model with the following advantages:

- the ability to define a weight for each constraint. Each constraint can be treated as a stochastic condition equation,
- the ability to compensate for any small deviation of the 3D straight-line from straightness in object space by adjusting the weight for the condition equation.

A 3D straight-line in object space is defined by two distinct points A and B (Figure 3.12). These points are the intersected rays of the corresponding points in different images. For example, the ray intersection of the image point a1 and a2 is an object point A. In the case of the ideal panoramic camera (no eccentricities of the projection center from rotation axis and with no systematic errors) the projected 3D straight-line is a cylindrical section and for the ideal frame array camera is a straight-line.

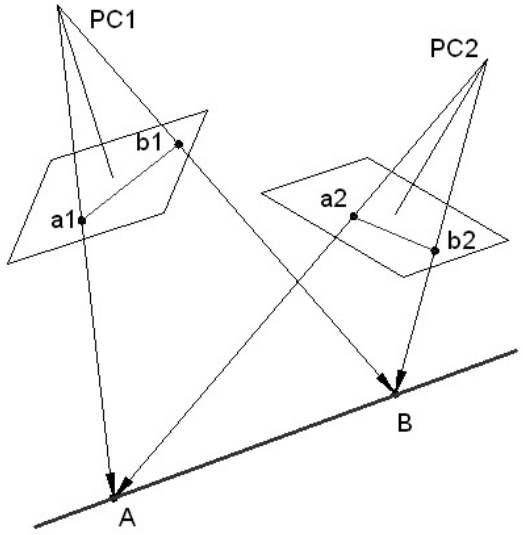

Figure 3.12. Defining a straight-line by the intersection of rays of two distinct corresponding points in different images. The projection centers of the images are denoted by PC1 and PC2.

The intermediate rays, $\vec{V}$, of the segment line AB should be coplanar with the plane defined by $\vec{V}_1$ and $\vec{V}_2$ (Figure 3.13). Equation (3.45) shows the coplanarity equation.

$$(\vec{V}_1 \times \vec{V}_2) \bullet \vec{V} = 0 \tag{3.45}$$

with $\times$ and $\bullet$ denoting the operator of the cross and inner products of two vectors.

Corresponding to this equation, equation (3.46) shows another form of equation (3.45) that is written based on the distance of $\vec{V}$ from the plane of $\vec{V}_1$ and $\vec{V}_2$.

$$s = \frac{\left|a \cdot X + b \cdot Y + c \cdot Z - d\right|}{\sqrt{a^2 + b^2 + c^2}} \tag{3.46}$$

where, $\left|\ \right|$ stands for the absolute value,

a,b,c,d …… parameters of the plane defined by $\vec{V}_1$ and $\vec{V}_2$. The first three parameters are the elements of the normal to the plane. The plane equation is $a \cdot X + b \cdot Y + c \cdot Z = d$,

X,Y,Z ……. coordinates of $\vec{V}$,

s ……... distance of the image point from the plane of $\vec{V}_1$ and $\vec{V}_2$.

Equation (3.46) can be treated as an observation equation model and, in the optimization procedure, s is minimized. The deviation of the 3D straight-line from the straightness and the standard deviation of the image line observations all together define the standard deviation of *s*.

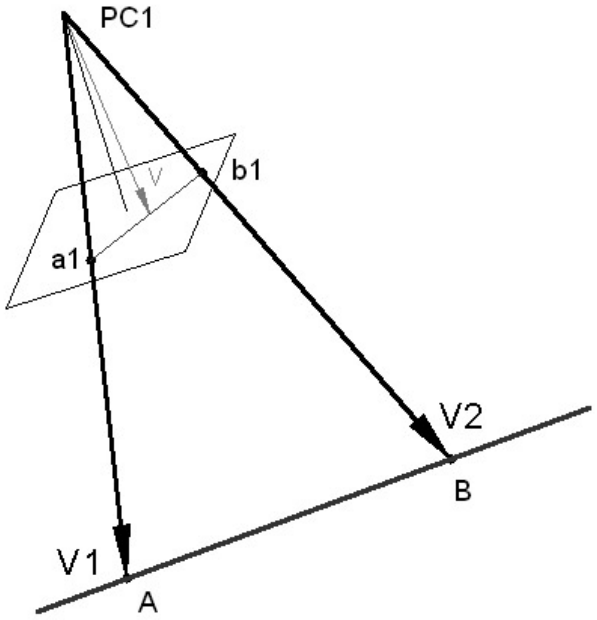

Figure 3.13. Coplanarity condition, the concept of modeling a 3D straight-line for frame array and single projection center panoramic cameras.

Equations (3.45) and (3.46) cannot be applied to multi-projection center images, (for example, a panoramic camera with eccentricities of the projection center from the rotation axis) because the incoming rays of the 3D straight-line span a surface which is not a plane (for single projection cameras this surface is a plane). The projected 3D straight-line in panoramic image space is a modulated sine wave function. Figure 3.14 shows the projection of a 3D straight-line into the panoramic image space with multi projection center because of eccentricity of the projection center from the rotation axis of the turntable.

A 3D straight-line for multi projection center cameras is defined based on the intersection rays of two distinct corresponding points in image space (in order to estimate an initial value for the 3D straight-line parameters). Figure 3.15 shows the definition of a 3D straight-line based on the image point observations which are the same as Figure 3.12.

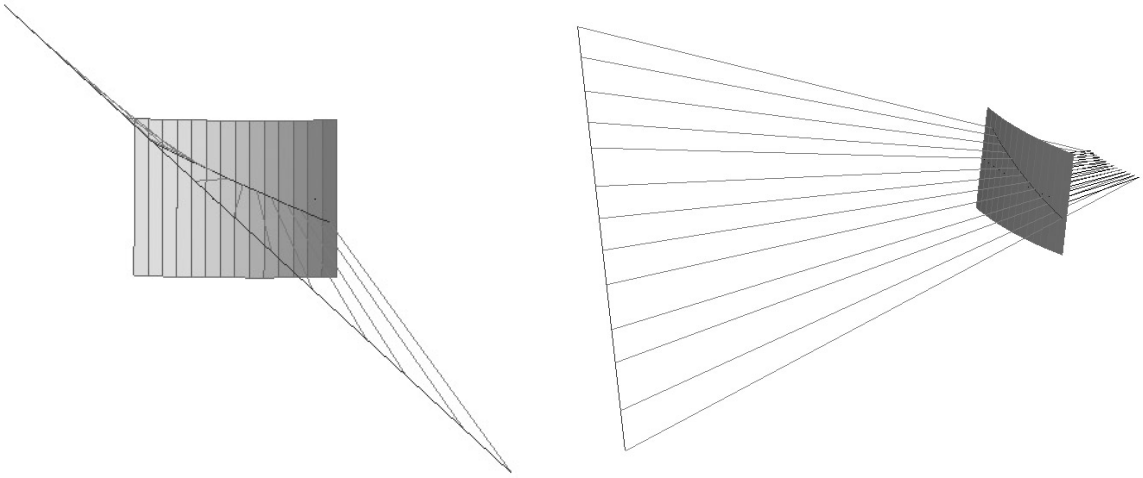

Figure 3.14. Projection of 3D straight-line into a panoramic image. The imaged line is a part of a modulated sine wave function. The surface created by the rays of the 3D straight-line is not a plane.

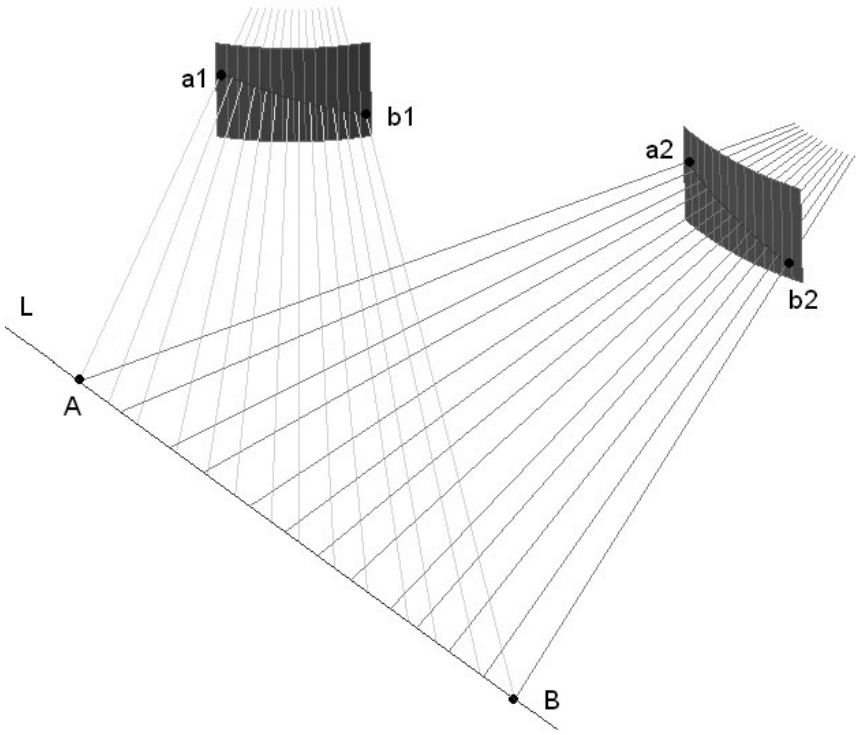

Figure 3.15. Defining a 3D straight-line, L, by the intersecting rays of two distinct corresponding image points in different panoramic images.

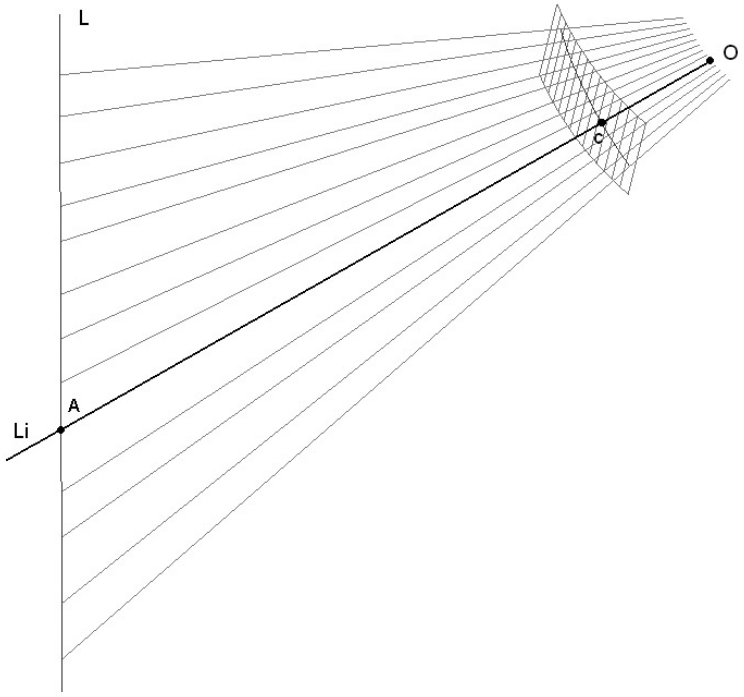

Figure 3.16. Minimizing the Euclidian distance of Li and L, the concept of modeling the 3D straight-line for multi-projection center images. Project center (O), image point (c) and object point on L are collinear. Ideally L and Li intersects at A.

The mathematical model of a 3D straight-line is based on the Euclidian distance, as in equation (3.46). In this case, the minimum distance between the lines Li and L (Figure 3.16) defines the condition equations (3.47) (see appendix B).

$$s = \textit{minimum distance (}\mathrm{L},\ \mathrm{Li}\textit{)} \tag{3.47}$$

The weight of s at the observation equation model (3.47) is defined based on the standard deviation of the image line measurements and the deviations of the 3D straight-line from a perfect 3D straight-line. In the least squares optimization s is minimized. Image space observations are the edge pixels. The unknowns are exterior orientation parameters, additional parameters and 6 parameters of the 3D straight-line.

3.6.2 Lines Intersection Angle Constraints

Two lines L1 and L2 with two direction vectors (m_x, m_y, m_z) and (n_x, n_y, n_z) are defined in the form of equation (3.48). (X_1, Y_1, Z_1) and (X_0, Y_0, Z_0) are two arbitrary points on L1 and L2.

$$\begin{aligned} L1 &: \frac{X - X_1}{m_x} = \frac{Y - Y_1}{m_y} = \frac{Z - Z_1}{m_z} = t \\ L2 &: \frac{X - X_0}{n_x} = \frac{Y - Y_0}{n_y} = \frac{Z - Z_0}{n_z} = t' \end{aligned} \tag{3.48}$$

The acute angle between these lines is used as a constraint. However, if the standard deviation of the angle is known a condition equation can be established in the form of equation (3.49) and the standard deviation can be used to define the weight of the observation.

$$\alpha = \cos^{-1}\left(\frac{\vec{V}_1 \bullet \vec{V}_2}{\sqrt{(\vec{V}_1 \bullet \vec{V}_1)\cdot(\vec{V}_2 \bullet \vec{V}_2)}}\right) \tag{3.49}$$

where, $\vec{V}_1 = \begin{pmatrix} m_x & m_y & m_z \end{pmatrix}^t$, $\vec{V}_2 = \begin{pmatrix} n_x & n_y & n_z \end{pmatrix}^t$ and α is the intersection angle.

The observation is α, the angle between to lines. Unknowns are the parameters of the 3D straight-lines.

3.6.3 Coplanarity Constraints of 3D Points

If a set of points is approximated by a plane, it is modeled by the distance of 3D points from the plane. Equation (3.50) shows the distance of a point from a plane.

$$dis = \frac{a \cdot X + b \cdot Y + c \cdot Z - d}{\sqrt{a^2 + b^2 + c^2}} \tag{3.50}$$

where,

$a \cdot X + b \cdot Y + c \cdot Z = d$ …….. the equation of the plane,
(*a, b, c*)……... the normal vector to the plane
(*X, Y, Z*)…….. the coordinates of the point.

In the least squares optimization the weight for observation equation (3.50) is defined based on the standard deviation of the distance of the points from the plane.

The observation is *dis,* the distance of a point to the plane. Unknowns are the coordinates of the coplanar points and parameters of the plane.

4

Sensor Calibration through Self-Calibration and Accuracy Tests

4.1 Introduction

The camera calibration was performed through self-calibration for two panoramic cameras and a laser scanner. For better analysis of the sensor behaviors, in the first step of the investigation the condition model with unknowns (mixed model) for least squares adjustment was used (see section 3.4.1). The observation model for least squares adjustment was used in the second step after successful modeling of the systematic errors in the first step.

The self-calibration was performed in three ways:

- space resection of individual images using a specific testfield of control points,
- block triangulation,
- block triangulation with object space constraints.

This chapter reports the result of panoramic cameras and a laser scanner calibration through self-calibration. The results are related to the observation model of least squares.

In section 4.2, two panoramic testfields are introduced. In section 4.3, the result of self-calibration through space resection is given. In this section, the result of the implicit and explicit modeling for compensating the non-stationary additional parameters will be shown. The results are presented for two panoramic cameras, *EYESCAN* and *SpheroCam* and a laser scanner, *Imager 5003* of *Zoller+Fröhlich* with laser scanner's intensity image. In section 4.4 the result of self-calibration by block adjustment and accuracy test is given for two panoramic cameras. In section 4.5 the possibility of the self-calibration of a panoramic camera by means of object space constraints, in this case 3D straight-lines, for estimating all additional parameters will be shown.

4.2 Panoramic Testfields of Control Points

Panoramic testfields of control points were used because of the 360° horizontal field of view of panoramic cameras and other sensors operating similar to panoramic camera. This section introduces two panoramic testfields.

4.2.1 ETH Zurich Panoramic Testfield

We established a panoramic testfield in ETH Zurich (testfield of ETH Zurich). Figure 4.1 shows the control points of this testfield which are distributed regularly in the 360° horizontal field of view. The control points are the center of 2.4 cm circular targets which are made of aluminum. The bases of targets are white and the contrasts are black. Some targets were stuck to the ceiling for the case of using wide vertical field of view lenses with the panoramic camera. Figure 4.2 shows a panoramic image from this testfield.

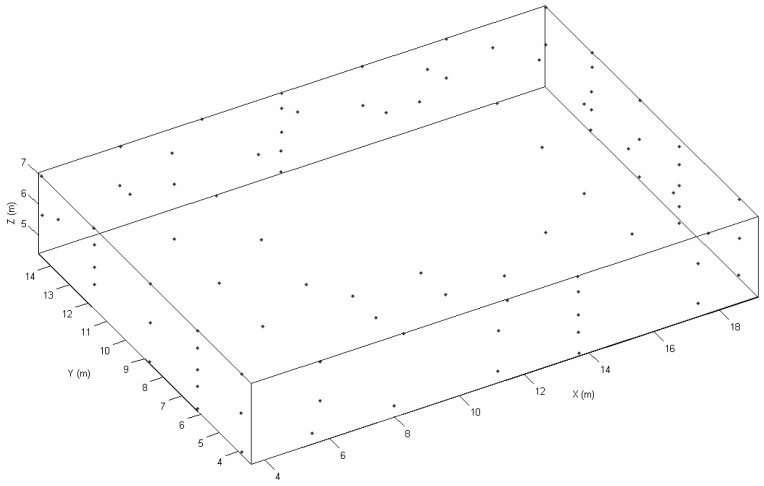

Figure 4.1. ETH Zurich panoramic testfield with 96 control points distributed homogeneously over the field of view of the panoramic camera.

Figure 4.2. A cylindrical panoramic image of the panoramic testfield of ETH Zurich.

Table 4.1 shows the specifications of the panoramic testfield. It consists of 96 control points. The dimensions of the testfield environment are 15 m x 12 m x 3 m. Control points of the testfield are the center of circular targets. They have been measured by a theodolite *TC2002* from at least 3 stations with a sufficient base line (more than 2 meters) at the distance of maximal 4 meters. The mean standard deviation of the control points of 3D network adjustment of horizontal and vertical angle observations are 0.3 mm, 0.3 mm and 0.1 mm for X, Y and Z coordinates, respectively. The mean standard deviation of the depth and lateral coordinates are 0.32 mm and 0.22 mm.

Table 4.1. Specifications of the ETH Zurich panoramic testfield.

Total number of targets	96
Dimensions of the testfield environment	15 m x 12 m x 3 m
Target size (mm)	24
Mean/max std. dev. (X,Y,Z) (mm)	0.3 / 0.9 , 0.3 / 0.8 , 0.1 / 0.3
Depth and lateral std. dev. (mm)	0.32, 0.22

4.2.2 TU Dresden Panoramic Testfield

Another panoramic testfield which is established in Technical University of Dresden (testfield of TU Dresden) was used in this investigation. Figure 4.3 shows the distribution of the control points and Table 4.2 shows the specification of the testfield.

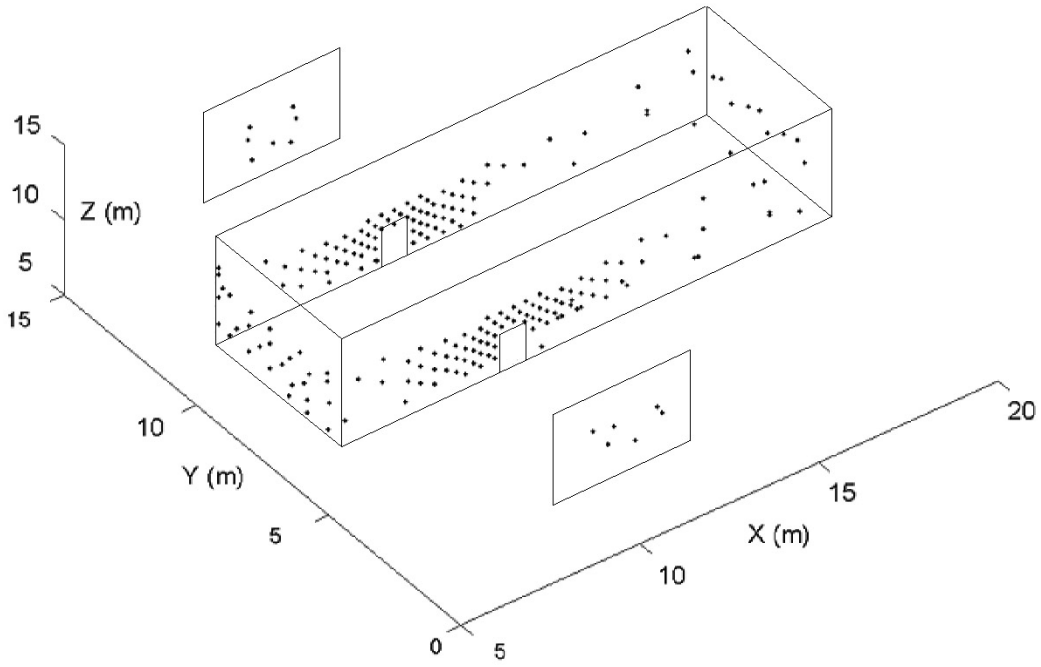

Figure 4.3. TU Dresden panoramic testfield with more than 200 control points distributed over the filed of view of the panoramic camera (*Courtesy D. Schneider, TU Dresden*).

The control points of this testfield are the centers of the retro-reflective targets. They have been measured by the photogrammetric method using a frame array CCD camera. The dimensions of the testfield environment are 14 m x 5 m x 3 m. The mean standard

deviation of the control points' coordinates are 0.2 mm, 0.3 mm and 0.1 mm for X, Y and Z coordinates, respectively. The depth and lateral standard deviations are 0.37 mm and 0.20 mm, respectively.

Figure 4.4. A cylindrical panoramic image from the panoramic testfield of TU Dresden (*Courtesy D. Schneider, TU Dresden*).

Table 4.2. Specifications of the TU Dresden panoramic testfield.

Total number of targets	224
Dimensions of control network	14 m x 5 m x 3 m
Target size (mm)	10 and 20
Mean/max std. dev. (X,Y,Z) (mm)	0.2 / 0.7 , 0.3 / 4.5 , 0.1 / 0.9
Depth and lateral std. dev. (mm)	0.37, 0.20

4.3 Self-Calibration through Space Resection

The self-calibration was performed using panoramic testfields by space resection. This method was used for investigation of the behavior of the camera system and systematic errors through image space residual analysis of the control points. Two panoramic cameras and a laser scanner were calibrated using space resection.

4.3.1 Panoramic Cameras

Two panoramic cameras were studied in this investigation, *EYESCAN* and *SpheroCam*. For the calibration of the *EYESCAN* the panoramic testfield of TU Dresden and for the calibration of *SpheroCam*, panoramic testfield of ETH Zurich was used.

4.3.1.1 EYESCAN

We received the image point and object point coordinates from D. Schneider, TU Dresden. The focal length of the panoramic camera in this investigation is 35 mm. The weight of observations for least squares bundle adjustment is a unit weight matrix for image point observations. The unit of image point observations is pixel.

Additional parameters were added sequentially one by one to the least squares bundle adjustment to observe the influence of the additional parameters on the modeling of systematic errors. Table 4.3 shows this procedure. Figure 4.5 shows the image space residuals at step 8. Some local systematic errors are visible in the image space of this figure.

The systematic errors that appear in Figure 4.5 were modeled and reduced by post processing the image space residuals using the patch-wise method (described in 3.3.2.2.1). The image point observations were corrected from systematic errors by a polynomial of up to order 3 for each patch. Tests of additional parameters were performed and only the significant coefficients of the polynomials were used in the modeling of each patch. The bundle adjustment was performed with the modified image point observations. Figure 4.6 shows the image space residuals. The region between vertical lines shows the patches. The unit of the image point observation is pixel and the obtained $\hat{\sigma}_0$ (*a posteriori* standard deviation) is 0.23 (Table 4.3).

Table 4.3. Effect of additional parameters in systematic errors modeling of *EYESCAN*. The unit of the image point observation is pixel.

Description of parameters	**Parameters**	$\hat{\sigma}_0$
1) Exterior orientation	$\omega, \varphi, \kappa, X_0, Y_0, Z_0$	19.94
2) Correction to the camera constant and shift of principal point along linear array	dc, dy_0	8.16
3) Symmetrical radial lens distortion	k_1, k_2	4.90
4) Eccentricities of projection center from rotation axis	ex, ey	3.68
5) Tilt of linear array with respect to the rotation axis	ly	2.00
6) Inclination of linear array from rotation axis	lx	2.00
7) Correction to the angular pixel size (affinity)	dp_x	1.62
8) Non-equal angular pixel size	$r_0, r_1, r_2, r_3, r_4, r_5$	0.65
Patchwise method		
9a) Two polynomials for modeling image space residuals.	up to 3rd order	0.23
Or		
9b) Tumbling	t_0, t_1, t_2	0.41

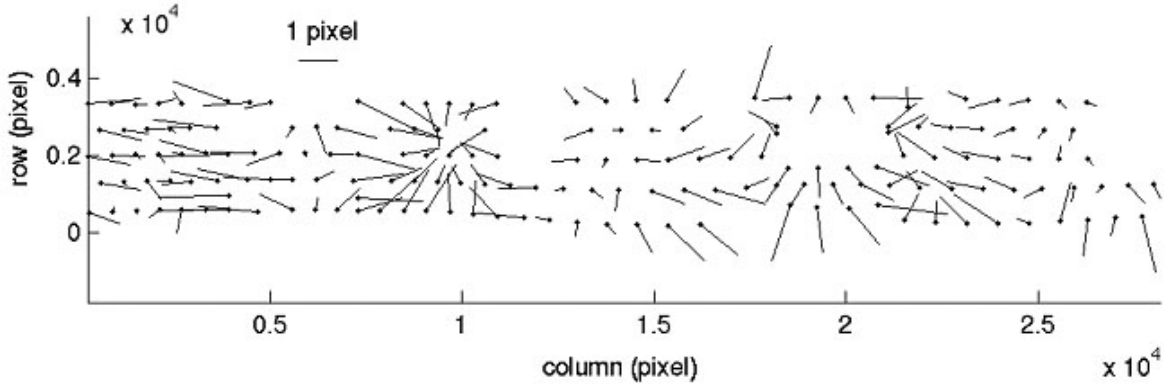

Figure 4.5. Image space residuals after using additional parameters corresponding to the results after step 8 in Table 4.3. $\hat{\sigma}_0$ is 0.65 (the unit of the image point observation is pixel).

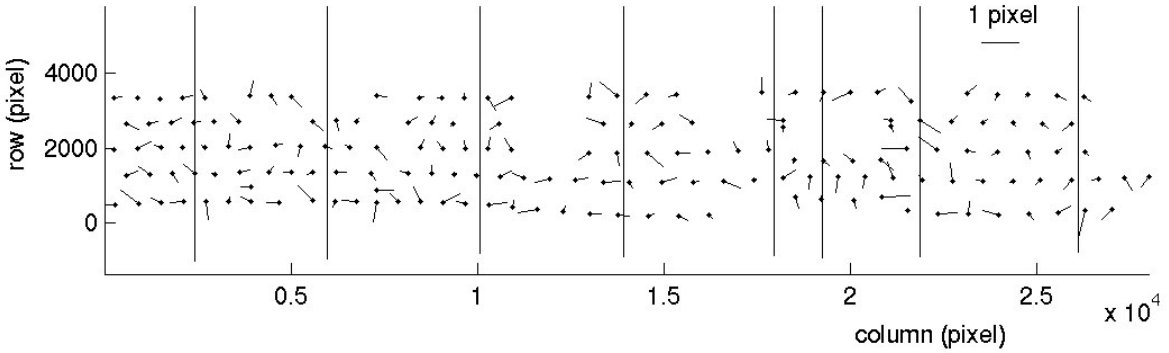

Figure 4.6. Image space residuals of patch-wise method corresponding to the results after step 9a in Table 4.3. The vertical lines show the border of each-patch. $\hat{\sigma}_0$ is 0.23 (the unit of the image point observation is pixel).

We faced two problems with this implicit model and patchwise method. The number and the size of patches were not identical to the number and size of patches of the other images which were taken from the same panoramic camera. Due to the non-stationary behavior of these systematic errors, the patchwise procedure should be repeated for each image separately. Therefore, for each image acquisition, a testfield of well-distributed control points is necessary, which restricts the applicability of this type of modeling in real applications.

The Fourier analysis of the residuals in image space showed a high peak in the power spectrum, which indicates an oscillation of the linear array during image acquisition by *EYESCAN*. In the next step we used the explicit model of tumbling. Bundle adjustment was performed with additional parameters including tumbling parameters. In this case, $\hat{\sigma}_0$ was 0.41 (Table 4.3). Figure 4.7 shows the image space residuals after using all additional parameters.

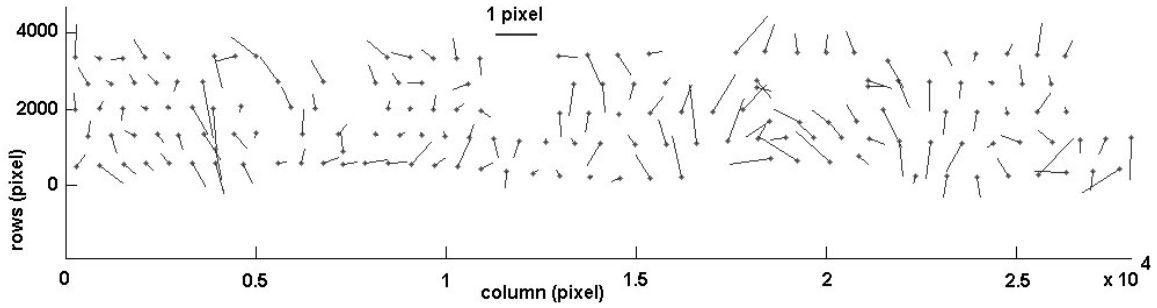

Figure 4.7. Image space residuals after using all additional parameters corresponding to the results after step 9b in Table 4.3. $\hat{\sigma}_0$ is 0.41 (the unit of the image point observation is pixel).

The result of explicit modeling was not better than the patchwise method but it has the advantage of fewer parameters than the implicit model and the patchwise method.

The comparison of the estimated additional parameters through space resection for 5 images of *EYESCAN* showed that the phase parameters of the sine wave functions for the modeling of non-equal angular pixel size and tumbling were significantly different.

4.3.1.2 SpheroCam

The focal length of the panoramic camera in this investigation is 50 mm. The weight matrix of the image point observations was a unit weight matrix and the unit of the image point observations is pixel.

Similar to the *EYESCAN*, self-calibration was performed by adding additional parameters in steps. Table 4.4 shows the influence of additional parameters on the modeling of systematic errors. A huge reduction of $\hat{\sigma}_0$ at two steps is obvious. The first is after the addition of the parameter for the correction of the angular pixel size. The second is after addition of the non-equal angular pixel size and tumbling parameters. Improvement by factor 6 is obvious in the last step. Figure 4.8 shows the image space residuals of the last step.

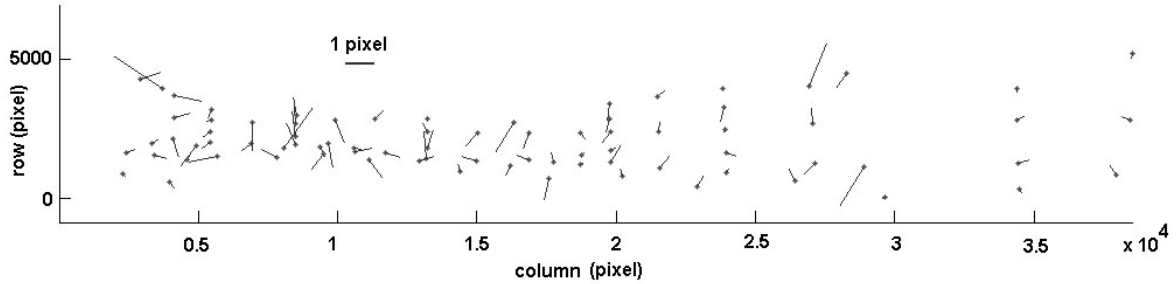

Figure 4.8. Image space residuals after using all additional parameters. $\hat{\sigma}_0$ is 0.52 (the unit of the image point observation is pixel).

The comparison of the estimated additional parameters through space resection for 7 images of *SpheroCam* showed that the following parameters are not stationary and significantly different:

- all parameters of the non-equal angular pixel size and tumbling (9 parameters),
- the correction to the angular pixel size (1 parameter),

The main reason for change in the additional parameters is the mechanical instability of the turntable of the *SpheroCam*. The *SpheroCam* was mainly designed for acquiring images of high radiometric quality. However, by modeling the systematic errors it can also be used for measurement applications.

Table 4.4. Effect of additional parameters on systematic error modeling of *SpheroCam*. The unit of the image point observation is pixel.

Description of parameters	Parameters	$\hat{\sigma}_0$
1) Exterior orientation	$\omega, \varphi, \kappa, X_0, Y_0, Z_0$	143.30
2) Correction to the angular pixel size	dp_x	14.09
3) Correction to the camera constant	dc	8.16
4) Correction to the shift of principal point along linear array	dy_0	7.25
5) Eccentricities of projection center from rotation axis	ex, ey	4.90
6) Tilt and inclination of linear array with respect to the rotation axis	ly, lx	4.16
7) Symmetrical radial lens distortion	k_1, k_2	3.11
8) Non-equal angular pixel size and tumbling	$r_0, r_1, r_2, r_3, r_4, r_5$ t_0, t_1, t_2	0.52

4.3.2 Laser Scanner – Imager 5003

The extended sensor model of panoramic cameras (see section 3.5) was used for the calibration of the *Imager 5003* from *Zoller+Fröhlich*[1]. For this purpose, self-calibration was performed through space resection of individual images. Table 4.5 shows the specifications of the intensity image and some initial additional parameters.

Table 4.5.Specifications of the *Imager 5003* and its intensity image.

Intensity image format (row, column) (pixel)	10,000 x 20,264
Angular pixel size of the turntable and rotating mirror	0.018°
Image geometry	Spherical

The acquired results of the self-calibration are based on the analysis of 5 different intensity images of the laser scanner. Two images were taken from the panoramic testfield ETH Zurich, while the laser scanner was mounted on top of a firm and stable pillar. Due to the high absorption of the laser light, there were some blunders in the intensity image of the black targets (see Figure 4.9), so the measurement of the target centers was not precise. The *a posteriori* standard deviation of unit weight for image point observations (in pixel) was 0.30 after using all additional parameters.

[1] http://www.zofre.de/e_index.html

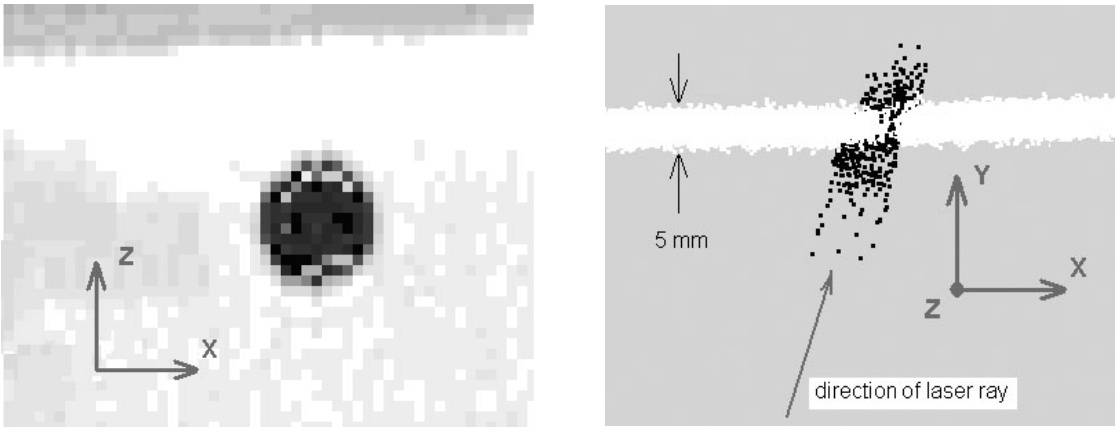

(a) (b)

Figure 4.9. Due to the high absorption of the laser light with black materials, blunders were appeared inside the black circular targets. a) The laser intensity image of a black target with white pixels as blunders and b) the point cloud corresponding to the same target (at 90° rotated view) deviating from the plane of target along the laser ray (the point cloud of the base of the target has 5mm noise).

To get a better intensity image of the targets we established a new panoramic testfield by changing the target size and color in the same environment at the same locations of the existing panoramic testfield. Due to the characteristics of the laser light, white circular targets were used with black color as background. Table 4.6 briefly describes the new panoramic testfield and Figure 4.10 shows a typical laser intensity image of the laser scanner from this testfield.

Table 4.6.Specifications of the panoramic testfield.

Number of control points	63
Dimensions of the testfield (X,Y,Z) (m)	15 x 12 x 3
Mean std. dev. of control points along X,Y and Z axes (mm)	0.3, 0.2, 0.1
Max. std. dev. of control points along X,Y and Z axes (mm)	0.7, 0.5, 0.2

(a) (b)

Figure 4.10. a) A typical intensity image of the *Imager 5003* laser scanner from the new panoramic testfield of ETH Zurich and b) a zoomed window of the intensity image of targets 10 meters away from the scanning station.

Three images where taken from the new panoramic testfield. One image was acquired while the laser scanner was mounted on top of a firm and stable pillar and two images were acquired while the laser scanner was mounted top of a wooden surveying tripod. Self-calibration was performed for these three images. The case that a firm and stable pillar was used had the lowest *a posteriori* unit weight variance of the three. The reason is likely to be instability of the tripod during the operation of the laser scanner.

The laser scanner orientation was performed with the intensity images. Additional parameters were added in steps for self-calibration. In each step, the correlation analysis and significance tests of the estimated parameters were performed. Table 4.7 shows the a posteriori standard deviation of unit weight for image point observations at each step.

The *a posteriori* standard deviation of unit weight for image point observations ($\hat{\sigma}_0$) is reduced to 0.15 in the last step by including non-equal angular pixel size and tumbling parameters. From Table 4.7 it can be concluded that the most influential parameter is the correction to the horizontal angular pixel size of the laser scanner.

Table 4.7. Effect of additional parameters on the systematic errors modeling of *Imager 5003*. The unit of the image point observation is pixel.

Description of parameters	Parameters	$\hat{\sigma}_0$
1) Exterior orientation parameters	$\omega, \varphi, \kappa, X_0, Y_0, Z_0$	2.74
2) Correction to the angular pixel size of the rotating mirror	dp_y	2.42
3) Correction to the angular pixel size of the turntable	dp_x	0.29
4) Eccentricities of scan center from rotation axis	ex, ey	0.28
5) Tilt and inclination of the virtual linear array with respect to the rotation axis	ly, lx	0.22
6) Non-equal angular pixel size and tumbling	$r_0, r_1, r_2, r_3, r_4, r_5$ t_0, t_1, t_2	0.15

The residuals of the image point observations in image space are shown in Figure 4.11. A local systematic pattern of residuals is obvious in the middle of the image. This may be related to non-modeled mechanical errors of the laser scanner system.

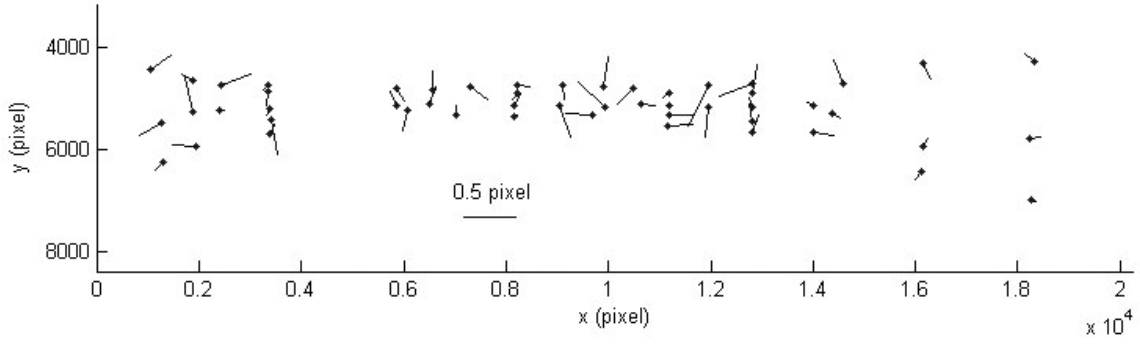

Figure 4.11. Image space residuals of the image point observations of *Imager 5003*.

4.4 Self-calibration by Block Triangulation and Accuracy Tests

Self-calibration by block triangulation is used for two reasons:

- It does not need more control points than a minimal constraints datum. This case is investigated for panoramic cameras in section 4.4.1. Providing a testfield of control points in real projects for self-calibration is not economical and is time consuming.

- In the case of using a suitable and strong geometrical network, it allows more reliable and precise determination of additional parameters compared to self-calibration by space resection. The measured control point coordinates of a testfield are not error free. The errors in the control points cause poor determination of the additional parameters. It is explained in chapter 6.

Bundle block adjustment was performed by considering the frame- and block-invariant additional parameters of panoramic cameras. The weight matrix of image point observations was the unit weight matrix in all cases. The unit of image point observations was the pixel.

Because of non-convergence of the least squares solution to a unique and correct solution, non-equal angular pixel size and tumbling parameters (9 parameters) were fixed to the values which were already estimated through space resection. Tumbling parameters can be estimated where a sufficient number of control points exists in the self-calibration process.

4.4.1 EYESCAN

Self-calibration and accuracy tests were performed for the *EYESCAN* by block triangulation using 5 camera stations. Because of limited dimension of the testfiled along the Y-axis the camera stations were placed approximately inline in order to obtain sharp and focused images from the closer targets. This configuration is not optimal for point positioning.

In order to investigate the minimal number of control points for self-calibration, a datum was defined by 3 control points. For accuracy tests 151 check points were defined among visible and accurate measured targets. Non-equal angular pixel size and the tumbling parameters were considered as fixed values determined by space resection and the other additional parameters were unknowns. Because of high correlation of the correction of the camera constant (*dc*) with object point coordinates, self-calibration and object point coordinates determination cannot be performed correctly. The RMSEs from check points in this situation were 8.2 mm, 4.9 mm and 31.6 mm for X, Y and Z coordinates. To resolve this problem, *dc* was fixed to the value that was estimated through bundle block adjustment using an over-constrained datum of all control points. Figure 4.12 shows the stations of the panoramic camera, the location of the control points, check points and the object space residuals for check points.

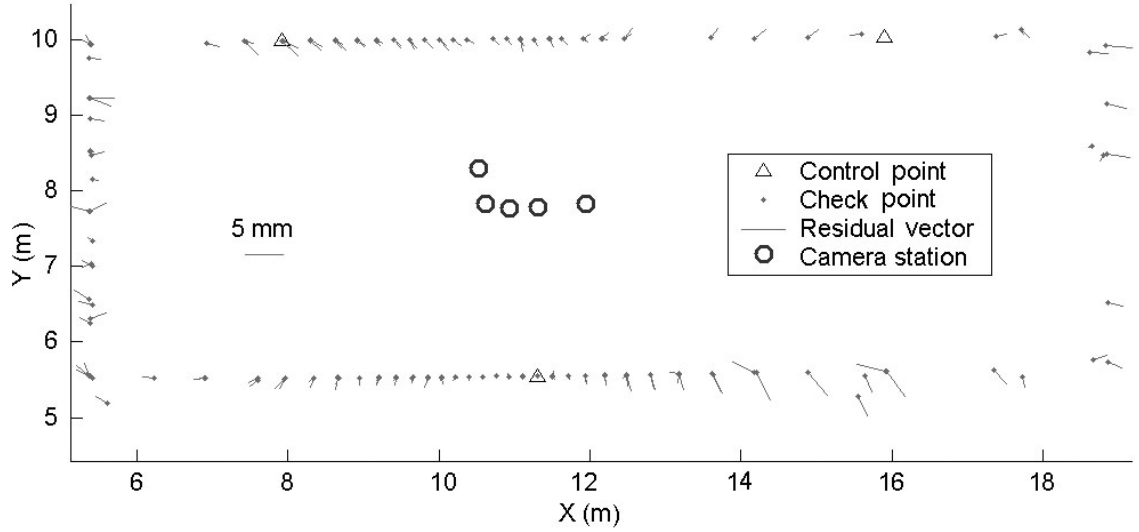

(a)

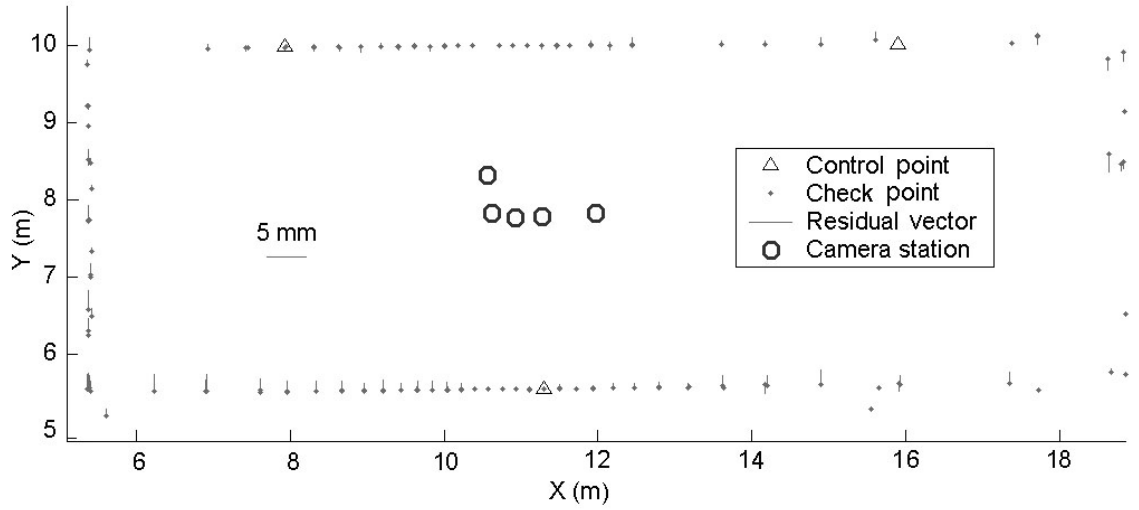

(b)

Figure 4.12. The configuration of the *EYESCAN* stations and object space residuals of check points. a) Object space residuals of check points for the X and Y axes in the XY-plane. b) Object space residuals of check points for the Z axis in the XY-plane.

Table 4.8 shows the result summary of the self-calibration and accuracy test. The RMSEs from check points are 1.22 mm, 1.04 mm and 0.84 mm for X, Y and Z coordinates respectively. These are reasonable in comparison to the standard deviations and show the influence of additional parameters in the modeling.

To show the degradation in accuracy that results from not modeling the non-equal angular pixel size and tumbling errors, self-calibration of the same network was performed using 8 additional parameters with *dc* fixed to the previously determined value. Table 4.9 shows the result of computation.

Table 4.8. Results of the accuracy test (with the inclusion of fixed tumbling and non-equal angular pixel size parameters determined by space resection) for the network of *EYESCAN*. The unit of the image point observation is pixel.

Number of check points	151
Datum definition	over-constrained using 3 control points
RMSEs of check points coordinates (X,Y,Z) (mm)	1.22, 1.04, 0.84
Std. dev. of check points coordinates (X,Y,Z) (mm)	1.58, 0.60, 0.54
$\hat{\sigma}_0$	0.16

Table 4.9. Results summary of accuracy test (without the tumbling and non-equal angular pixel size parameters) for the network of *EYESCAN*. The unit of the image point observation is pixel.

Number of check points	151
Datum definition	over-constrained using 3 control points
RMSEs of check point coordinate (X,Y,Z) (mm)	9.72, 3.72, 3.60
Std. dev. of check points coordinates (X,Y,Z) (mm)	1.68, 0.64, 0.60
$\hat{\sigma}_0$	0.17

The RMSE of check point coordinates in Table 4.9 with respect to the case that tumbling was modeled (Table 4.8) is worse by a factor of 9 along the X-axis, 3 along the Y-axis and 4 along the Z-axis.

4.4.2 SpheroCam

Self-calibration was also performed by block triangulation for *SpheroCam*. 4 panoramic images were taken from different stations. The datum definition of the network was based on inner constraints using all available control points for eliminating 7 datum defects. For accuracy test purposes 87 check points among visible and measured targets were defined.

In this case, 9 parameters of non-equal angular pixel size and tumbling were fixed to the value already estimated by space resection. Self-calibration was performed and the RMSEs of check point coordinates were 1.76 mm, 1.39 mm and 6.04 mm for X, Y and Z coordinates respectively. Because of a high correlation of the correction of the camera constant with the Z coordinates of the object points, the estimation of the Z coordinates were degraded. To solve this problem, the correction of camera constant (*dc*) was fixed to the value that was estimated by a block triangulation with over-constrained datum using all control points. Self-calibration and accuracy tests were performed.

Figure 4.13 shows the object space residuals of check points and location of the *SpheroCam* stations. Figure 4.13a shows the check points' residuals of the X and Y coordinates in the XY-plane. Figure 4.13b shows the check points' residuals along the Z coordinates in the XY-plane.

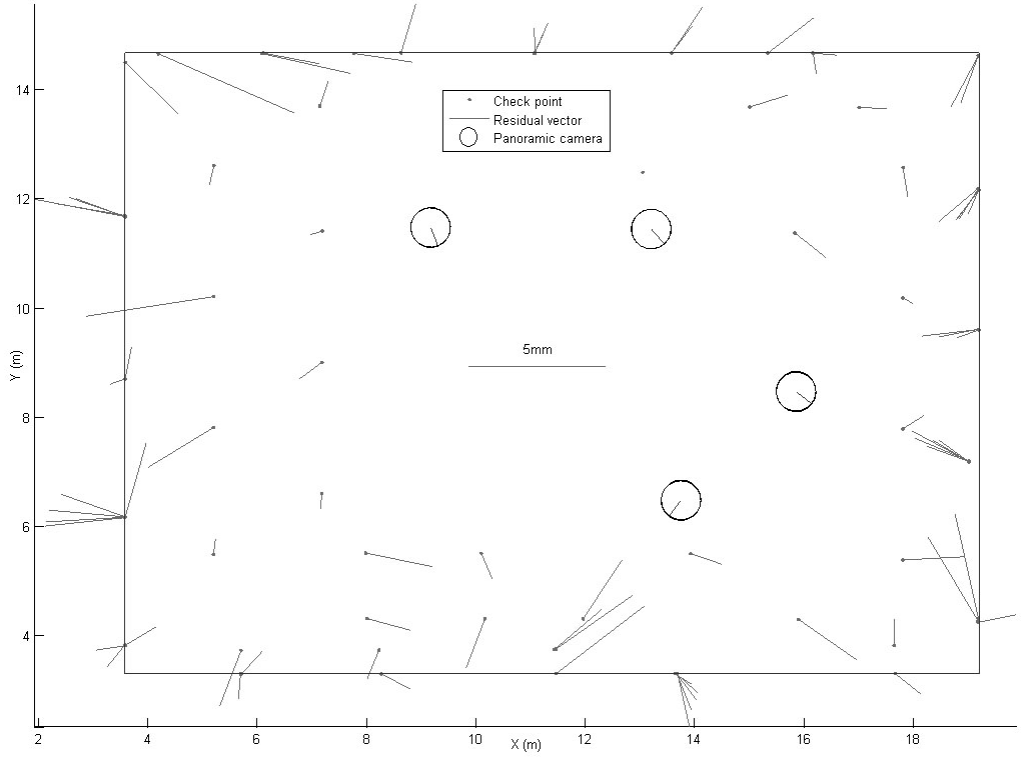

(a)

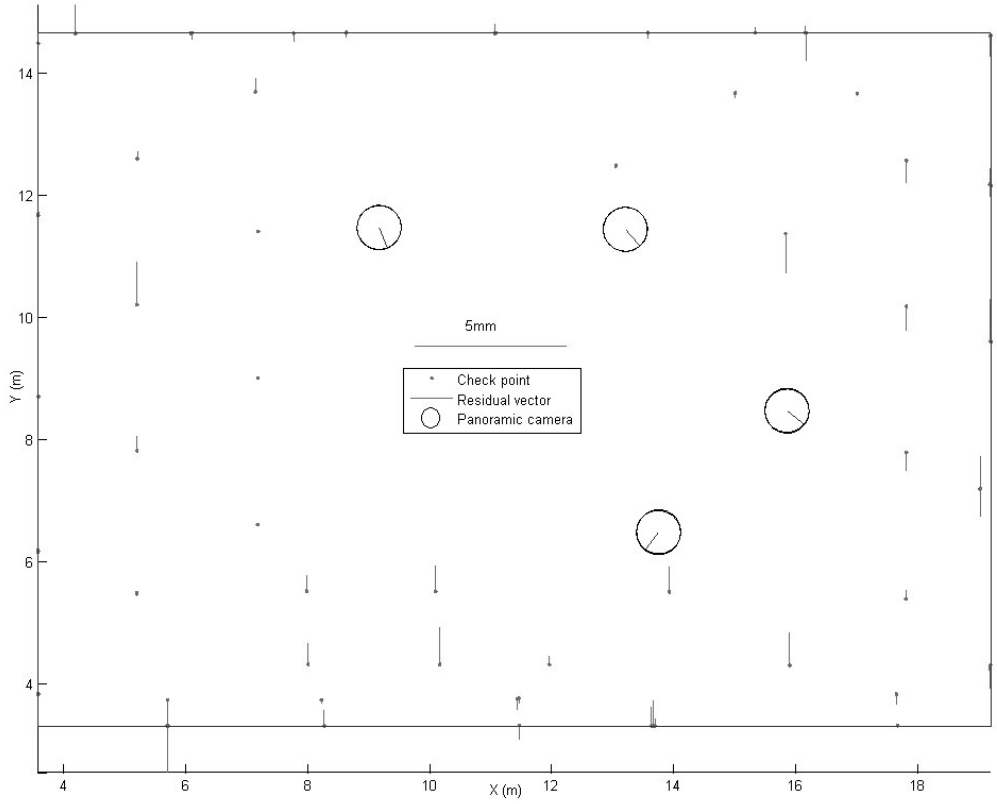

(b)

Figure 4.13. The network configuration of the *SpheroCam* stations and object space residuals of check points coordinates. a) Object space residuals of check points for X and Y coordinates in the XY-plane. b) Object space residuals of check points for Z coordinate in the XY-plane.

Table 4.10 shows the results of the self-calibration and accuracy test. The RMSEs of check point coordinates of this network are 1.65 mm, 1.2 mm and 0.61 mm along the X, Y and Z coordinate axes respectively. Compared to the standard deviations, those are reasonable and show the influence of additional parameters in the modeling of systematic errors.

Table 4.10. Results of accuracy test (with the inclusion of fixed tumbling and non-equal angular pixel size parameters determined by space resection) for the network of *SpheroCam* images.

Number of check points	87
Datum definition	inner constraints using 87 control points
RMSEs of check point coordinates (X,Y,Z) (mm)	1.65, 1.20, 0.61
Std. dev. of check point coordinates (X,Y,Z) (mm)	1.16, 0.92, 0.41
$\hat{\sigma}_0$	0.52

To show the degradation in accuracy that results from non-modeling of non-equal angular pixel size and tumbling errors, the self-calibration of the same network was performed using 8 additional parameters with *dc* fixed to the already determined value. Table 4.11 shows the results of computation.

Table 4.11. Results of accuracy test (without the tumbling and non-equal angular pixel size parameters) for the network of *SpheroCam* images. The unit of the image point observation is pixel.

Number of check points	87
Datum definition	Inner constraints using 87 control points
RMSEs of check points coordinates (X,Y,Z) (mm)	9.92, 10.14, 2.51
Std. dev. of check points coordinates (X,Y,Z) (mm)	3.44, 2.73, 1.27
$\hat{\sigma}_0$	0.54

Comparing the RMSEs of check points coordinates of Table 4.11 with respect to the case that tumbling was modeled (Table 4.10) shows the degradation by a factor of 6 along the X-axis, 9 along the Y-axis and 3 along the Z-axis.

4.5 Self-Calibration by Block Triangulation and Object Space Constraints

Non-equal angular pixel size and tumbling parameters of panoramic cameras cannot be determined through block triangulation with minimal constraints datum. This problem does not occur when camera calibration is performed by block triangulation (bundle) or space resection using a sufficient number of control points. In other words, an over-constrained datum with many control points (for example 100 control points) is needed, which is not practical or economical.

In the previous section it has been shown that when the additional parameters of non-equal angular pixel size and tumbling are known in advance, self-calibration is possible with minimal constraints datum. However, in many cases the parameters of the tumbling modeling are not available in advance. Since the mathematical sensor model is highly non-linear, the unknown parameters are a lot, also the existence of many local minima at the goal function of the least squares, the divergence and oscillation of the bundle adjustment solution happens due to insufficient constraints. Therefore other constraints are included in the solution in order to restrict the oscillation and provide the convergence of the solution. For that an over-constrained datum is defined by using object space constraints like 3D straight-lines.

The 3D straight-line observations of this investigation are the existing features in the workspace area, panoramic testfield of ETH Zurich (Figure 4.14). The edges of the existing desks (Figure 4.15), doors and picture frames were selected as 3D straight-lines in object space. These line features in the panoramic images were measured to sub-pixel precision after chaining the extracted edges by the Canny edge operator. Figure 4.16 shows an example of sub-pixel extracted edges of the desks.

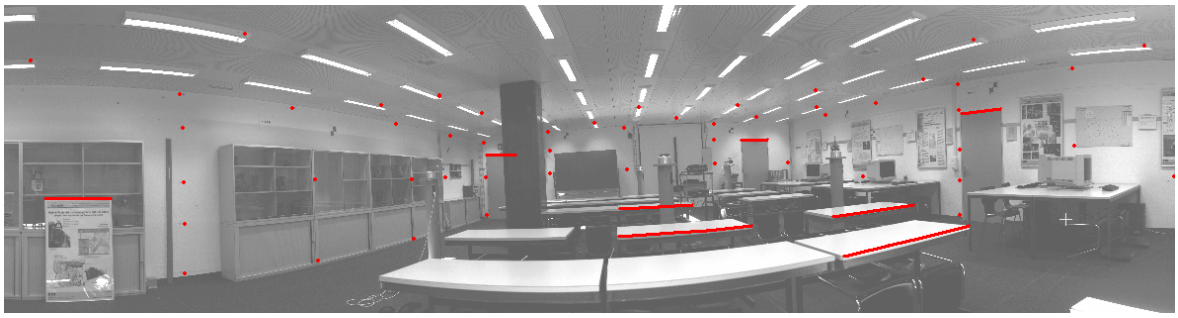

Figure 4.14. Distribution of the 3D straight-lines. 8 straight-lines were measured at the edges of the desks, the frame of a picture and the edges of doors. This figure also shows the distribution of tie points.

The corresponding edge points in image space were measured by intersecting the straight-line edge segments (Figure 4.17). These points were introduced as new points in the bundle block adjustment for defining the 3D straight-lines in the object space. In other words, the object space coordinates of these new points were used to define the initial values of the 3D straight-line parameters.

The corresponding image edges are added to the bundle adjustment using equation (3.47) as stochastic constraints. 8 straight-lines in object space were defined and measured in 4 panoramic images. The average length of the projected 3D straight-lines in the images is 400 pixels. In addition, tie point observations were added to the bundle equations.

The inner constraints datum for resolving 7 datum defect was defined by existing object points which are in this case the coordinates of the control points. Note that datum is inner constraints and the individual control points are not used in the bundle adjustment. For the accuracy test 87 check points were defined.

Figure 4.15. An example of 3D straight-line feature: borders of the desks.

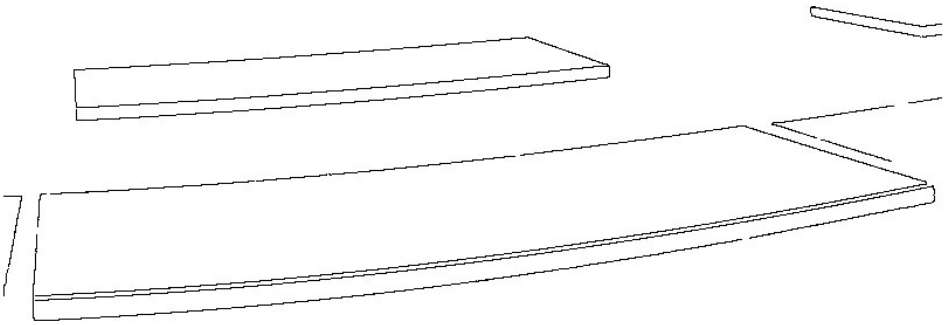

Figure 4.16. Sub-pixel extracted edges of the desks boundaries after removing non-relevant edges.

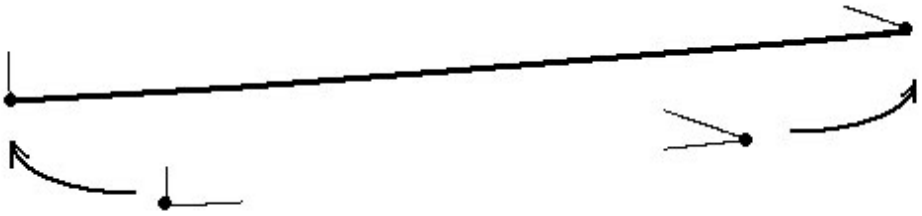

Figure 4.17. Defining the edge points by intersecting the straight-line edges at the corner. These points are measured at all panoramic images and used to determine the initial values of the 3D straight-lines.

Because of high correlation of the correction of the camera constant (*dc*) with the Z coordinate of the object points, *dc* was fixed to a priori value which was already estimated by a block triangulation with over-constrained datum. The bundle block adjustment was performed using all additional parameters while correction to the angular pixel size and non-equal angular pixel size and tumbling parameters were block-variant. Bundle adjustment did not converge to a solution and oscillation occurred because of using too many unknowns in the adjustment and the existence of many local minima at the goal function of the least squares solution. In order to solve this problem only the period of the

tumbling was considered as a block-invariant parameter. Bundle adjustment was performed and the results were successful.

Table 4.12 shows the results of self-calibration by using 3D straight-line constraints and tie point observations. Figure 4.18 shows the object space residuals of check points and the distribution of the 3D straight-lines in object space.

Table 4.12. Results of the bundle block adjustment using 3D straight-line constraints. The units of the image point and line observations are pixel.

Datum	Inner constraints
Number of check points	87
Number of 3D straight-lines (in object space)	8
RMSEs of check point coordinates (X,Y,Z) (mm)	1.68, 1.80, 0.80
Std. dev. of check point coordinates (X,Y,Z) (mm)	1.10, 0.81, 0.32
$\hat{\sigma}_0$	0.40

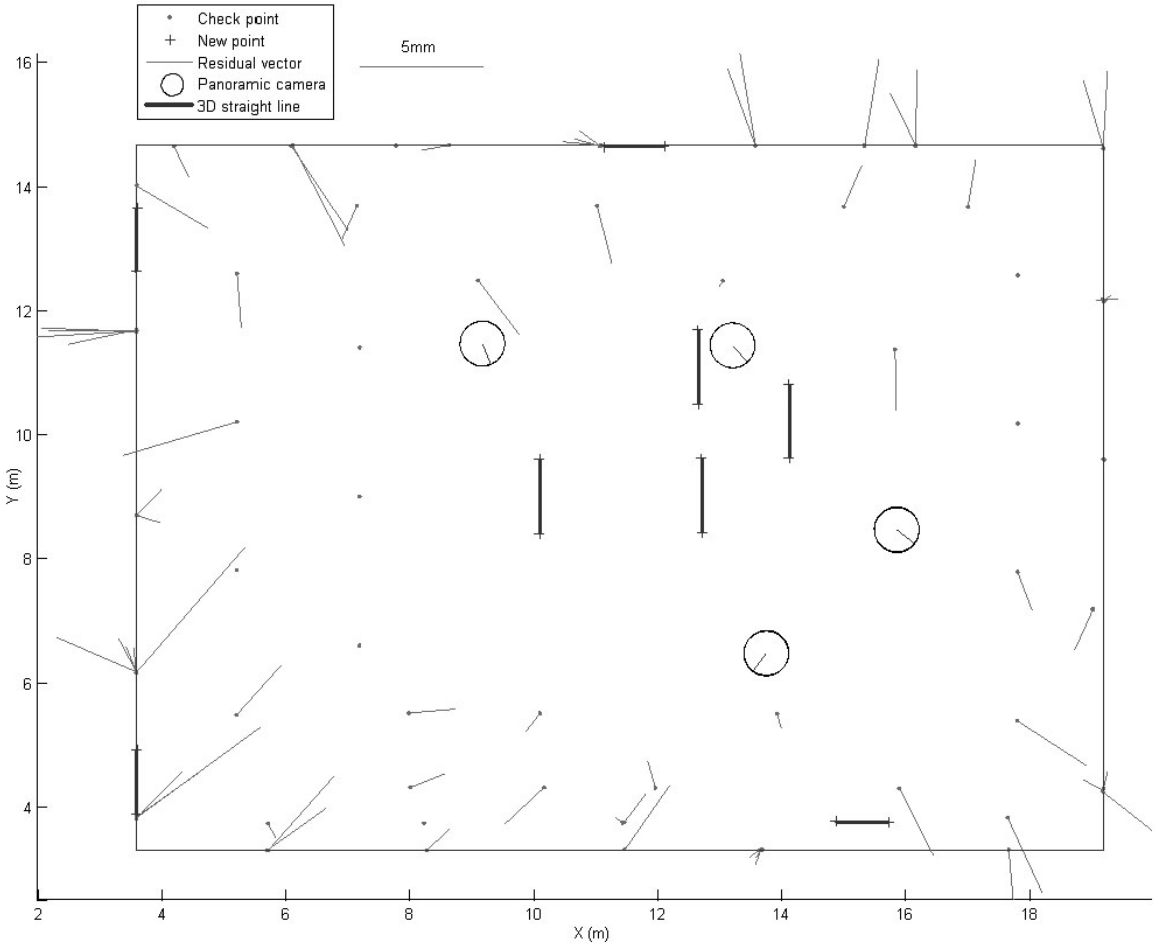

Figure 4.18. Residuals of check points in object space (fitting accuracy), while all additional parameters were estimated by bundle adjustment using 8 3D straight-line constraints and 87 tie points. Note the correction to the camera constant was fixed to a priori value determined from space resection.

The RMSEs of check point coordinates of self-calibration with comparison to the RMSEs from check points in Table 4.10 (in which the period of tumbling were known in advance and were fixed) shows that the estimation of additional parameters was successful.

5

Network Design and Analysis by Computer Heuristic Simulation

5.1 Introduction

The first step towards establishing a photogrammetric network is the design of the network. Conceptually, the purpose of the network design is to produce an optimum network configuration and an optimum observation plan that will satisfy the pre-set quality with the minimum effort. In other words, after the definition of the network quality requirements (precision and reliability) the technique of network optimization allows for finding such an optimal network configuration and an optimal set of observations that will satisfy these requirements (Grafarend, 1974; Cross, 1985; Schmitt, 1985; Schaffrin, 1985).

The importance of network design in close-range photogrammetry has been recognized since the 1970s and investigations into methods for close-range photogrammetric network design have been under development since then. An early solution to the problems associated with network design is presented by Marzan and Karara (1976). The network design methodology formulated is so called rational design. The method is based on a set of empirical formulae which output the expected precision of object space coordinates of points as functions of certain system or network parameters. Although such a network design method has the advantage of simplicity and economy, the concept has some problems for high precision close-range photogrammetric application. These include (Marshall, 1989):

- Lack of flexibility
- The solution is not mathematically rigorous
- The effect of both systematic and gross error cannot be assessed
- The influence of adjustment on the network cannot be assessed. For example datum definitions and effects of unstable imaging geometry
- Design is based on a specific set of system parameters while other, probably less significant system parameters are not included in the design process.

Due to these fundamental limitations in the rational design process, further development has not occurred and this procedure is not currently implemented in the design of close-range photogrammetric network.

An alternative, more flexible and mathematically rigorous, network design method was formulated by Grafarend (1974) primarily for the design of geodetic networks. It was very difficult, if not impossible, to solve all aspects of the network optimization in a single mathematical step. Instead, the design method as proposed by Grafarend, divides the design problem into sub-problems in order some progress could be made in each step. The basic orders of design classification, as proposed by Grafarend (1974) are:

- Zero-Order Design (ZOD): the datum problem
- First-Order Design (FOD): the configuration problem
- Second-Order Design (SOD): the observation weight problem
- Third-Order Design (TOD): the network densification problem

The above design orders can be done using two methods, namely, the trial-and-error method and the analytical method. In the trial-and-error method the optimum network can be sought manually (Cross, 1985). In contrast, the analytical method offers specific mathematical algorithms to solve a particular design problem. This method automatically produces a network that will be optimum in some mathematical sense.

Application of this design point of view has been applied successfully for close-range photogrammetry networks. Fraser (1984, 1992, 1996) discussed the network design problem in close-range photogrammetry. Fritsch and Crosilla (1990) performed first order design with an analytical method but results were not satisfactory. Mason (1994) used expert systems and Olague (2002) used a genetic algorithm for the placement of frame array CCD cameras using heuristic computer simulations. Saadatseresht et al. (2004) used the fuzzy inference system for the visibility analysis.

The concept of reliability of geodetic networks originates from Baarda (1967) and refers to the ability of a network to detect and resist blunders in observations (see Appendix D for more details). In close-range photogrammetry, precision and reliability considerations have been addressed by Gruen (1978, 1980) and Torlegard (1980).

In the case that self-calibration parameters are present, the network is designed to reduce the negative influence of the additional parameters on the network quality requirements, which are usually precision and reliability values of the object point coordinates. The influence of the additional parameters is studied in two ways:

- The effect of individual additional parameters on object point coordinates precision
- The dependence of one additional parameter on other parameters in the solution vector which can be shown by correlation analysis

The first case was already addressed in Gruen (1980) and Gruen and Beyer (2001). It can be extended for every sensor. The second case was studied for frame array CCD cameras by Fraser (1984) and Gruen and Beyer (2001). As a general rule for recovering the interior orientation additional parameters (shift of principal points) in self-calibration, an orthogonal kappa rotation between each camera station was suggested by Fraser (1984).

Due to the different characteristics of panoramic cameras compared to frame array CCD cameras, new considerations should be taken into account with respect to the following subjects of investigation:

- The network of panoramic cameras for reliability and precision enhancement
- Self-calibrating networks of panoramic cameras

The influence of the network for precision enhancement was studied by Amiri Parian and Gruen (2005c). Amiri Parian and Gruen (2006) discussed self-calibration networks of panoramic cameras by several examples. In section 5.2 the assumptions for the simulation are described. These are sensor parameters, additional parameters and workspace of the simulation. In section 5.3, different networks of panoramic cameras and a joint network of panoramic and frame array CCD cameras are analyzed for reliability and precision enhancement. In section 5.4, networks of panoramic cameras are analyzed for self-calibration and point positioning.

5.2 The Assumptions for the Simulation

The assumptions for the simulation are related to the sensor characteristics, monitoring objects (points) and additional parameters of the sensor, which will be given in the following sections.

5.2.1 Sensor Parameters

The simulated panoramic camera parameters are approximately equal to the parameters of the real panoramic camera, *SpheroCam*. A rectilinear lens with a focal length of 50 mm is used. The radius of the cylinder, the distance of the linear array from the rotation axis, is 100 mm. The eccentricity of the projection center is 50 mm (Table 5.1).

Table 5.1. Specification of the panoramic camera used in the simulations.

Focal length	50 mm
Image format (row, column) (pixel)	5,300 x 39,269
Eccentricity of the projection center	50 mm
Pixel size	8 microns

Network simulations for self-calibration modifies the synthetic true pixel coordinates by introducing random errors with a normal distribution N(0, σ; σ = 0.25 pixel).

5.2.2 Additional Parameters of the Sensor

The additional parameters of the panoramic camera that were used are:

- The eccentricities of the projection center from the origin of the turntable coordinate system: *ex, ey*

- The tilt and inclination of the linear array with respect to the turntable coordinate axis: *ly* and *lx*
- Lens distortions: k_1 and k_2
- The shift of principal point: dy_0
- The shift of the camera constant: *dc*
- The affinity by the correction of the angular pixel size: dp_x

These additional parameters are treated as block-invariant additional parameters and are used only for the self-calibration networks of panoramic cameras.

5.2.3 Workspace of Simulation

The dimension of the simulated workspace was 15 x 12 x 3 meters (Figure 5.1), which was similar to the panoramic testfield ETH Zurich (see 4.2.1). It consisted of 81 monitoring points.

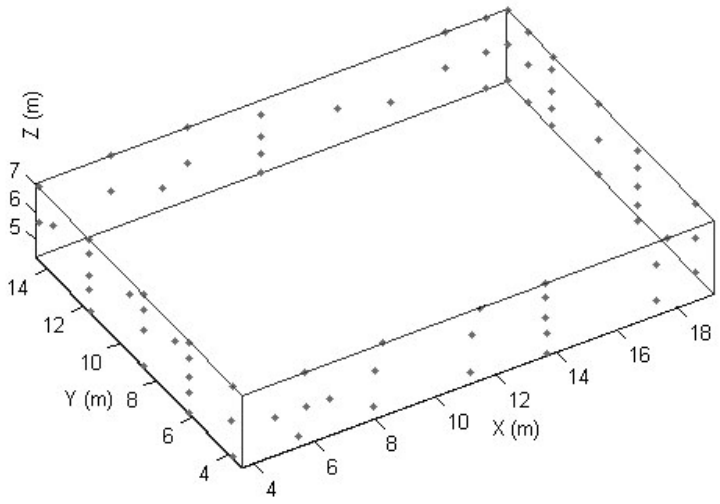

Figure 5.1. The workspace of the simulation with 81 monitoring points.

5.3 Enhancing the Precision and Reliability

Four networks of panoramic cameras and one joint network of panoramic and frame array CCD cameras are analyzed by heuristic simulation.

The mean internal accuracy of the panoramic camera system is assumed to be 0.25 pixel. This is based on the practical results of the camera self-calibration for a metric panoramic camera (Schneider and Maas, 2004). The mean internal accuracy of the frame array camera is assumed to be 0.1 pixel.

Simulations are performed, based on Equation (3.31), by considering the eccentricity of the projection center from the rotation axis. The bundle adjustment is based on free network adjustment (inner constraints datum considering all object points) for all cases.

5.3.1 Case 1: 2 Panoramic Camera Stations

The first network consists of two panoramic camera stations. The cameras are mounted on top of each other. The base line is vertical and its length is 1.5 meters. Figure 5.2 shows the top view of the absolute error ellipsoids of the object points. The mean value of the estimated standard deviation of object points' coordinates is 2.6 mm. Depth and lateral standard deviations are 2.56 and 0.38 mm (see Table 5.2).

The mean measure of the internal reliability is (0.36, 6.26) pixel for column and row coordinates of image point observations, respectively. These values show that this network is not able to detect blunders smaller than these values. In addition, because of the network geometry, the mean measure of the internal reliability for row coordinate (along linear array) is 17 times larger than the mean measure of the internal reliability for column coordinate (along rotation of the turntable). The influence of undetectable blunders, maximal measure of the external reliability, on the estimation of the object point coordinates is (75.43, 15.77) mm for depth and lateral coordinates, respectively (see Table 5.2).

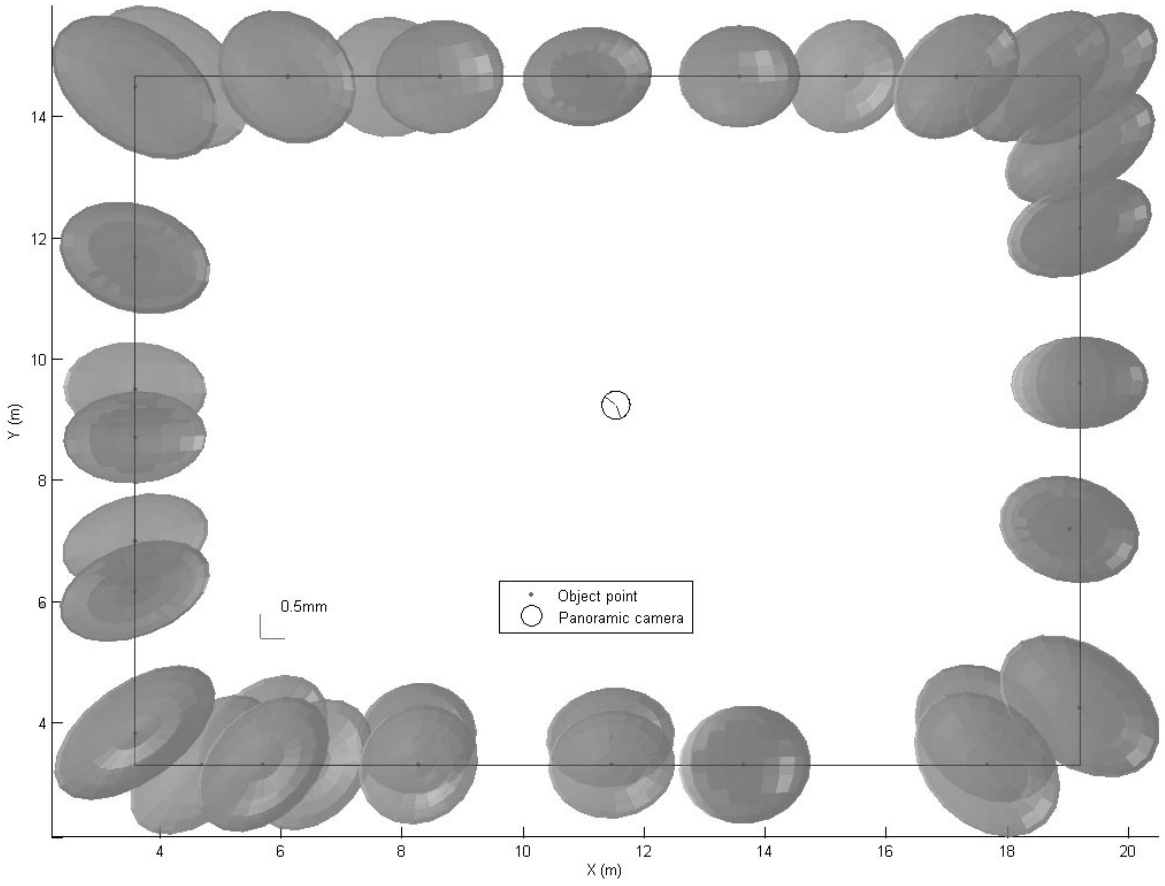

Figure 5.2. Absolute error ellipsoids from the network of 2 panoramic camera stations (case 1).

5.3.2 Case 2: 4 Panoramic Camera Stations

The second network consists of 4 panoramic camera stations. The base lines are horizontal and the base length is 7 meters along the X-axis and 6 meters along the Y-axis. The camera

stations are at the height of 1.5 meters from the workspace floor. Figure 5.3 shows the configuration of the panoramic camera stations and also the absolute error ellipsoids. In this network, the mean of the estimated standard deviation of object points' coordinates is 0.48 mm. Depth and lateral standard deviations are 0.46 and 0.15 mm (Table 5.2). The standard deviations of object points in this network have been enhanced with respect to the previous network. This is mainly because of the increase of the image scale.

This network shows also an improvement in the measures of the internal and external reliabilities compared to the previous network. The mean measure of the internal reliability is (0.45, 0.31) pixel for column and row coordinates of image point observations, respectively. The ability of this network geometry for blunder detection at row coordinate is higher than its ability at column coordinate with a factor of 1.5. The maximal measure of the external reliability is (1.61, 0.24) mm for depth and lateral coordinates of the object point coordinates, respectively (Table 5.2). These values are greater than the estimated standard deviations along depth and lateral axes of the object points with a factor of 3.5 and 1.5, respectively. If blunders present in the observations, the standard deviations of the depth and lateral axes of the object point coordinates are degraded maximum with these factors.

The coordinates estimated using this network are more reliable than the previous network.

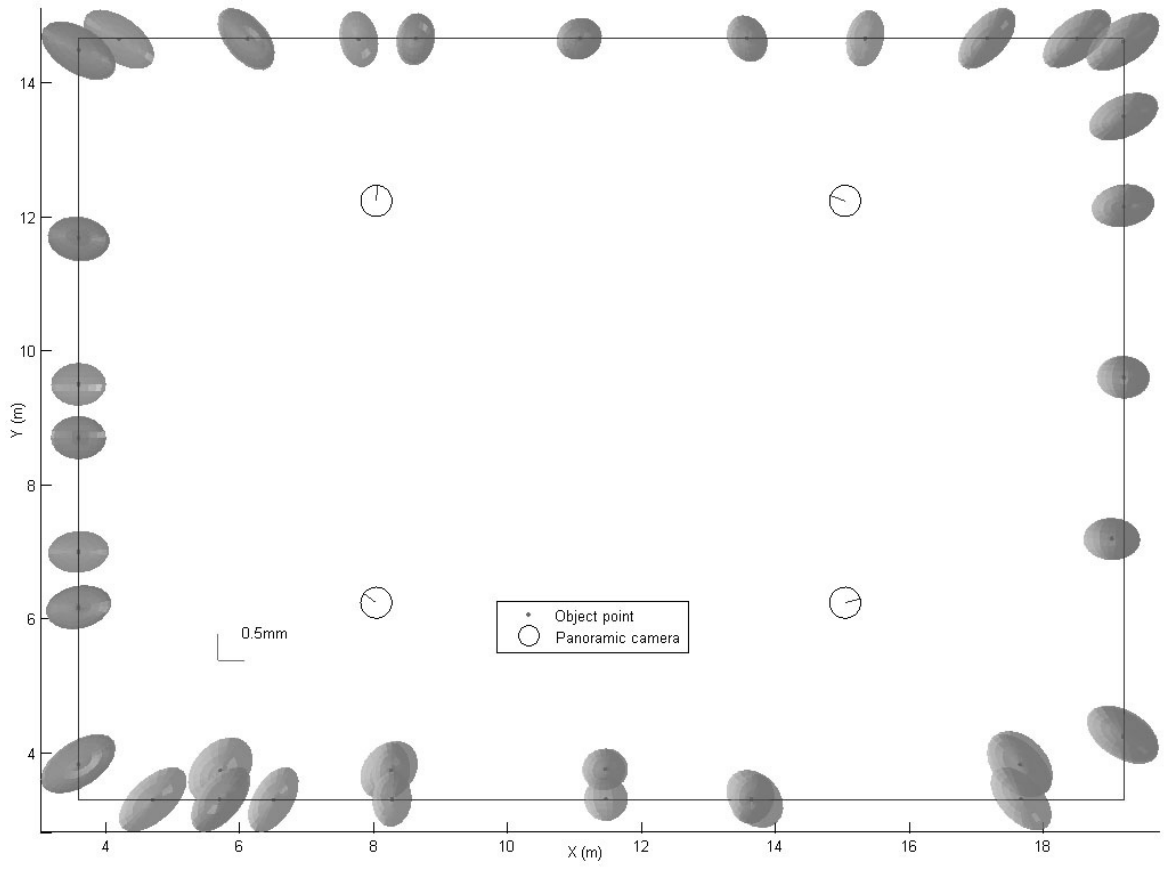

Figure 5.3. Absolute error ellipsoids from the network of 4 panoramic camera stations (case 2).

5.3.3 Case 3: 8 Panoramic Camera Stations

The third network consists of 8 panoramic camera stations. Four camera stations positioned on the same level and at the top of each station another station. The horizontal base length is 7 meters along X-axis and 6 meters along Y-axis. The vertical base is 1.3 meters. The mean estimated standard deviation is 0.29 mm for object points' coordinates, which is better than the previous cases. Lateral and depth standard deviations are 0.27 and 0.10 mm respectively. An improvement by factor of 1.8 was made in the difference of maximal and minimal standard deviations ($\Delta\sigma$). With respect to the previous network (case 2), standard deviations are enhanced in this case, because of the better configuration of the camera stations. However, at the corners, error ellipsoids differ from those at the middle of each side (Figure 5.4). The inhomogeneity of error ellipsoids is due to the small intersection angle of rays. The reason of larger error ellipsoids is smaller image point scale. To resolve this problem, FOD should be applied.

The mean measure of the internal reliability of this network is (0.31, 0.28) pixel for column and row coordinates of the image point observations, respectively. The maximal measure of the external reliability is (0.37, 0.12) mm for depth and lateral coordinates of the object point coordinates, respectively (Table 5.2).

The weak geometrical imaging can be solved by adding more camera stations and providing a stronger geometrical network configuration. One solution to this problem is strengthening the panoramic camera network by defining sub-networks of frame array CCD cameras for those points which have weaker geometry. The possibility of combined frame array and panoramic cameras has been already addressed in Schneider and Maas (2005).

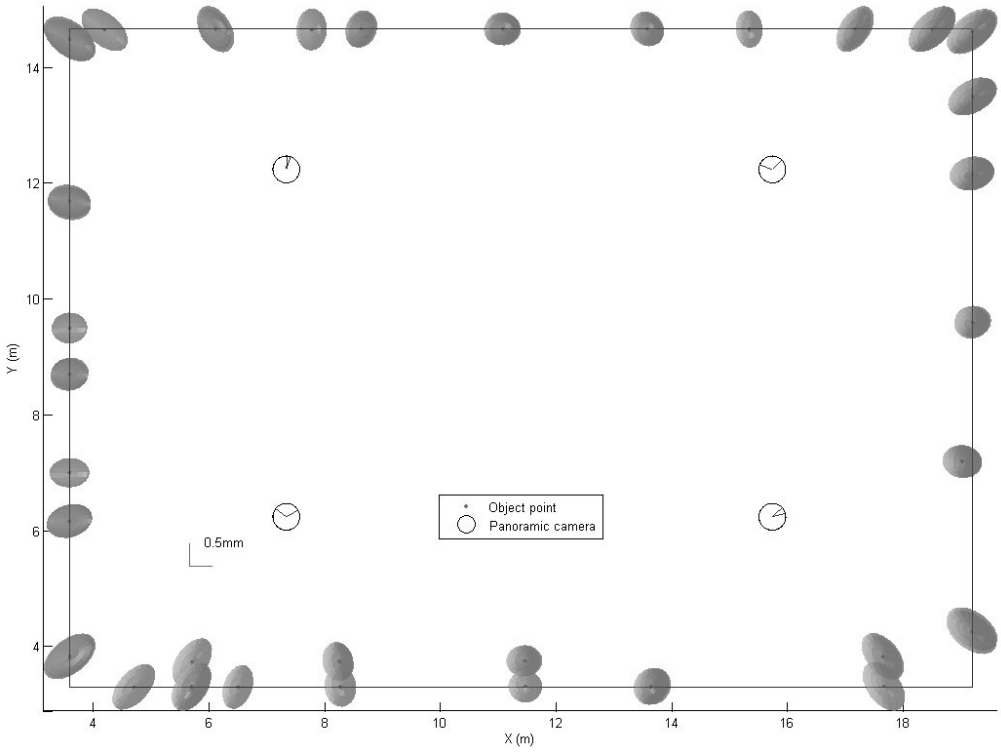

Figure 5.4. Absolute error ellipsoids from the network of 8 panoramic camera stations (case 3).

Table 5.2. The influence of the network configuration on the standard deviations of object point coordinates and internal and external reliabilities. The units of standard deviations are mm. The *a priori* and *a posteriori* standard deviation of unit weight is 0.25 for image point observation in pixel.

Network configuration	Relative precision	Mean σ	Mean σ depth	Mean σ lateral	Δσ depth	Δσ lateral	Mean measure of internal reliability (column, row) (pixel)	Max. measure of external reliability (depth, lateral) (mm)
2 pano. stns.	1 : 7,500	2.60	2.56	0.38	2.33	0.54	0.36, 6.26	75.43, 15.77
4 pano. stns.	1 : 40,500	0.48	0.46	0.15	0.57	0.13	0.45, 0.31	1.61, 0.24
8 pano. stns.	1 : 67,000	0.29	0.27	0.10	0.32	0.07	0.31, 0.28	0.37, 0.12
8 pano. stns. + 12 frame array stns.	1 : 97,000	0.20	0.18	0.07	0.18	0.06	0.28, 0.27	0.35, 0.12
16 pano. stns.	1 : 108,000	0.18	0.17	0.07	0.18	0.05	0.27, 0.27	0.18, 0.08

Δσ is the difference between the maximal and minimal standard deviations.
Note that for reliability computations the lower bound of the noncentrality parameter (δ_0) is set to 1 (see Appendix D).

5.3.4 Case 4: 8 Panoramic and 12 Frame Array CCD Cameras

The simulation continues by adding frame array camera stations to the previous network with the characteristics of a *Sony DSC-F828*. The focal length is 7.3 mm, the format size is 3264 x 2448 pixels and pixel size is 2.7 microns.

The sub-networks are used to improve the precision of those points which have worse precision than the other points (at the corner of the workspace). Because of the different distribution of the object points at the corners, two sub-networks are considered with two camera stations and two sub-networks are considered with four camera stations. In total, four sub-networks with 12 frame array stations are defined. The results of simulations are in Figure 5.5 and Table 5.2. The comparison of the standard deviation of this network with respect to the previous network shows an improvement of a factor 1.45. In addition, this network has a better degree of isotropy with respect to the previous networks.

The mean measure of the internal reliability of this network is (0.28, 0.27) pixel for column and row coordinates of the image point coordinates. The maximal measure of the external reliability is (0.35, 0.15) mm for depth and lateral coordinates of the object point coordinates (Table 5.2). The measures of the internal and external reliabilities are approximately similar to the measures of the internal and external reliabilities of the previous network.

The relative precision from this network is 1:97,200. However, considering the unwrapped 360˚ environment into a plane, the relative precision becomes 1:270,000.

5.3.5 Case 5: 16 Panoramic Camera Stations

Another network is considered which consists of 16 panoramic camera stations. 8 stations are at the same height and on top of each one, another panoramic camera station (Figure 5.6). The mean standard deviation of object points' coordinates is almost the same as in the previous network and is equal to 0.18 mm (Table 5.2).

The mean measure of the internal reliability of this network is (0.27, 0.27) pixel for column and row coordinates of the image point observations, respectively. These values are close to the *a posteriori* standard deviation (0.25) of the unit weight image point observations in pixel. The influence of undetectable blunders at this network (maximal measure of the external reliability) is (0.18, 0.08) mm for depth and lateral coordinates of the object points (Table 5.2).

The geometrical strength of the network of 8 extra panoramic camera stations in terms of precision of point coordinates is the same as the joint network of frame array and panoramic cameras. However, the error ellipsoids of the previous network are a little more isotropic at the corners of the workspace. In addition, this network is more reliable in terms of external reliability compared to the network of joint frame array and panoramic cameras. It shows the strength of this network for reducing the influence of undetectable blunders.

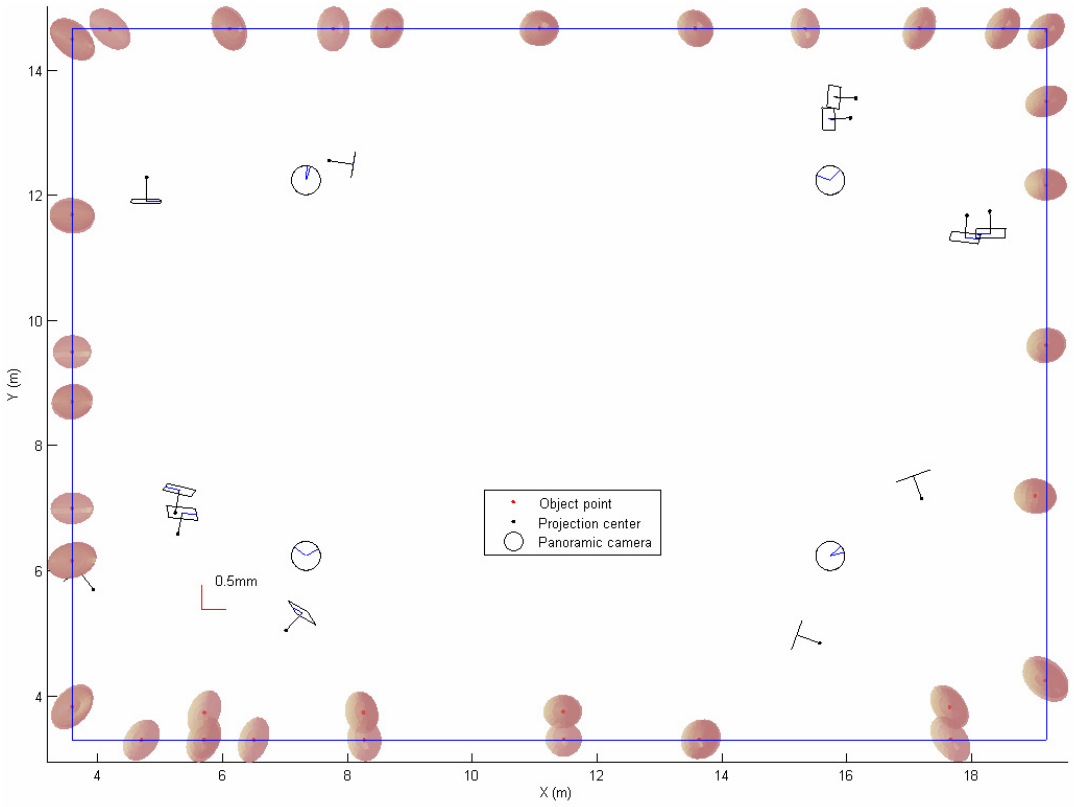

(a)

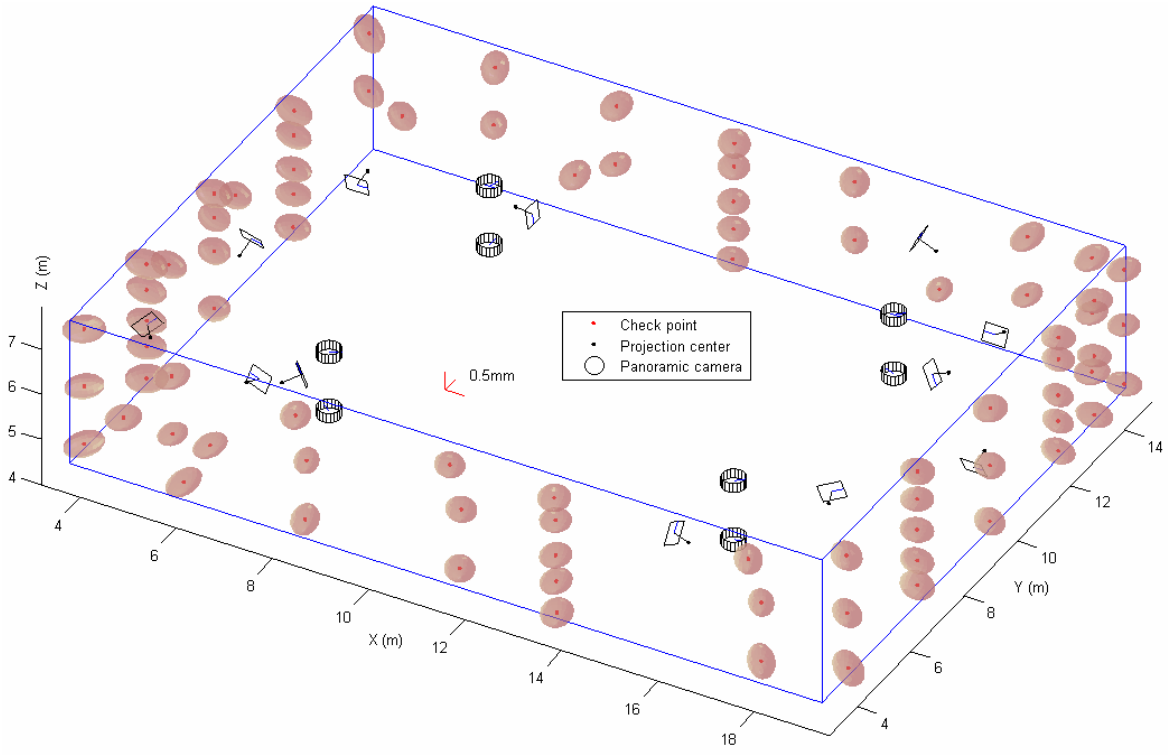

(b)

Figure 5.5. Absolute error ellipsoids from the network of panoramic and frame array CCD cameras with 8 panoramic camera stations and 12 frame array CCD camera stations (case 4). a) XY-view and b) oblique view.

Taking 12 images with frame array camera needs much less time than taking 8 images with a panoramic camera. In addition, due to the mechanical design of the panoramic camera, the convergent concept is not realized in direction along the linear array axis. This lack of flexibility in geometrical design of the panoramic camera network can be resolved with frame array cameras.

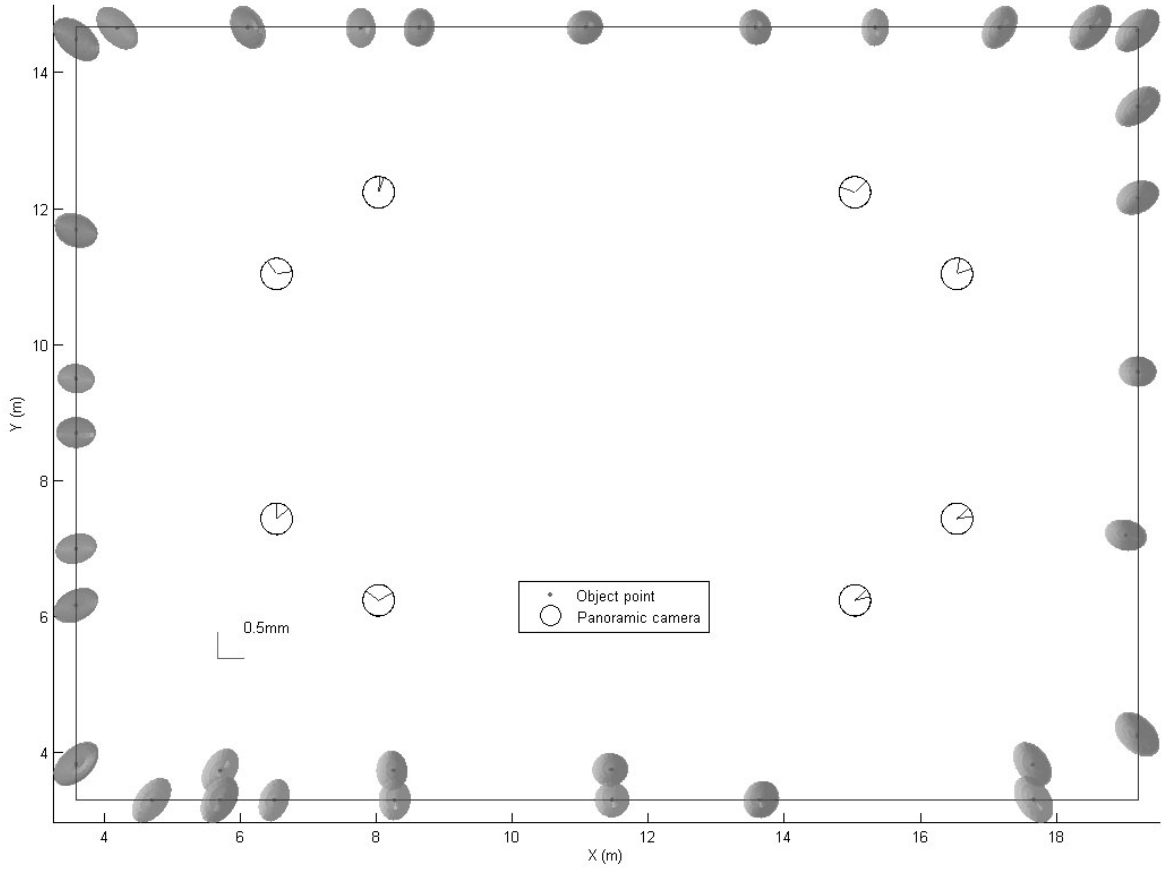

Figure 5.6. Absolute error ellipsoids from the network of 16 panoramic camera stations (case 5).

5.4 Point Positioning and Self-Calibration

Because of the design structure of panoramic cameras, the camera stations are leveled in practice. In addition, a full panoramic visibility of the surroundings requires nearly leveled camera station. However, problems can arise in self-calibrating networks.

The aim of this section is to find a suitable configuration of panoramic camera stations for the purpose of self-calibration. This will be determined by the aid of the correlation analyses of unknowns and accuracy tests.

Six different network cases are studied by heuristic simulation. In all cases, the datum choice is inner constraints (free network) based on all control points. All control points are also used as check points for the accuracy tests. In four network cases (cases 4-6), non-leveled camera stations have been introduced, with omega (rotation around X-axis) and phi

(rotation around Y-axis) set to non-zero values in order to de-correlate additional parameters with object point coordinates and exterior orientation parameters.

5.4.1 Case 1: 2 Stations

The first network consists of 2 stations. The stations have a vertical base of 1.5 meters with a zero horizontal base. Both stations are leveled (omega and phi are 0). This is the simplest configuration which could be established for the measurement of a 360° environment.

Self-calibration with all additional parameters is not possible in such a network due to very high correlations between additional parameters, Exterior Orientation Parameters (EOPs) and the coordinates of the object points. Increasing the vertical and horizontal bases does not solve the problem.

5.4.2 Case 2: 4 Leveled Stations at the Same Height

In order to improve the network geometry, a new network with 4 camera stations is considered (Figure 5.7). The geometry of this network is better than the network of two stations in case 1 (see section 5.3).

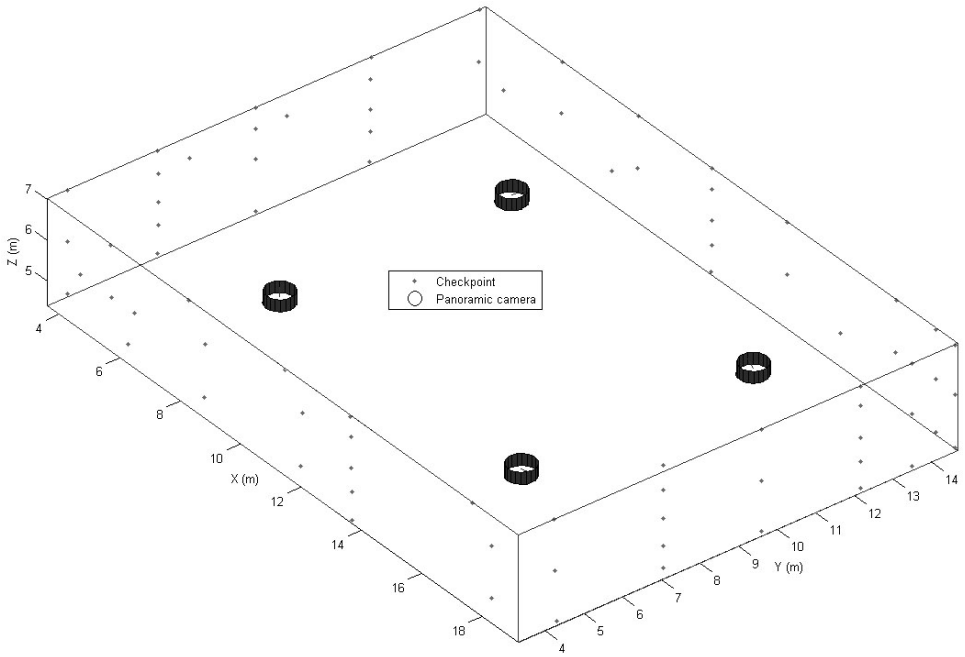

Figure 5.7. The configuration of four panoramic camera stations network.

After performing simulation and self-calibration, very high correlations (almost close to 1) are observed between (Table 5.3):

- *dc,* k_1 and k_2 and object point coordinates
- EOPs and object point coordinates
- additional parameters (*dc*, dp_x, k_1 and k_2) and EOPs

The mean standard deviations of this network, which are 0.5 mm in depth and 5.4 mm in lateral axes, is much better than the RMSEs from check points, which turned out to be 76.5 mm for depth and 930.2 mm for lateral axes. From this type of network configuration (see section 5.3) we expect better lateral precision and RMSE than depth precision and RMSE. The reason of such degradation is the high correlation of object point coordinates with EOPs and additional parameters. This degradation is not only seen in the estimation of the object point coordinates but also influences the estimation of those additional parameters which have very high correlations with other parameters. In this example, *dc,* k_1 and k_2 could not be estimated and are far from the true value of the simulation.

5.4.3 Case 3: 4 Leveled Stations at Different Heights

Case 3 investigates the influence of different heights of stations. The results are similar to the results of case 2. High correlations still exist and the determination of the object point coordinates is not accurately possible (Table 5.3). The additional parameters that have high correlations with object point coordinates cannot be determined. The height difference of stations in this network did not de-correlate parameters.

5.4.4 Case 4: 4 Unleveled Stations at the Same Height (±3°)

In this network case, the influence of a convergent network is investigated. The network convergence of panoramic cameras along the rotation axis (vertical axis) is weak and usually cannot be realized because of the design structure of the turntable which optimally and with less mechanical errors operates at leveled situations.

The network in this case consists of 4 camera stations. The stations are not leveled and omega and phi are ±3°. After the self-calibration of this network, high correlations (Table 5.3) appear between:

- *dc* and Z-coordinates, only for some of the object point coordinates
- EOPs and Z-coordinates of the object points
- Additional parameters and some EOPs

The mean standard deviations of check points from this network are 0.4 mm for depth and 1.2 mm for the lateral axes. The RMSEs of check point coordinates are 0.4 mm for depth and 2 mm for lateral coordinates. Figure 5.8 shows the depth axes view and lateral axis view of the check point coordinates residuals in object space. From this Figure it is clear that the high correlation of *dc* and Z-coordinate of the object points has degraded the estimation of the Z-coordinates. Therefore, depth standard deviation is better than lateral standard deviation which is unusual for this kind of geometrical network.

Comparing the result of this network to the network of case 2, a significant improvement is obvious. Although it is not an ideal network for self-calibration, it shows the influence of convergence along the vertical axis for panoramic cameras.

5.4.5 Case 5: 4 Unleveled Stations (±9°)

The network of this case is similar to the previous network (case 4) with the difference that the stations are not leveled and omega and phi are equal to ±9°, which means more convergence along the vertical axis. The comparison of the results of this network with the network case 4 shows a substantial improvement (Table 5.3) of de-correlations of parameters and object point coordinates.

Networks of different station heights of this version were also simulated. The results (Table 5.3) are similar to the case were camera stations are at the same height. This indicates that the height difference does not have an influence regarding our purpose of de-correlation of the parameters.

5.4.6 Case 6: 4 Unleveled Stations at the Same Height (±14°)

In continuation of the evaluation of convergent panoramic camera networks, a network of 4 stations at the same height with omega and phi equal to ±14° (more convergence with respect to the previous networks) was simulated. The result of the simulation (Table 5.3) no longer shows high correlations of parameters. In addition, the mean standard deviation of the object point coordinates and RMSEs from check points are in good agreement with each other. The lateral precision is better than the depth precision which is expected from this network configuration.

In this network configuration highly correlating additional parameters are:

- dy_0, ly with correlation of 0.98
- k_1, k_2 with correlation of 0.96

Both sets of parameters: k_1, k_2 and dy_0, ly have inherent correlations. All the parameters of this network turned out to be significant after testing. In addition, the estimated additional parameters are in good agreement with the true additional parameters of the simulation.

We achieve a better determination of additional parameters by tilting the camera. It was shown that a tilt of around 10° gives already stable results in all additional parameters and the determination of object space coordinates. A strong self-calibrating network, for both object point positioning and additional parameters determination can be realized with tilted camera stations.

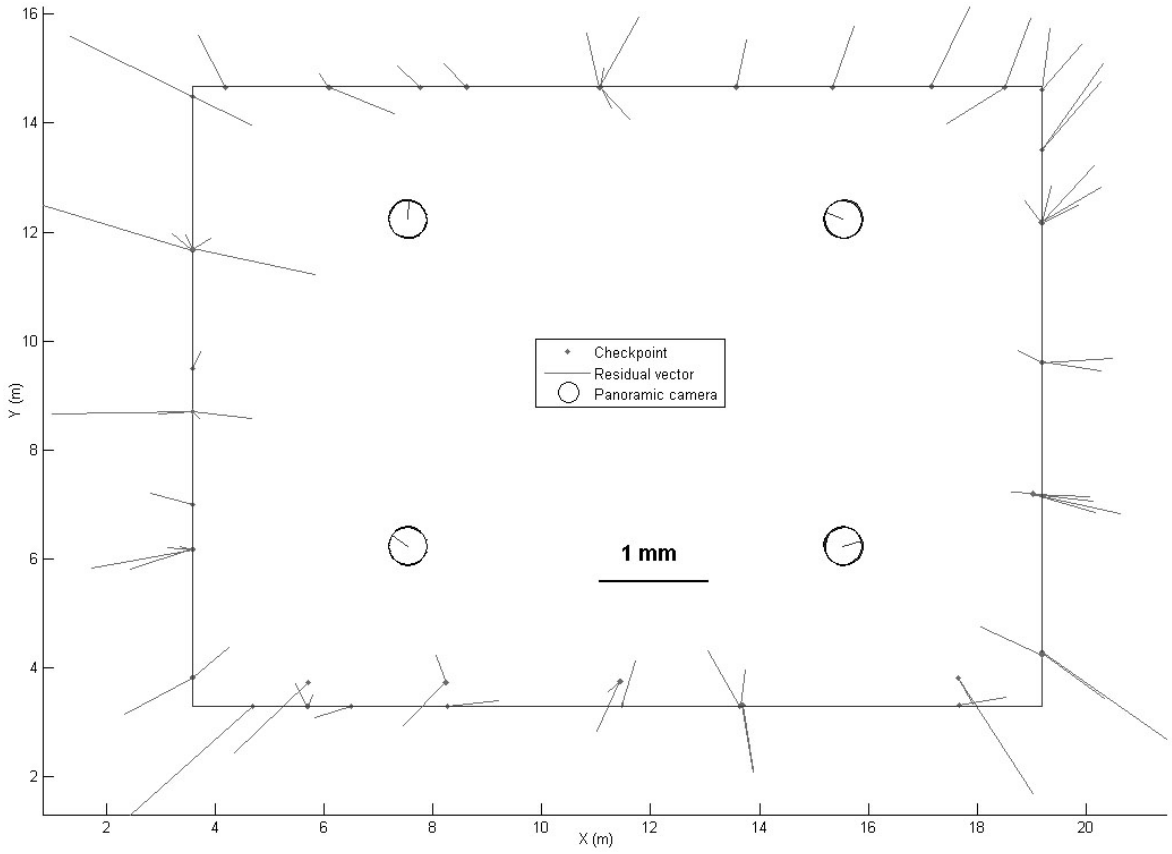

(a)

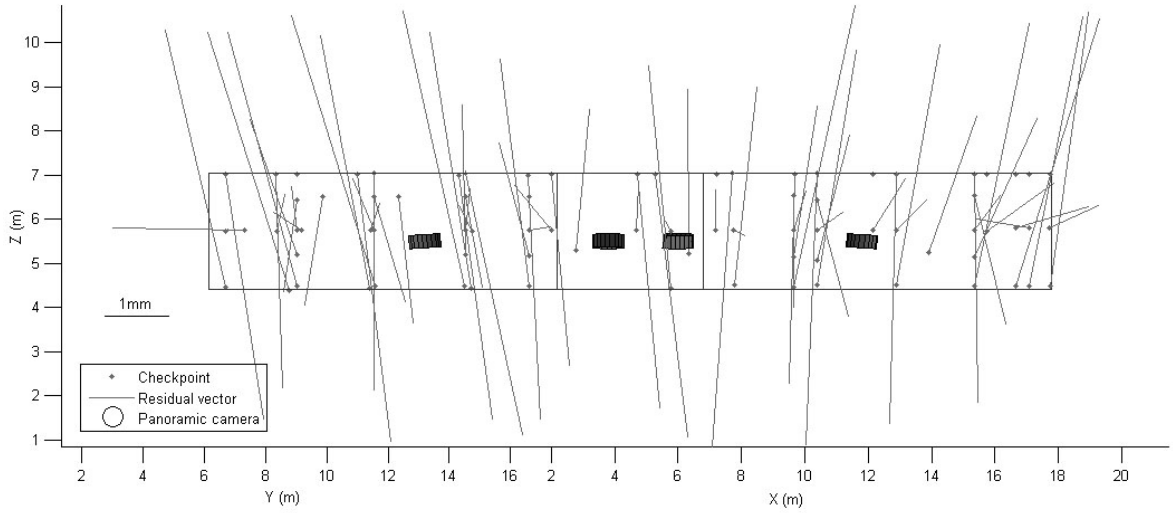

(b)

Figure 5.8. The residuals from check points in object space for the case 4. a) The visualization of the depth axes residuals and b) the visualization of the lateral axis residuals.

Table 5.3. Results summary of the simulated networks (units are mm. RMSEs and standard deviations are from check points). For the estimation of the standard deviations, sigma naught cap of each version was used (approximately 0.2).

#	Network configuration (4 stations)	[1] High correlations	RMSE of X,Y,Z	[2] Std. X,Y,Z
2	omega and phi are 0 stations are at the same height	*dc*, k_1 , k_2 … all (X,Y,Z) (>0.95) EOPs ... all (X,Y,Z) (>0.95) additional parameters…EOPs (>0.95)	89.5, 63.5, 930.2	0.6, 0.5, 5.4
3	omega and phi are 0 stations are at different heights	*dc*, dy_0 , k_1, k_2 … all (X,Y,Z) (>0.95) *ly* … all (X,Y,Z) (>0.85, >0.85, >0.90) EOPs ... all (X,Y,Z) (>0.95) additional parameters … EOPs (>0.95)	89.5, 63.5, 929.6	0.6, 0.4, 4.8
4	omega and phi are ±3° stations are at the same height	*dc* … Z-coordinates (>0.95 for 67 points) EOPs … Z-coordinates (>0.95) additional parameters … some EOPs (>0.95)	0.5, 0.4, 2.0	0.4, 0.3, 1.2
5	omega and phi are ±9° stations are at the same height	*dc* … Z-coordinates (>0.75 and <0.85 for 29 points) EOPs … Z-coordinates (>0.80 and <0.95 for 15 points) additional parameters … some EOPs (>0.75 and <0.95)	0.3, 0.3, 0.2	0.3, 0.3, 0.3
	omega and phi are ±9° stations are at different heights	*dc* … Z-coordinates (>0.75 and <0.85 for 34 points) EOPs … Z-coordinates (>0.80 and <0.95 for 24 points) additional parameters … some EOPs (>0.75 and <0.95)	0.3, 0.3, 0.3	0.3, 0.3, 0.3
6	omega, phi are ±14° stations are at the same height		0.3, 0.3, 0.2	0.3, 0.3, 0.2

[1] High correlation is for additional parameters with EOPs, additional parameters with XYZ object points and EOPs with XYZ object points
[2] Mean standard deviation

6

Datum-Invariant Parameters

6.1 Introduction

The datum of a photogrammetric network is defined as basic (minimal) parameters needed to define the network in space. One scale, three orientations and three coordinates are needed to position the network relative to a pre-defined coordinate system. The conventional photogrammetric measurements, e.g., image features (point and line) are internal measurements made in the image space. Therefore, they can only define relative positions (i.e. relative coordinates) of the network points, while the absolute coordinates of a network point are external quantities. Thus, with the conventional measurements alone, position computations cannot be initiated unless some other basic information, i.e., the network datum, is defined.

Mathematically, the need for the datum parameters of a network means that, in addition to having at least as many observations as unknowns, a network must be supplied with the above minimal information in order to proceed computations. As a minimum, a 3D photogrammetric network must have one scale, three orientations, and one known position (three coordinates) for resolving seven datum defects. The various approaches for defining network datum parameters are as follows (Pope, 1971; Vanicek and Krakiwsky, 1986):

- over-constrained
- minimal constraints
- inner constraints (free network adjustment)

An example of an over-constrained network is a photogrammetric network with more than three control points (actually two full control points and one of the coordinates of the third control point). In the case of a strong geometrical network, the datum definition is not over-constrained for two reasons. The first is the cost of control point observations (external observations). The second reason is the influence of over-constrained datums on the additional parameters of the sensor (frame array CCD or panoramic cameras) in the case of self-calibration.

These problems are solved using minimal and inner constraints datums. An inner constraints datum is a specific type of minimal constraints datum with the property that among all minimal constraints datum, the trace of the cofactor matrix of unknowns is

minimal (Bossler et al., 1973). In addition, the solution from inner constraints datum has the minimum norm of unknowns with respect to other minimal constraints datum (Lawson and Hanson, 1974).

In this chapter, the influence of the datum definition on the solution vector (all unknown parameters) and the quality analysis matrices (computed from least squares adjustment) are shown with an analytical proof. Numerical examples are also given.

6.2 Least Squares and Quality Analysis Matrices

In order to simplify the mathematical formulation for both frame array and panoramic cameras, the observation equations of the collinearity equations are written with general terms in the form of equation (6.1).

$$\begin{cases} v_x + x = f_x + g_x \\ v_y + y = f_y + g_y \end{cases} \tag{6.1}$$

where,

x, y…… image point observations,
v_x , v_y …….. residuals of image point observations (x, y),
f_x, f_y……... functions of exterior orientation parameters and object point coordinates,
g_x, g_y……. functions of additional parameters.

The functions g_x and g_y are linear for frame array cameras and non-linear for panoramic cameras.

Equation (6.2) shows the linear terms of the Taylor expansion of equation (6.1).

$$\begin{cases} x = f_x(X_0) + g_x(Y_0) + \dfrac{\partial f_x}{\partial X} \cdot \delta X + \dfrac{\partial g_x}{\partial Y} \cdot \delta Y \\ y = f_y(X_0) + g_y(Y_0) + \dfrac{\partial f_y}{\partial X} \cdot \delta X + \dfrac{\partial g_y}{\partial Y} \cdot \delta Y \end{cases} \tag{6.2}$$

where,

X …….. exterior orientation parameters and 3D coordinates of object points,
Y ……... additional parameters,
X_0 and Y_0 … initial values.

The observation equations of equation (6.1) are rewritten in the matrix form of equation (6.3):

$$V + dL = A \cdot \delta U \ , \ P = \sigma_0^2 \cdot C_L^{-1} \tag{6.3}$$

with

C_L ……. variance covariance matrix of observations.

where,

$$A = \begin{pmatrix} B & C \end{pmatrix}, \delta U = \begin{pmatrix} \delta X \\ \delta Y \end{pmatrix}, V = \begin{pmatrix} v_x \\ v_y \end{pmatrix}$$

$$dL = \begin{pmatrix} x - f_x(X_0) - g_x(Y_0) \\ y - f_y(X_0) - g_y(Y_0) \end{pmatrix}, B = \begin{pmatrix} \frac{\partial f_x}{\partial X} \\ \frac{\partial f_y}{\partial X} \end{pmatrix} \text{ and } C = \begin{pmatrix} \frac{\partial g_x}{\partial Y} \\ \frac{\partial g_y}{\partial Y} \end{pmatrix} \tag{6.4}$$

If the network has datum defect, the matrix A will be a rank deficient and singular matrix. In this case, a datum matrix D (Vanicek and Krakiwsky, 1986) is defined in order to make the matrix A full rank. In this case the least squares solution of the equation (6.4) will be in the form of equation (6.5).

$$\begin{pmatrix} \delta X \\ \delta Y \end{pmatrix} = \delta \hat{U} = Q_U \cdot (A^t \cdot P \cdot dL) = (N + D^t \cdot D)^{-1} (A^t \cdot P \cdot dL) \tag{6.5}$$

where,

$$Q_U = (N + D^t \cdot D)^{-1} - H^t \cdot (H \cdot D^t \cdot D \cdot H)^{-1} \cdot H \tag{6.6}$$

with

$$Q_U = \begin{pmatrix} Q_{XX} & Q_{XY} \\ Q_{YX} & Q_{YY} \end{pmatrix}$$

$N = A^t P A$

H ……. null space matrix of A

$A \cdot H^t = 0$, $N \cdot H^t = 0$, $H \cdot A^t = 0$ and $H \cdot N = 0$

The parameters and quality analysis matrices that can be derived from least squares are summarized in Table 6.1.

It has been known in geodesy and photogrammetry that the change of datum definition has no influence on some of the above parameters and quality analysis matrices. This will be shown with an analytical proof in section 6.3. In relation to photogrammetry, the author has not found the proof of datum-invariant additional parameters and cofactor matrix of additional parameters in the literature. These proofs are also given in sections 6.3.2 and 6.3.3.

Table 6.1. Summary of the parameters and quality analysis matrices from least squares optimization.

$\begin{pmatrix}\delta X\\ \delta Y\end{pmatrix} = \delta\hat{U} = Q_U \cdot (A^t \cdot P \cdot dL) = (N + D^t \cdot D)^{-1} \cdot (A^t \cdot P \cdot dL)$	unknown parameters
$Q_U = (N + D^t \cdot D)^{-1} - H^t \cdot (H \cdot D^t \cdot D \cdot H)^{-1} \cdot H$	cofactor matrix of unknowns
$Q_{\hat{l}} = A \cdot Q_U \cdot A^t = A \cdot (N + D^t \cdot D)^{-1} \cdot A^t$	cofactor matrix of adjusted observations
$Q_{\hat{V}} = P^{-1} - Q_{\hat{l}}$	cofactor matrix of residuals
$\hat{V} = A \cdot \delta\hat{U} - dL = Q_{\hat{V}} \cdot P \cdot dL$	residual vector of observations
$\hat{\sigma}_0^2 = \hat{V}^t \cdot P \cdot \hat{V} / d_f$	variance factor with $d_f = trace(Q_{\hat{V}} \cdot P)$

6.3 Datum-Invariant Parameters and Quality Analysis Matrices

Datum-invariant parameters are listed in the Table 6.2. It is obvious that the matrices A, P, N, H and vector dL are datum-invariant, because they are independent of the datum definition matrix D.

According to Table 6.1, $Q_{\hat{V}}$, $\hat{\sigma}_0^2$, $\hat{V}$ and R are computed based on $Q_{\hat{l}}$. Therefore, if we prove that $Q_{\hat{l}}$ is datum-invariant then these matrices are datum-invariant, too. The proof is given in section 6.3.1. In section 6.3.2 and 6.3.3 the proof of datum independency of δY and Q_{YY} will be shown.

Table 6.2. Datum independent parameters of the least squares optimization.

A ……	the design matrix
dL ……..	$dL = A \cdot \delta\hat{X} - \hat{V}$
$\hat{V}$ ……	the estimated residual vector
$Q_{\hat{l}}$ ……..	the cofactor matrix of the adjusted observations
P ……	the weight matrix of the observations
N ……	the normal matrix
H ……	the null space matrix of the design matrix
$Q_{\hat{V}}$ ……..	the cofactor matrix of the estimated residuals
$\hat{\sigma}_0^2$ ……..	the *a posteriori* variance factor
Q_Y ……..	the cofactor matrix of the additional parameters
δY ……..	the correction to the additional parameters

6.3.1 Cofactor Matrix of Observations

For two different datum choices with datum matrices D_1 and D_2 the following equation is written:

$$\begin{aligned} Q_{\hat{l},1} &= A \cdot Q_{U,1} \cdot A^t = A \cdot (I - H^t \cdot (D_2 \cdot H^t)^{-1} \cdot D_2) \cdot Q_{U,1} \cdot A^t \\ &= A \cdot (Q_{U,2} \cdot N) \cdot Q_{U,1} \cdot A^t = A \cdot Q_{U,2} \cdot (N \cdot Q_{U,1}) \cdot A^t \\ &= A \cdot Q_{U,2} \cdot (I - D_1^t \cdot (H \cdot D_1^t)^{-1} \cdot H) \cdot A^t = A \cdot Q_{U,2} \cdot A^t = Q_{\hat{l},2} \end{aligned} \tag{6.7}$$

which shows that the cofactor matrix of the adjusted observations from datum choice D_1 is equal to the cofactor matrix of the adjusted observations from datum choice D_2. However, we need to prove equation (6.8), which was already used in equation (6.7).

$$Q_U \cdot N = I - H^t \cdot (D \cdot H^t)^{-1} \cdot D \tag{6.8}$$

In the least squares optimization process, through derivation of the "variation function" (Vanicek and Krakiwsky, 1986), the equation (6.9) is constructed.

$$G \cdot \begin{pmatrix} \delta U \\ -K_2 \end{pmatrix} = \begin{pmatrix} -A^t \cdot P \cdot dL \\ 0 \end{pmatrix}$$

with (6.9)

$$G = \begin{pmatrix} N & D^t \\ D & 0 \end{pmatrix}$$

where K_2 is the "Lagrange correlate", reflecting the fact that datum constraints are present in the optimization. The solution to equation (6.9) is acquired by inversion of the matrix G. The inverse of matrix G is denoted in equation (6.10).

$$\begin{pmatrix} Q_U & S^t \\ S & T \end{pmatrix} = G^{-1} \tag{6.10}$$

From equation (6.10), equation (6.11) and the sets of equations of (6.12) are derived.

$$N \cdot Q_U + D^t \cdot S = I \tag{6.11}$$

$$\begin{aligned} N \cdot S^t + D^t \cdot T &= 0 \\ D \cdot Q_U &= 0 \\ D \cdot S^t &= I \end{aligned} \tag{6.12}$$

By pre-multiplication of H to equation (6.11), the equation (6.13) is obtained (note that H is null space matrix of N).

$$S = (H \cdot D^t)^{-1} \cdot H \tag{6.13}$$

Substituting equation (6.13) into the equation (6.11) gives the proof of the equation (6.8).

6.3.2 Additional Parameters

Equation (6.5) can be rewritten in matrix form (equation (6.14)):

$$\begin{pmatrix} B^t \cdot P \cdot B + D_X^t \cdot D_X & B^t \cdot P \cdot C \\ C^t \cdot P \cdot B & C^t \cdot P \cdot C \end{pmatrix} \cdot \begin{pmatrix} \delta X \\ \delta Y \end{pmatrix} = \begin{pmatrix} B^t \cdot P \cdot dL \\ C^t \cdot P \cdot dL \end{pmatrix} \tag{6.14}$$

Where, D_X is the datum matrix that is defined by exterior orientation parameters and 3D coordinates of object points. Equation (6.4) gives the definition for matrices B, and C and vector dL.

From the equations system of (6.14), δY is computed (equation (6.15)) as

$$\delta Y = (C^t \cdot P \cdot C - C^t \cdot P \cdot Q_{\hat{l},B} \cdot P \cdot C)^{-1} \cdot (C^t \cdot P \cdot dL - C^t \cdot P \cdot Q_{\hat{l},B}) \tag{6.15}$$

Where $Q_{\hat{l},B}$ is the cofactor matrix of the adjusted observations when additional parameters are not in the equation (6.2). Since $Q_{\hat{l},B}$ is datum-invariant and the other matrices in equation (6.14) are also datum-invariant, δY becomes a datum-invariant quantity.

6.3.3 Cofactor Matrix of Additional Parameters

Through decomposition of equation (6.6), equation (6.16) is derived:

$$\begin{pmatrix} Q_{XX} & Q_{XY} \\ Q_{YX} & Q_{YY} \end{pmatrix} = \begin{pmatrix} K_{11} & K_{12} \\ K_{21} & K_{22} \end{pmatrix} - \begin{pmatrix} H_X^t \cdot (H_X \cdot D_X^t \cdot D_X \cdot H_X)^{-1} \cdot H_X & 0 \\ 0 & 0 \end{pmatrix} \tag{6.16}$$

with

$$\begin{pmatrix} K_{11} & K_{12} \\ K_{21} & K_{22} \end{pmatrix} = \begin{pmatrix} B^t \cdot P \cdot B + D_X^t \cdot D_X & B^t \cdot P \cdot C \\ C^t \cdot P \cdot B & C^t \cdot P \cdot C \end{pmatrix}^{-1} \tag{6.17}$$

Q_{YY} is datum independent, if K_{22} in equation (6.17) is datum independent.

By the matrix partitioning (see appendix C) of equation (6.17), the solution of K_{22} is achieved by equation (6.18).

$$\begin{aligned} K_{22} &= (C^t \cdot P \cdot C - C^t \cdot P \cdot B \cdot (B^t \cdot P \cdot B + D_X^t \cdot D_X)^{-1} \cdot B^t \cdot P \cdot C)^{-1} \\ &= (C^t \cdot P \cdot C - C^t \cdot P \cdot Q_{\hat{l},B} \cdot P \cdot C)^{-1} \end{aligned} \tag{6.18}$$

Since $Q_{\hat{l},B}$ and other matrices in equation (6.18) are datum-invariant quantities, K_{22} is also a datum-invariant matrix. Therefore Q_{YY} is a datum-invariant matrix.

6.4 Numerical Results

Numerical examples are given for a simulated network of a panoramic camera. The assumptions of the simulation are the same as those that were given in section 5.2. However, to highlight the influence of imprecise control point coordinates on the estimation of the additional parameters, the control point coordinates are degraded by a normal distribution noise with mean value of 0 and standard deviation of 5 mm.

The network configuration is the same as the network configuration which was already shown in section 5.4.6. The important property of this network geometry is that it reliably estimates the additional parameters and object point coordinates.

Four different datum choices are considered for this investigation:

1) Inner constraints datum by using all object points (datum #1),
2) Two different minimal constraints datums, with different distribution of 7 coordinates of control points (datum #2 and #3),
3) Over-constrained datum by using all control points (datum #4).

Table 6.3 shows the true values of the estimated additional parameters from each datum choice. Among the additional parameters, *ey* was not a significant parameter after significance testing of parameters.

Table 6.3. True values of additional parameters, estimated values and standard deviations of additional parameters for 4 different datum choices.

			Datum #1, #2, #3		Datum #4	
		True values	Estimated values	Standard deviations	Estimated values	Standard deviations
Additional parameters	dp_x (mm)	5e-7	5.00e-7	9.00e-10	5.00e-7	7.10e-9
	dy_0 (mm)	0.55	0.56	1.15e-2	0.78	1.06e-1
	dc (mm)	1.5	1.50	8.84e-3	1.46	8.36e-2
	k_1 (mm^{-2})	1e-4	1.00e-4	5.73e-7	1.21e-4	9.38e-6
	k_2 (mm^{-4})	-3e-7	-3.00e-7	1.00e-9	-3.47e-7	1.77e-8
	ex (mm)	-50	-51.081	0.748	-53.26	4.97
	ey (mm)	1e-1	0.17	0.22	0.57	1.35
	lx (rad)	1e-2	9.94e-3	5.66e-5	9.35e-3	3.80e-4
	ly (rad)	1e-2	9.79e-3	2.07e-4	5.56e-3	2.05e-3

From Table 6.3 it is clear that the estimated additional parameters and their standard deviations for datum choices of inner and minimal constraints are the same. However, the additional parameters and their standard deviations differ from those for over-constrained

datum. The additional parameters from the first three datums are closer to the true values with respect to the results from datum #4.

The above example shows the influence of datum choice on the estimation of additional parameters. Imprecise control point coordinates degrade the estimation of the additional parameters in the case of an over-constrained datum.

The experience from the self-calibration of panoramic cameras showed that some of the additional parameters cannot be determined without control points or object space constraints. In these cases the use of control points are recommended.

7

Conclusions

This dissertation developed a joint sensor model for panoramic cameras and laser scanners. It analyzed the precision and reliability structures of networks of panoramic cameras, and a joint network of frame array CCD and panoramic cameras. It investigated and analyzed self-calibration networks of panoramic cameras. It analyzed the datum-invariant parameters and quality analysis matrices of least squares adjustment. This chapter summarizes these topics and provides conclusions.

7.1 A Joint Sensor Model and Object Space Constraints

A joint sensor model was developed for terrestrial linear array-based panoramic cameras and laser scanners. The investigation on the sensor modeling was based on the stationary and non-stationary systematic errors of panoramic cameras. The stationary systematic errors, which mainly show themselves in the static mode of the panoramic camera, were investigated by the geometry of the linear array with respect to the turntable and lens distortions.

The non-stationary systematic errors, which are tumbling and non-equal angular pixel size were investigated by:

- the analysis of image point residuals for example through Fourier analysis,
- tumbling measurements of the turntable by measuring the inclination of the turntable during the panoramic camera operation.

Non-equal angular pixel size originates from the rotating device of the turntable. The sources of this type of systematic error are:

- non-linear angular velocity of the rotating device,
- inaccurate mechanical rotation axis, which causes the deviations of the trajectory of the projection center from a perfect circle,
- tumbling, which causes a non-uniform friction and leads to change of angular velocity.

This error was modeled by different sine wave functions.

Tumbling originates from the mechanical properties of the turntable. It is mainly caused by an incorrect and incomplete shape of ball bearings and the contacting surfaces. It was modeled with two different methods:

- implicit model by a patch-wise method
- explicit model by a distinct physical model

The first method is based on pure mathematical functions. It is simpler with respect to the second method but needs many control points. The second method is based on a distinct physical meaning and does not need many control points.

Additional parameters of panoramic cameras after modeling both stationary and non-stationary systematic errors are related to two different classes:

- A subset of Brown's additional parameters
- A new set of additional parameters for panoramic cameras alone

The first class of the additional parameters models lens distortions, the camera constant and the shift of principal point along the linear array. The second class models the deviation of the linear array with respect to the turntable, the correction to the angular pixel size, the non-equality of angular pixel size and tumbling.

Two different models of least squares adjustment were developed. The first is condition equations model with unknowns (mixed model), which is simple for elimination of λ. The second is observation equations model which is more practical for applications like texture mapping and network simulations.

Self-calibration through space resection and block triangulation was performed for two panoramic cameras, *SpheroCam* and *EYESCAN*. Sub-pixel accuracy levels were achieved for such highly dynamic systems. In addition, accuracy tests were performed to see the potential of the sensor in terms of accuracy in object space. Because of over-parameterization the divergence and oscillation of least squares bundle adjustment happens. Therefore the non-equal angular pixel size and tumbling parameters could not be determined through networks of minimal constraints datum. However, by using many control points these parameters could be determined successfully.

The minimum number of control points was investigated in the case of self-calibration networks. The results indicated that a minimal constraints datum can be used for self-calibration provided that the tumbling and non-equal angular pixel size parameters are known in advance.

Since the mathematical sensor model is highly non-linear, the unknown parameters are a lot, also the existence of many local minima at the goal function of the least squares, the divergence and oscillation of the bundle adjustment solution happens due to insufficient constraints. Therefore the possibility of using additional constraints was investigated. A new model of 3D straight-line constraints was developed for multi-projective center sensors. 3D straight-line constraints were investigated for the determination of the non-stationary systematic errors. The result of self-calibration using eight 3D straight-line constraints showed successful results for accuracy test and determining additional parameters with an inner constraints datum.

The sensor model of panoramic cameras was extended for the calibration of terrestrial laser scanners with the laser's intensity images. Some small changes were made to the sensor model of panoramic cameras. Therefore it only considers the angular aspects of terrestrial laser scanners. The results of self-calibration of a terrestrial laser scanner (*Imager 5003*) through space resection based on the extended sensor model indicated a sub-pixel accuracy level.

7.2 Network Design and Analysis

Close-range photogrammetric network designs of panoramic cameras and joint panoramic cameras and frame array CCD camera were studied by heuristic simulation. The aims of the study were two-fold. The first aim was to enhance the precision and reliability through network design in order to estimate object point coordinates with high precisions. The second aim was to investigate suitable panoramic camera networks for the purpose of self-calibration and point positioning.

7.2.1 Enhancing Precision and Reliability

For the purpose of precision and reliability enhancements, several networks of panoramic camera stations were studied. In all network cases an inner constraints datum (free network adjustment) was considered. The assumption of the simulation was that the sensor had been calibrated in advance.

With only two panoramic images, an indoor environment with the size of 15 m x 12 m x 3 m was measured. For a distance of 10 m from the camera stations, the standard deviations of the object point coordinates were better than 3 centimeters. The error ellipsoids of the object points from this network, as could be expected, were not isotropic and homogeneous. The measure of the internal reliability of this network is very high which means the network is not able to detect even very large blunders. The measure of the external reliability is also high which makes the network unreliable for accurate applications. However, this simple network with a limited accuracy can be used for applications such as archeology, crime and accident investigations where high precision is not demanded.

The precision and reliability were enhanced by adding two extra panoramic camera stations. In this case the standard deviations of the object point coordinates were better than 0.5 mm. The measure of the internal reliability was better than 0.45 pixel for both row and column axes. The measure of the external reliability for the object point coordinates was 1.61 mm. By adding 4 more panoramic camera stations a network of 8 stations was constructed. The precision and the measure of the external reliability of the object point coordinates of this network was enhanced respectively by a factor of 1.7 and 4.35 compared to the network of 4 panoramic camera stations. The error ellipsoids of the object points of this network were more isotropic and homogeneous with respect to the previous networks.

To improve the network geometry, 12 frame array CCD camera stations were added to the network of 8 panoramic camera stations. Four sub-networks of frame array CCD camera

stations were considered to enhance the precisions of the point coordinates at the 4 corners of the environment. The relative precision of this network was 1:97,200. The measures of the internal and external reliabilities of this network did not have a significance improvement compared to the network of 8 panoramic camera stations.

An equivalent network of only panoramic cameras with respect to the network of panoramic and frame array CCD cameras was also simulated. This network consisted of 16 panoramic camera stations. The estimated standard deviations from this network were similar to the network of frame array CCD and panoramic cameras. The measure of the external reliability of this network is better than the network of frame array CCD and panoramic cameras. However, a quicker image acquisition of the network of joint frame array CCD and panoramic cameras with respect to the network of only panoramic camera concludes the efficiency of the joint network for highly demanded precision. Such high precision is usually requested for industry and engineering applications.

7.2.2 Self-Calibration and Point Positioning

Networks of panoramic cameras were analyzed by heuristic simulation for the purpose of self-calibration and point positioning. Different networks consisting of leveled, unleveled, same height and different height of stations were studied. For the analysis of self-calibrating networks, the correlations of the parameters and accuracy tests were considered.

It was shown that by tilting the camera a positive effect on the determinability of additional parameters can be achieved. Tilt of around 10° gives stable results in all additional parameters and the determination of object space coordinates. A strong self-calibrating network, for both object point positioning and additional parameters determination, can be realized with tilted camera stations.

7.3 Datum-Invariant Parameters

Datum-invariant parameters and quality analysis matrices of least squares bundle block adjustment were shown and proved. It was shown with an analytical proof and numerically that the additional parameters of panoramic cameras and their cofactor matrices are datum-independent in the case of the minimal and the inner constraints datum. This implies that the change of the network datum does not influence additional parameters, their standard deviations and correlations among additional parameters.

The danger of over-constrained datum with imprecise control points was shown. As a general rule, the minimal or the inner constraints datums are suggested for self-calibration purposes provided that a strong geometrical network is established.

7.4 Future Research

The preliminary steps towards using panoramic cameras for close-range photogrammetric applications have been shown in this dissertation. The next step of the research is the use

of panoramic cameras for object reconstruction and texture mapping, e.g. in cultural heritage and indoor environment recording.

Because of different image geometry of panoramic cameras which causes a different sensor model and additional parameters compared to the frame array CCD cameras, the conventional close-range photogrammetric software cannot process panoramic images. Therefore, the sensor model and additional parameters that has been developed here and associated functions dealing with the sensor model and the image geometry (e.g. epipolar line) should be integrated into software.

The similarities in terms of errors and operations of panoramic cameras and terrestrial laser scanners (with intensity image) show that a joint sensor consisting of laser scanners and panoramic camera will be an efficient tool for close-range photogrammetric applications.

Appendix A

The Observation Model for the Ideal Panoramic Camera

A set of equations (A.1) shows the expansion of equation (3.3) for the ideal panoramic camera.

$$\begin{cases} X' = \lambda \cdot c \cdot \cos(\theta) \\ Y' = -\lambda \cdot c \cdot \sin(\theta) \\ Z' = \lambda \cdot y \end{cases} \tag{A.1}$$

with $\theta = j \cdot p_x$ and $y = (i - \frac{N}{2}) \cdot p_y$.

Equation (A.2) is obtained by eliminating λ from the first two equations of (A.1).

$$\theta = -\tan^{-1}(\frac{Y'}{X'}) \tag{A.2}$$

The new set of equations (A.3) can be obtained from equation (A.1).

$$\begin{cases} X'^2 + Y'^2 = \lambda^2 \cdot c^2 \\ Z'^2 = \lambda^2 \cdot y^2 \end{cases} \tag{A.3}$$

By eliminating λ from the equations of (A.3), equation (A.4) is obtained.

$$y = \frac{c \cdot Z'}{\sqrt{X'^2 + Y'^2}} \tag{A.4}$$

Equations (A.2) and (A.4) are the observation model for the ideal panoramic camera.

Appendix B

Minimum Distance of Two 3D Lines

Equation (B.1) shows two 3D lines *L1* and *L2* with two direction vectors (m_x, m_y, m_z) and (n_x, n_y, n_z).

$$\begin{aligned} L1 &: \frac{X - X_1}{m_x} = \frac{Y - Y_1}{m_y} = \frac{Z - Z_1}{m_z} = t_0 \\ L2 &: \frac{X - X_0}{n_x} = \frac{Y - Y_0}{n_y} = \frac{Z - Z_0}{n_z} = t_1 \end{aligned} \tag{B.1}$$

where, (X_1, Y_1, Z_1) and (X_0, Y_0, Z_0) are two arbitrary points on *L1* and *L2*.

The minimum distance of these two lines is computed by equation (B.2).

$$dis = \sqrt{lx^2 + ly^2 + lz^2} \tag{B.2}$$

where,

$$\begin{cases} lx = (X_1 - X_0) + (m_x \cdot t_1 - n_x \cdot t_0) \\ ly = (Y_1 - Y_0) + (m_y \cdot t_1 - n_y \cdot t_0) \\ lz = (Z_1 - Z_0) + (m_z \cdot t_1 - n_z \cdot t_0) \end{cases} \tag{B.3}$$

t_0 and t_1 are computed through equation (B.4).

$$\begin{cases} \begin{pmatrix} lx & ly & lz \end{pmatrix}^t \cdot \begin{pmatrix} m_x & m_y & m_z \end{pmatrix}^t = 0 \\ \begin{pmatrix} lx & ly & lz \end{pmatrix}^t \cdot \begin{pmatrix} n_x & n_y & n_z \end{pmatrix}^t = 0 \end{cases} \tag{B.4}$$

Appendix C

Matrix Inversion by Partitioning

The inversion of a square and non-singular matrix A can be computed by matrix partitioning. If matrix A is partitioned into four sub-matrices, equation (C.1), then its inverse is denoted by matrix B in equation (C.2).

$$A = \begin{pmatrix} A_{11} & A_{12} \\ A_{21} & A_{22} \end{pmatrix} \tag{C.1}$$

$$B = A^{-1} = \begin{pmatrix} A_{11} & A_{12} \\ A_{21} & A_{22} \end{pmatrix}^{-1}$$

$$\begin{pmatrix} A_{11} & A_{12} \\ A_{21} & A_{22} \end{pmatrix} . \begin{pmatrix} B_{11} & B_{12} \\ B_{21} & B_{22} \end{pmatrix} = \begin{pmatrix} I & 0 \\ 0 & I \end{pmatrix} \tag{C.2}$$

where,

$$\begin{cases} B_{21} = -A_{22}^{-1} \cdot A_{21} \cdot B_{11} \\ B_{11} = (A_{11} - A_{12} \cdot A_{22}^{-1} \cdot A_{21})^{-1} \\ B_{22} = A_{22}^{-1} - A_{22}^{-1} \cdot A_{21} \cdot B_{12} \\ B_{12} = -B_{11} \cdot A_{12} \cdot A_{22}^{-1} \end{cases} \tag{C.3}$$

or

$$\begin{cases} B_{22} = (A_{22} - A_{21} \cdot A_{11}^{-1} \cdot A_{12})^{-1} \\ B_{21} = -B_{22} \cdot A_{21} \cdot A_{11}^{-1} \\ B_{12} = -A_{11}^{-1} \cdot A_{12} \cdot B_{22} \\ B_{11} = A_{11}^{-1} - A_{11}^{-1} \cdot A_{12} \cdot B_{21} \end{cases} \tag{C.4}$$

Note that sub-matrices A_{11} or A_{22} should be non-singular.

Appendix D

Reliability

Reliability (Baarda, 1967) refers to the ability of a network to detect and resist blunders in observations. Usually we deal with "internal reliability" and "external reliability". The former refers to the ability of the network to detect blunders by tests of a hypothesis made with a specific confidence level (1-α) and power (1-β), while the latter is related to the effect of the undetectable blunders on the estimated parameters.

The measure of internal reliability that refers to the lower bound of just detectable blunder ($\nabla_0 l_i$) in the *i*th observation can be expressed as shown in equation (D.1):

$$\nabla_0 l_i = \frac{\delta_0 \sigma_{l_i}}{\sqrt{r_i}} \tag{D.1}$$

where δ_0 is the lower bound of the noncentrality parameter and is a function of α and β, and σ_{l_i} and r_i are the standard deviation and redundancy number of the *i*th observation, respectively.

The measure of external reliability, which refers to the maximum effect of the undetectable blunder ($\nabla_0 l_i$) on the estimates of unknown parameters, is given by equation (D.2):

$$\nabla_{0,i}\hat{X} = (A^t P A)^{-1}(A^t P \nabla_{0,i} l) \tag{D.2}$$

where, $\nabla_{0,i} l$ is a vector containing zeros except for $\nabla_0 l_i$ at the *i*th position.

From (D.1) and (D.2) we can see that the larger the redundancy number r_i, the smaller the size of the undetectable blunders as well as its influence on the estimated parameters.

Bibliography

The references are listed in alphabetic order. The following abbreviations are used:

ACSM: American Congress on Surveying and Mapping
AGU: American Geophysical Union
ASPRS: American Society for Photogrammetry and Remote Sensing
CVPR: Computer Vision and Pattern Recognition
DARPA: Defense Advanced Research Projects Agency
IAPRS: International Archives of Photogrammetry and Remote Sensing
ICCV: International Conference on Computer Vision
IEEE: Institute of Electrical and Electronics Engineers
ISP: International Society of Photogrammetry
PE&RS: Photogrammetric Engineering and Remote Sensing

1. Amiri Parian, J. and Gruen, A., 2003: A Sensor Model for Panoramic Cameras. 6th *Optical 3D Measurement Techniques* (Eds. Gruen, A. and Kahmen, H.), Vol. 2, pp. 130-141.

2. Amiri Parian, J. and Gruen, A., 2004a: A Refined Sensor Model for Panoramic Cameras. *IAPRS*, 34(5/W16), 12 pages, on CD-ROM http://www.commission5.isprs.org/wg1/workshop_pano/ [Visited: October 2006].

3. Amiri Parian, J. and Gruen, A., 2004b: An Advanced Sensor Model for Panoramic Cameras. *IAPRS*, 35(5), Istanbul, Turkey, pp. 24-29.

4. Amiri Parian, J. and Gruen, A., 2005a: Panoramic Camera Calibration Using 3D Straight Lines. *IAPRS*, 36(5/W8), 8 pages, on CD-ROM http://www2.informatik.hu-berlin.de/~knauer/ISPRS/panoramicworkshop2005/ [Visited: October 2006].

5. Amiri Parian, J. and Gruen, A., 2005b: Integrated Laser Scanner and Intensity Image Calibration and Accuracy Assessment. *IAPRS*, 36(3/W19), Enschede, the Netherlands, pp. 18-23.

6. Amiri Parian, J. and Gruen, A., 2005c: Close Range Photogrammetric Network Design for Panoramic Cameras by Heuristic Simulation. 7th *Optical 3D Measurement Techniques*, (Eds. Gruen, A. and Kahmen, H.), Vol. 1, pp. 273-244.

7. Amiri Parian, J. and Gruen, A.: 2006. Self-Calibrating Network Analysis for Panoramic Cameras by Heuristic Simulation. *IAPRS*, 36(5), Dresden, Germany, pp. 230-235.

8. Arvo, J., 1994: *Graphics Gems II*. Academic Press, New York, pp. 351-354 and pp. 377-380.

9. Baarda, W., 1967: A Testing Procedure for Use in Geodetic Networks. Netherlands Geodetic Commission, *Publications on Geodesy*, 2(4), Delft, the Netherlands.

10. Baker, S. and Nayar, S. K., 1998: A Theory of Catadioptric Image Formation. IEEE Proceedings of *ICCV*, pp. 35-42.

11. Benosman, R. (Ed.) and Kang, S.B., 2001: *Panoramic Vision: Sensors, Theory, and Application*. Springer publishing, 480 pages.

12. Bossler, J. D., Grafarend, E. W., and Kelm, R., 1973: Optimal design of geodetic nets. *Journal of Geophysical Research*, 78(26), pp. 5887–5897.

13. Boulianne, M., Nolette, C., Agnard, J. P., and Brindamour, M., 1997: Hemispherical Photographs Used for Mapping Confined Spaces. *PE&RS*, 63(9), pp. 1103-1109.

14. Boult, T. 1998: Remote reality via omnidirectional imaging. Proceedings of *DARPA Image Understanding Workshop.*

15. Brown, D.C., 1971: Close-Range Camera Calibration. *Photogrammetric Engineering*, 37(8), pp. 855-866.

16. Brown, D.C., 1976: The bundle adjustment – progress and prospects. *International Archive of Photogrammetry*, Helsinki, Finland, 21(B3), 33 pages.

17. Chen, S.E., 1995: QuickTime VR - An Image-Based Approach to Virtual Environment Navigation. *Computer Graphics* (SIG GRAPH '95), pp. 29-38.

18. Colcord, J.E., 1989: Using Fish-Eye Lens for GPS Site Reconnaissance. *Journal of Surveying Engineering*, 115(3), pp. 347-352.

19. Cross, P.A., 1985: Numerical Methods in Network Design. *Optimization and Design of Geodetic Networks* (Eds. Grafarend, E. and Sanso, F.), Springer, Berlin, pp. 429-435.

20. Fraser, C.S., 1984: Network Design Considerations for Non-Topographic Photogrammetry. *PE&RS*, 50(8), pp. 1115-1126.

21. Fraser, C.S., 1992: Photogrammetric Measurement to One Part in a Million. *PE&RS*, 58(3), pp. 305-310.

22. Fraser, C.S., 1996: Network Design, Chapter 9. *Close Range Photogrammetry and Machine Vision* (Ed. Atkinson, K. B.), Whittles Publishing, Scotland, pp. 256-281.

23. Fritsch, D. and Crosilla, F., 1990: First-Order Design Strategies for Industrial Photogrammetry. Close-Range Photogrammetry Meets Machine Vision (Eds. Gruen, A. and Baltsavias, E. P.), *SPIE Proceedings*, Vol. 1395, pp. 432-438.

24. Gotthardt, E., 1968: *Einfuehrung in die Ausgleichungsrechnung*. Herbert Wichmann Verlag Karlsruhe, 273 pages.

25. Grafarend, E.W., 1974: Optimization of Geodetic Networks. *Bollettino di Geodesia e Science Affini*, 33(4), pp. 351-406.

26. Gruen, A., 1978: Accuracy, Reliability and Statistics in Close-Range Photogrammetry. Proceedings of the Symposium of ISP, Commission V, Stockholm, Sweden.

27. Gruen, A., 1980: Precision and Reliability Aspects in Close-Range Photogrammetry. XIV Congress of ISP, Commission V, Hamburg, Federal Republic of Germany, pp. 117-133.

28. Gruen, A., and Beyer, H., 2001: System Calibration Through Self-Calibration. *Calibration and Orientation of Cameras in Computer Vision* (Eds. Gruen, A. and Huang, T. S.), Springer Verlag, Berlin Heidelberg, pp. 172-180.

29. Habib, A., Morgan, M., Kim, E.M. and Cheng, R., 2004: Linear Features in Photogrammetric Activities. *IAPRS*, 35(B2), Istanbul, Turkey, pp. 610-615.

30. Hamilton, W.R., 1844: On Quaternion; or on New System of Imaginaries in Algebra, *Philosophical Magazine* (25), pp. 10-13.

31. Hearn, D. and Baker, M.P., 1996: *Computer Graphics,* C Version, 2nd edition, Englewood Cliffs, NJ: Prentice-Hall, pp. 419-420 and pp. 617-618.

32. Heikkinen, J., 2005: *The Circular Imaging Block in Close-Range Photogrammetry*. Institute of Photogrammetry and Remote Sensing, Helsinki University of Technology, Doctoral Dissertation.

33. Hell, G., 1979: Terrestrische Bildtriangulation mit Beruecksichtigung zusaetzlicher Beobachtungen. DGK, Reihe C, Heft Nr. 252, Munchen, 90 pages.

34. Herbert, T.J., 1987: Area Projections of Fisheye Photographic Lenses. *Agricultural and Forest Metrology* (39), pp. 215-223.

35. Heuvel, F.A. van den, 1999: Estimation of Interior Orientation Parameters from Constraints on Line Measurements in a Single Image. *IAPRS*, 32(5/W11), pp. 81-88.

36. Heuvel, F.A. van den, Verwaal, R. and Beers, B., 2006: Calibration of Fisheye Camera Systems and the Reduction of Chromatic Aberration. *IAPRS*, 36(5), Dresden, Germany, 6 pages. On CD_ROM, http://www.isprs.org/commission5/proceedings06/pages/start.html [Visited: October 2006].

37. Hong, J., 1991: Image-based homing, *International Conference on Robotics and Automation*, May.

38. Kager, H. and Kraus, K., 1976: Geowissenschaftliche Mitteilungen. XIII. Internationale Kongress fuer Photogrammetrie, Helsinki.

39. Kukko, A., 2004: A New Method for Perspective Centre Alignment for Spherical Panoramic Imaging, *The Photogrammetric Journal of Finland*, 19(1), pp. 37-46.

40. Lawson, C.L. and Hanson, R.J., 1974: *Solving Least Squares Problems*. Prentice-Hall.

41. Lisowski, W. and Wiedemann, A., 1999: Auswertung von Bilddaten eines Rotationszeilenscanners**.** In: *Photogrammetrie und Fernerkundung Proceedings der 18. DGPF-Jahrestagung 1998 in München (*Editors: J. Albertz and S. Derch), Deutsche Gesellschaft für Photogrammetrie, Band 7, Berlin, 1999, pp.183-189.

42. Luhmann, T. and Tecklenburg, W., 2002: Bundle Orientation and 3-D Object Reconstruction from Multiple-Station Panoramic Imagery. *IAPRS*, 34(5), Corfu, Greece, pp. 181-186.

43. Luhmann, T. and Tecklenburg, W., 2004: 3-D Object Reconstruction from Multiple-Station Panorama Imagery. *IAPRS*, 34(5/W16), 8 pages, on CD-ROM http://www.commission5.isprs.org/wg1/workshop_pano/ [Visited: October 2006].

44. Marshall, A.R., 1989: *Network Design and Optimization in Close Range Photogrammetry*. Uniserv S36, the University of New South Wales, Sydney, Australia, 249 pp.

45. Marzan, G.T. and Karara, H.M., 1976: Rational Design for Close-Range Photogrammetry. Photogrammetry Series No 43, University of Illonois, Urbana, Illinois.

46. Mason, S., 1994: *Expert System-Based Design of Photogrammetric Networks*. Institute of Geodesy and Photogrammetry, ETH Zurich, Switzerland, No. 53, PhD Thesis.

47. Matthias, H., 1961: *Umfassende Behandlung der Theodolitachsenfehler auf vektorieller Grundlage unter spezieller Berücksichtigung der Taumelfehler der Kippachse*. Verlag Leemann, No. 10, Zürich, PhD Thesis.

48. Mikhail, E.M., Weerawong, K., 1994: Feature-Based Photogrammetric Object Reconstruction, ASPRS/ACSM Annual Convention Technical Papers, pp. 407-417.

49. Milgram, D.L. 1977: Adaptive techniques for photomosaicking. *IEEE Transactions on Computers*, C-26(11), pp. 1175–1180.

50. Nayar, S. K. and Baker, S., 1997: Catadioptric image formation, Proceedings of *DARPA Image Understanding Workshop*, pp. 1431-1437.

51. Olague, G., 2002: Automated Photogrammetric Network Design Using Genetic Algorithms. *PE&RS*, 68(5), pp. 423-431.

52. Ollis, M., Herman, H. and Singh, S., 1999: Analysis and Design of Panoramic Stereo Vision Using Equi-Angular Pixel Cameras. The Robotics Institute Carnegie Mellon University, CMU-RI-TR-99-04, Pittsburgh, PA 15213, 43 pages.

53. Peleg, S. and Herman, J. 1997: Panoramic mosaics by manifold projection. *CVPR'97*, pp. 338–343.

54. Petsa, E., Kouroupis, S. and Karras, G.E., 2001: Inserting the past in video sequences. *IAPRS*, 34(5C7), pp. 707-712.

55. Poentinen, P., 1999: On the Creation of Panoramic Images from Image Sequences, *Photogrammetric Journal of Finland*, 16(2), pp. 43-67.

56. Pope, A.J. 1971: Transformation of Covariance Matrices due to Changes in Minimal Control. Paper distributed at the AGU, Fall Annual Meeting in San Francisco.

57. Reddy, B.S. and Chatterji, N., 1996: An FFT-Based Technique for Translation, Rotation, and Scale-Invariant Image Registration. *IEEE Transactions on Image Processing*, 5(8). pp. 1266-1271.

58. Rich, P.M., 1990: Characterizing Plant Canopies with hemispherical Photographs. *Remote Sensing Reviews*, 5(1), pp. 13-29.

59. Saadatseresht, M., Fraser, C.S., Samadzadegan, F. and Azizi, A., 2004: Visibility Analysis in Vision Metrology Networks Design. *The Photogrammetric Record*, 19(107), pp. 219-236.

60. Schaffrin, B., 1985: Aspects of Network Design. *Optimization and Design of Geodetic Networks* (Eds. Grafarend, E. and Sanso, F.), Springer Verlag, Berlin, pp. 548-597.

61. Scheele, M, Börner, A., Reulke, R., Scheibe, K., 2001: Geometrische Korrekturen: Vom Flugzeugscanner zur Nahbereichskamera, *Photogrammetrie-Fernerkundung-Geoinformation*, Heft 1, pp. 13-22.

62. Scheibe, K., Korsitzky, H., Reulke, R., Scheele, M. and Solbrig, M., 2001: EYESCAN - A High Resolution Digital Panoramic Camera. *Robot Vision 2001,* Lecture Notes in Computer Science (1998), pp. 77-83.

63. Schmitt, G., 1985: A Review of Network Designs, Criteria, Risk Functions and Design Ordering. *Optimization and Design of Geodetic Networks* (Eds. Grafarend, E. and Sanso, F.), Springer Verlag, Berlin, pp. 6-10.

64. Schneider, D. and Maas, H.-G., 2003: Geometric modeling and calibration of a high resolution panoramic camera. *Optical 3D Measurement Techniques VI* (Eds. Gruen, A. and Kahmen, H.), Vol. 2, pp. 122-129.

65. Schneider, D. and Maas, H.-G., 2004: Application of a geometrical model for panoramic image data. *IAPRS*, 34(5/W16), 5 pages, on CD-ROM http://www.commission5.isprs.org/wg1/workshop_pano/ [Visited: October 2006].

66. Schneider, D. and Maas, H.-G., 2005: Combined Bundle Adjustment of Panoramic and Central Perspective Images. *IAPRS*, 36(5/W8), 4 pages, on CR-ROM http://www.informatik.hu-berlin.de/~knauer/ISPRS/panoramicworkshop2005/ [Visited: October 2006].

67. Schneider, D. and Maas, H.-G., 2006: A Geometric Model for Linear-Array-Based Terrestrial Panoramic Camera. *The Photogrammetric Record*, 21(115), pp. 198–210.

68. Schwalbe, E., 2005: Geometric modeling and calibration of fisheye lens camera systems. *IAPRS*, 36(5/W8), 6 pages. On CD-ROM http://www.informatik.hu-berlin.de/~knauer/ISPRS/panoramicworkshop2005/ [Visited: October 2006].

69. Shum, H. and Szeliski, R., 1997: Panoramic Image Mosaics. Microsoft Research, Technical Report, MSR-TR-97-23, 50 pages.

70. Slama, C.C. (Ed.), 1980: *Manual of Photogrammetry*. Fourth Edition, American Society for Photogrammetry and Remote Sensing, Falls Church, Virginia, pp. 196-207.

71. Svoboda, T., Pajdla, T. and Hlavac, V., 1997: Central Panoramic Cameras: Geometry and Design. Research report K335/97/147, Czech Technical University, Faculty of Electrical Engineering, Center for Machine Perception, 16 pages.

72. Szeliski, R. 1996: Video mosaics for virtual environments. *IEEE Computer Graphics and Applications*, 16(2), pp. 22–30.

73. Tienstra, J.M., 1956: *Theory of the Adjustment of Normally Distributed Observations*, Uitgeverij, Argus, Amsterdam.

74. Torlegard, K., 1980: On Accuracy Improvement in Close-Range Photogrammetry. *Proceedings of Industrial and Engineering Survey Conference*, London, England.

75. Vanicek, P. and Krakiwsky, E. J., 1986: *Geodesy: The Concepts* (second edition). Elsevier science publishers, the Netherlands, 714 pages.

76. Yagi,Y. and Yachida, 1991: Real-time generation of environmental map and obstacle avoidance using omnidirectional image sensor with conic mirror. In: *IEEE Conference on Computer Vision and Pattern Recognition*, pp. 160-165.

Acknowledgments

There are many people I would like to thank without whom this work would not have been realized or whose input significantly added to the scientific value.

I would like to start by thanking my supervisor, Prof. Dr. Armin Gruen who during the last four years provided me with scientific support and encouragement. His excellent guidance, accessibility, continuous supervision, quick feedback and his meticulous reviewing of the earlier versions of my work along with his invaluable comments are gratefully acknowledged.

I am also very grateful to co-supervisors: Associate Prof. Dr. Ali Azizi (Department of Surveying and Geomatics Engineering, Faculty of Engineering, University of Tehran) and Prof. Dr. habil. Hans-Gerd Maas (Institute of Photogrammetry and Remote Sensing, Technical University of Dresden) for their reviews and providing me with invaluable insights.

Next I would like to thank my colleagues for their support and contribution. A special thanks goes to Danilo Schneider and Prof. Dr. habil. Hans-Gerd Maas (Institute of Photogrammetry and Remote Sensing, Technical University of Dresden) who provided me the image and control point observations of the *EYESCAN* panoramic camera at the very beginning of my research; Prof. Dr. Ludger Hovestadt (Chair of Computer-Aided Architectural Design, ETH Zurich) who provided me the *SpheroCam* panoramic camera for image acquisition; Prof. Dr. Hilmar Ingensand and Dr. Thorsten Shultz (IGP, ETH Zurich) who supported me with the *Imager 5003* laser scanner; Beat Ruedin (IGP, ETH Zurich) for his hardware and software support; Soheil Sotoodeh (IGP, ETH Zurich) for providing easy-to-use software tools; Dr. AliReza Amiri-Simkooei (Delft Institute of Earth Observation and Space Systems, Delft University of Technology) for his invaluable feedback to my questions on the network optimization; Dr. Isabel Sargent and Dr. David Holland (Research, Ordnance Survey, UK) for proofreading and reviewing of my dissertation and providing excellent feedback and Henri Eisenbeiss (IGP, ETH Zurich) for translating the abstract to German.

I would like to mention colleagues who helped me indirectly to complete this dissertation: Liliane Steinbrueckner, Susanne Sebestyen, Dr. Fabio Remondino, Dr. Emmanuel Baltsavias, Dr. Daniela Poli, Dr. Jana Niederoest, Devrim Akca, Gerhard Schrotter, Dr. Li Zhang, Dr. Chunsun Zhang, Mehdi Rezaeian, Martin Sauerbier, Thomas Hanusch, Sultan Kocaman, Kirsten Wolff, Dr. Martijn de Ruijter de Wildt, Haris Papasaika, Natalia Vassilieva and Nusret Demir.

The Ministry of Science, Research and Technology (MSRT) of Iran and Swiss Federal Institute of Technology Zurich (ETH Zurich) are gratefully acknowledged for the financial support to pursue my research.

Last but by no means least, a special mention should go to my whole family for their support and motivation, particularly my parents AliReza and Hajar, whom I really missed in this period.

Curriculum Vitae

First name: **Jafar**
Family name: **Amiri Parian**
Date of birth: March 16, 1977
Place of birth: Shemiran, Tehran, Iran
Nationality: Iranian

EDUCATIONS

ETH Zurich, PhD. Photogrammetry — Zurich, Switzerland, 2003-2007
Institute of Geodesy and Photogrammetry
Thesis: Sensor Modeling, Calibration and Point Positioning with Terrestrial Panoramic Cameras

University of Tehran, M.Sc. Photogrammetry — Tehran, Iran, 1999-2001
Department of Surveying and Geomatics, Faculty of Engineering
Thesis: Implementation and Evaluation of an Automatic Face Reconstruction method Using the Digital Close-Range Photogrammetric Technique

University of Tehran, B.Sc. Surveying — Tehran, Iran, 1995-1999
Department of Surveying and Geomatics, Faculty of Engineering

RESEARCH INTEREST

- Sensor modeling, calibration and accuracy tests of optical sensors
- Geodetic and photogrammetric network design and analysis
- High level automation for vision metrology